# CONTROLS ON ANTIMONY AND ARSENIC SPECIATION VIA SORPTION AND REDOX CHEMISTRY AT THE CLAY MINERAL - WATER INTERFACE IN NATURAL AND LABORATORY SETTINGS

A

THESIS

Presented to the Faculty

of the University of Alaska Fairbanks

in Partial Fulfillment of the Requirements

for the Degree of

DOCTOR OF PHILOSOPHY

By

Anastasia Gennadyevna Ilgen, M.S.

Fairbanks, Alaska

December 2010

CONTROLS ON ANTIMONY AND ARSENIC SPECIATION VIA SORPTION AND REDOX CHEMISTRY AT THE CLAY MINERAL - WATER INTERFACE IN NATURAL AND LABORATORY SETTINGS

By

Anastasia Gennadyevna Ilgen

RECOMMENDED:

Advisory Committee Chair

Chair, Department of Chemistry & Biochemistry

APPROVED:

Dean, College of Natural Science & Mathematics

Dean of the Graduate School

Dec 6, 2010

Date

## Abstract

Adsorption and redox transformations of contaminants in soil and aqueous environments are often controlled by the available mineral substrates. Aluminosilicates and aluminum oxides are ubiquitous and can influence the speciation and, therefore, the transport and bio-availability of toxic elements such as arsenic (As) and antimony (Sb). It is important to understand the partitioning and redox reactions promoted by these substrates in order to understand and model the transport of As and Sb in soils and surface waters.

This study provides a detailed investigation of the sorption and redox behavior of As and Sb in clay-rich natural and laboratory systems. Since $Fe^{3+}$ is often found substituting for $Al^{3+}$ in clay mineral structures, we also investigated the role of structural Fe in redox transformations of As and Sb adsorbed at the clay surface in controlled laboratory experiments.

In a natural system affected by the release of spent geothermal fluids (Mutnovsky geothermal fields, Kamchatka, Russia), As concentrations are elevated above background levels in the Falshivaia River water and sediments (< 65 μm size fraction). Arsenic from the geothermal source fluids is in the reduced $As^{3+}$ form, and is oxidized to $As^{5+}$ after mixing with river water. Both $As^{3+}$ and $As^{5+}$ are found in aqueous and adsorbed forms. Analysis of the extended x-ray absorption fine structure (EXAFS) spectra shows that sediment-phase arsenic is associated with both Al- and Fe-rich phases with a bi-dentate corner-sharing local geometry.

A series of laboratory experiments were performed in order to investigate Sb adsorption by Al-rich mineral substrates at a macroscopic and molecular level. The EXAFS analysis of the experimental samples concluded that both $Sb^{3+}$ and $Sb^{5+}$ form inner-sphere sorption complexes on the surfaces of hydrous aluminum oxide (HAO), and the clay minerals kaolinite (KGa-1b) and nontronite (NAu-1). Primarily, bi-dentate corner-sharing with a minor amount of mono-dentate corner-sharing complexes were formed. The oxidation state of the clay structural Fe affects the adsorption capacity of nontronite; if the clay is partially reduced, the $Sb^{5+}$ uptake is increased significantly.

The long term dynamics of the As aqueous speciation in clay suspensions where reduced arsenic ($As^{3+}$) was added initially is complex. A fast disappearance of $As^{3+}$ due to oxidation to $As^{5+}$ was followed by a slow increase of aqueous $As^{3+}$. This behavior is explained by two simultaneous reactions: fast oxidation of $As^{3+}$ by structural $Fe^{3+}$ (anaerobic) or $Fe^{3+}$ and dissolved $O_2$ (aerobic) and the slow reduction of $As^{5+}$ by dissolved $Fe^{2+}$. The ability of the structural Fe in nontronite clay to promote oxidation of $As^{3+}/Sb^{3+}$ was greatly affected by its oxidation state: if all structural Fe was in an oxidized $Fe^{3+}$ form, no oxidation was observed; however, when ~ 20 % of structural Fe was reduced to $Fe^{2+}$, the clay promoted the most extensive oxidation under both aerobic and anaerobic conditions. The structural $Fe^{2+}$ is not able to reduce $As^{5+}/Sb^{5+}$, but reduction was seen when aqueous $Fe^{2+}$ was present in the systems.

These research findings indicate that As and Sb can be effectively immobilized by Al-rich phases, while the substrate nature and oxidation state of structural Fe, along with the presence of dissolved $Fe^{2+}$, can greatly affect the fate and transport of As and Sb. The increase in $Sb^{5+}$ uptake in response to reducing structural Fe, possible increase or decrease in uptake of As due to $As^{5+}$ reduction by aqueous $Fe^{2+}$, or oxidation of $As^{3+}$ by clay structural $Fe^{3+}$, is likely to take place in a natural clay-rich soil or aquifer environment in moderate to slightly reducing conditions.

## Table of Contents

Page

Page

Page

## List of Figures

Page

Page

Page

## List of Tables

Page

Page

## Dedication and Acknowledgments

This thesis is dedicated to my amazing, loving family, which made me who I am and helped me to get where I wanted to go.

Many people have contributed to the success of this work. First of all, I have to thank my adviser, Dr. Tom Trainor for opening up his group and allowing me to explore my own scientific interests. Tom ultimately shaped me as a scientist through his example of excellence and, sometimes invisible, but always firm guidance in improving the quality of my work. A very special thank should go to Dr. John Eichelberger, who opened the world for me by organizing my first visit to study abroad through his tireless efforts to build international research collaborations spanning the Ring of Fire. I was very lucky to participate in three international volcanological field schools led by John, where I learned about active volcanoes, about dreams and life, and how determined and strong scientists must be in their drive to climb every real and figurative mountain. Dr. Rainer Newberry was incredibly helpful and ingenious in both teaching geochemistry and helping me with a variety of analytical work. His perspective on both research and life, and his continuing help and support were truly invaluable. I would like to thank Dr. Cathy Cahill for her helpful advice and moral support when it was most needed. Dr. Bill Simpson joined the committee in the final years of my Ph.D. work; however his attention to detail and ability to ask just the right questions helped to shape my work and point me to excellence. Any failure to reach that goal of excellence is my own, for I lacked no support from the experts around me. Thank you all!

My past and current laboratory mates deserve special thanks: Dr. Christopher Iceman, Dr. Sarah Petitto, Ashley Jones, Kunal Tanwar, Peter Peterson, Vanessa Ritchie, Raena Rowland, and Kristen Williams. At different times you all helped me in one way or another, thank you. The whole Chemistry and Biochemistry Department and especially Emily Reiter and Mist D'June-Gussak need to be thanked for their administrative, technical, and personal support, as well. My samples never would have reached the synchrotron facilities in fact without Emily. My collaborator at the Institute of Volcanology and Seismology in Kamchatka, Dr. Sergey Rychagov helped with the

field study; Dr. Andrea Foster at the United States Geological Survey in California helped with the beam run work, and beam scientists Dr. Matt Newville, Dr. Dale Brewe and Dr. Joe Rodgers were also instrumental in my success with these instruments.

When the exhaustion of analytical, experimental, and school work outweighed the excitement of science, my husband, Brandon Ilgen, was always there for me with much needed encouragement and grammatical support. It would have been impossible to make it all the way through without his support. Our son, Ruslan Ilgen, was a sweet and cooperative baby who traveled (peacefully) with me for analytical work and conferences. I have to thank my parents, Dr. Nina A. Tranbenkova and Dr. Gennady G. Tranbenkov for cultivating my love for science and encouraging my desire to contribute in the scientific endeavor of producing new knowledge. My entire family deserves endless gratitude for their continuing help, support, and patience.

My funding sources included a graduate fellowship from the Inland Northwest Research Alliance (INRA), teaching assistantship at the Department of Chemistry and Biochemistry at the University of Alaska Fairbanks, National Science Foundation grants, and an International Association of GeoChemistry student research grant; travel to the conferences and analytical facilities was supported by travel grants from the Clay Minerals Society, a Goldschmidt meeting travel grant, and University of Alaska Fairbanks Graduate School and College of Natural Science and Mathematics travel grants.

# Chapter 1: Introduction and Objectives

*Science... it never solves a problem without creating ten more.*

**George Bernard Shaw**

## 1.1 Sources and Impacts of As and Sb Contamination

Chemical reactions at the surfaces of fine-grained minerals found in natural soil and aqueous environments are considered primary factors that determine the mobility and bioavailability of nutrients and contaminants, including the toxic metalloids antimony (Sb) and arsenic (As). The mobilization of As and Sb due to partitioning between surrounding rocks and ground water makes some aquifers dangerous for human use. This research advances the fundamental understanding of As and Sb reactions at the mineral surfaces affecting the transformations, retention, and transport of these metalloids in natural environments.

Typically enriched in both historical and modern volcanic and geothermal settings (Filella et al., 2002; Sabadell and Axtmann, 1975), antimony and arsenic are chalcophylic elements that can be mobilized and enter natural water as a result of rock weathering or industrial use. Arsenic is also a common contaminant associated with gold mining (Craw et al., 2000) and was widely used in pesticides and insecticides during the twentieth century (Frankenberger, 2002). In 1944, for example, the US alone used 36,000 tons of As in pesticide form (Frankenberger, 2002). Increased awareness of health risks associated with As has decreased use to less than 20,000 tons annually worldwide. Abundant in nature, the natural flux of As is of more concern than previous anthropogenic sources at the present time (Vaughan, 2006).

The naturally occurring amount of antimony is approximately 10 times less than arsenic. Due to its low abundance, the majority of natural waters have safe levels of dissolved Sb (Filella et al., 2002). Industrial use has artificially increased the

concentration of Sb in water and soil in mining and urban areas. In 2009 187,000 tons of Sb were utilized in industrial applications such as in flame retardants, pigments, and transportation (Carlin Jr, 2010).

Arsenic and antimony are both toxic and their toxicity depends on their chemical form: reduced $Sb^{3+}$ and $As^{3+}$ have higher acute toxicities than the oxidized forms $Sb^{5+}$ and $As^{5+}$ (Gebel, 1997). Safe limits in drinking water established by the United States Environmental Protection Agency (EPA) are 10 (Sb) and 6 (As) ppb.

Antimony is a suspected human carcinogen while vascular disease and cancer are associated with prolonged exposure to As through contaminated drinking water. A large scale As contamination problem exists in Asia, particularly in Bangladesh (Ahuja, 2008; Henke et al., 2009; Kinniburgh et al., 2003; O'Day, 2005; Ravenscroft et al., 2009), where 35 million people may be exposed to As-contaminated drinking water (Kinniburgh et al., 2003). Low-level As contamination occurs around the globe, including parts of the U.S. and Europe (Ryker, 2003; Vaughan, 2006). Antimony contamination in soils around mining and smelting sites, as well as urban and shooting range locations, creates concern for drinking water contamination on a local scale (Wilson et al., 2010).

### 1.2 Major Environmental Pathways for As and Sb

Areas of past and current geothermal activity are one possible source of As contamination. The dissolved As content in hot springs (forming as a result of rising hot water) and in the surface waters draining these systems commonly exceeds 10 ppb, and ranges from 0.1 to 10 ppm for different geothermal regions (Webster and Nordstrom, 2003). If a geothermal field is developed for electricity production, deep wells reaching the geothermal reservoir are drilled to bring the fluids to the surface to run steam turbines. If fluids are rising to the surface naturally (as in the case with hot-springs) their As content is decreased due to cooling and decompression, and precipitation of As minerals takes place before the fluid reaches the surface. In the case of fluids extracted for electricity production, these processes are bypassed, and the As concentration in the well fluids is about three orders of magnitude higher than in the surface waters (Webster

and Nordstrom, 2003). If the waste fluids are not re-injected underground, the As flux at the surface increases. For example, the Wairakei geothermal power station in New Zealand is the largest single source of As in Waikato River (Webster and Nordstrom, 2003), where As is mostly transported in dissolved form with 7-8% adsorbed to suspended particulate matter. The resulting As content in the Waikato River sediment is 61-1,790 mg/kg (Webster and Nordstrom, 2003). There is a close association between arsenic and iron oxides in river and lake sediments affected by waste geothermal water (Webster and Nordstrom, 2003). However, the molecular understanding and exact binding mechanism for the interactions between mineral substrates and As originating from high temperature reducing fluids exposed at the surface remains unknown.

The solution concentration, and the mobility and bioavailability of Sb and As, are limited by (co)precipitation and partitioning reactions. The major factors affecting As and Sb partitioning between aqueous and solid phases are the oxidation state of As and Sb, the nature of the surface moieties on the adsorbing substrate, the presence of competing ions or complexing ligands, pH, and, to a lesser extent, ionic strength. The reversibility of adsorption depends on the bonding between the adsorbed species and the mineral surface. The chemisorption, or inner-sphere mode of adsorption, refers to bonding between the adsorbed species and $OH_2^+$, OH and $O^-$ surface functional groups; the physisorption, or outer-sphere mode of adsorption, exists due to electrostatic attraction or hydrogen bonding (Stollenwerk, 2003). The bonds are weaker in the latter case; therefore, the physisorbed species are more mobile. Understanding the adsorbed species on a molecular level is a key component of the surface complexation modeling for predicting the concentration of As and Sb in the aqueous and solid phases.

In laboratory batch experiments, As immobilized at the surfaces of synthetic Fe- (Fendorf et al., 1997; Manceau et al., 2007; Manning et al., 1998; Ona-Nguema et al., 2005; Sherman and Randall, 2003; Waychunas et al., 1995; Waychunas et al., 2005), Al- (Arai et al., 2001; Arai and Sparks, 2002; Arai et al., 2005; Foster, 1999; Ladeira et al., 2001) and Mn-oxides (Foster et al., 2003; Manning et al., 2002) and natural clay minerals (Foster, 1999; Ladeira and Ciminelli, 1998) usually form inner-sphere mono- and bi-

dentate corner-sharing complexes as shown by means of X-ray Absorption Spectroscopy (XAS); the outer-sphere As complexes were also reported on the surfaces of corundum $Al_2O_3$ and hematite $Fe_2O_3$ (012) identified by Resonant Surface X-ray Scattering (Catalano et al., 2008). In natural samples collected from mine tailings and contaminated soils, the inner-sphere sorption complexes were reported (Beaulieu and Savage, 2005; Cances et al., 2005; Gault et al., 2005; Gault et al., 2003; Manning, 2005; Morin et al., 2002; Strawn et al., 2002; Voegelin et al., 2007). The laboratory studies of Sb partitioning conclude that, similar to As, Sb is effectively adsorbed by Mn- (Kovalenko, 1958; Rauf et al., 1994; Thanabalasingam and Pickering, 1990), Al- (Thanabalasingam and Pickering, 1990; Xu et al., 2001) and Fe- oxides (Leuz et al., 2006b; Watkins et al., 2006). In natural settings, Sb is adsorbed by Fe-oxide mineral surfaces and forms inner-sphere bi-dentate corner and edge-sharing complexes (Scheinost et al., 2006). A more detailed review of Sb adsorption behavior is presented in Chapter 4. In short, the information about Sb partitioning to Al-oxides and clay minerals is limited, while XAS studies of the molecular environment and adsorption complexes of Sb on these substrates do not exist.

Some of the Mn- and Fe-oxides and clay mineral substrates, in addition to their role in adsorption, are capable of promoting reduction or oxidation of contaminants through catalysis or, possibly, direct electron transfer (Hofstetter et al., 2003; Hofstetter et al., 2006; Oscarson et al., 1981). For example, the oxidation of $As^{3+}$ in both aerobic and anaerobic conditions is enhanced in the presence of the Fe-oxide goethite (Lin and Puls, 2000; Stollenwerk, 2003) and the clay minerals kaolinite and illite (Lin and Puls, 2000; Lin and Puls, 2003; Manning and Goldberg, 1997). Several experimental results conclude that $As^{3+}$ is oxidized by dissolved $O_2$ while Fe in goethite (Ona-Nguema et al., 2005) or Ti impurities in kaolinite (KGa-1) (Foster et al., 1998) act as catalysts; and others simply report observed $As^{3+}$ oxidation in anaerobic conditions in the presence of Fe-oxides and clay mineral substrates (Lin and Puls, 2000; Lin and Puls, 2003). There are few observations regarding Sb redox reactions promoted by mineral substrates. There is evidence that $Sb^{3+}$ is oxidized by the amorphous Fe- and Mn-oxides (Belzile et al.,

2001), and in aerobic conditions $Sb^{3+}$ can be oxidized by dissolved $O_2$ and $H_2O_2$ in the presence of goethite FeOOH via the Fenton mechanism (Leuz et al., 2006a; Leuz and Johnson, 2005). A more detailed overview of As and Sb redox transformations promoted by mineral substrates is presented in Chapter 3. In summary, the exact mechanism and reactive species involved in the oxidation reactions promoted by the mineral substrates are not fully understood.

### 1.3 Research Objectives and Methodology

This research addresses As and Sb sorption and redox reactions associated with mineral surfaces including: i) control and nature of reactive species involved in redox reactions promoted by mineral substrates; ii) laboratory studies and speciation of Sb and As in natural samples; iii) characterization of Sb adsorption on aluminosilicate mineral substrates to better constrain the stoichiometry of adsorption reactions.

The specific objectives were: I) to provide a detailed analysis of As speciation in the near surface aquatic and sediment environment affected by the release of spent geothermal fluids in order to correlate As chemical form with transport characteristics in a natural system; 2) to characterize adsorption of Sb by Al-rich substrates at the macroscopic and molecular levels; and 3) to determine whether Fe incorporated in the clay mineral structure can promote redox transformations of As and Sb under oxic and anoxic conditions.

The naturally occurring clay substrates were chosen for the experimental part of this study due to their abundance in a typical soil or aqueous environment and the indications in literature that they can be important As and Sb scavengers (Charlet et al., 2005; Wilson et al., 2010). The interactions of Sb and As with aluminosilicate clays are also significantly less studied compared to interactions with metal (Fe, Al and Mn) oxides. It is commonly seen that smectite clays have Fe incorporated in the structure substituting for Al in the octahedral layer (Stucki, 2006). The structural $Fe^{2+}$ in clays was shown to reduce nitroaromatic compounds (Hofstetter et al., 2006) and chromium (Taylor et al., 2000). Since Fe-oxides are able to facilitate oxidation of $As^{3+}$ and $Sb^{3+}$, one of the

goals for this project was to determine whether $Fe^{2+}/Fe^{3+}$ incorporated in clay mineral structures can participate in redox transformations of As and Sb.

### 1.4 Summary of Presented Work

Chapters 2 through 4 of this work are written as individual manuscripts for submission in peer reviewed journals. Chapter 2 describes speciation and fate of As from a high temperature geothermal fluid released into a surface environment. The location for this study was the Dachny geothermal fields in the Mutnovsky region, Kamchatka (Russia), where a 50 MWt geothermal power plant operates. The waste fluids have elevated As content, and a portion of the waste is discharged in the surface water. Various types of water and sediment samples were analyzed using analytical wet chemistry methods in order to correlate the redox and adsorption behavior of As with the geochemical characteristics of the system. The oxidation state of As was determined using Liquid Chromatography coupled to Inductively Coupled Plasma Mass Spectrometry (LC-ICP MS). The oxidation state and molecular environment of As immobilized by the river sediment was assessed using XAS techniques. The results indicate that different water types can be distinguished based on their major ion composition. The deep well fluids are characterized by high $Cl^-$ ion concentrations, which are used as their geochemical signature and indicate mixing of waste fluids with pristine water. Based on the major ion composition of the Falshivaia River, the river water is a mixture between different source waters. After reduced well fluid is mixed with oxygenated river water, the reduced forms of sulfur are oxidized first, followed by arsenic and ammonia, then iron. Both reduced $As^{3+}$ and oxidized $As^{5+}$ are immobilized by the bottom sediments, through the formation of inner-sphere adsorption complexes. Both Al and Fe 2$^{nd}$ shell neighbors were identified in the XAS data, indicating that Al- and Fe-rich mineral substrates are important arsenic scavengers. The crystalline phases found in the fine (<63 μm) sediment fraction were volcanic plagioclase, stilbite and quartz, and clay minerals from the smectite group. The field area has extensive zones of hydrothermal alteration characterized by the presence of clay minerals kaolinite,

montmorillonite, illite-smectite, and Fe-oxide minerals, which contribute to the river sediments. Since reduced and oxidized forms of arsenic were found in aqueous and adsorbed forms, the question of whether the oxidation is primarily a homo- or heterogeneous reaction became apparent.

Chapter 3 details a batch study implemented to test the reactivity of the clay minerals kaolinite and nontronite in promoting heterogeneous redox transformations of arsenic and antimony. More specifically, the study was designed to answer the following questions:

1) Is $Sb^{3+}$ oxidation catalyzed by the Ti-impurities in kaolinite (KGa-1b), similarly to $As^{3+}$ oxidation?

2) Can structural $Fe^{3+}$ in nontronite (NAu-1) be an $e^-$ acceptor in the oxidation of $As^{3+}$ and $Sb^{3+}$ immobilized at the clay surface?

3) How does the ability of the structural $Fe^{2+}$ in nontronite to reduce $As^{5+}$ and $Sb^{5+}$ compare to the reactivity of the dissolved $Fe^{2+}$ added to the clay suspensions?

The observations of As speciation changes in the nontronite clay suspensions, where reduced $As^{3+}$ was added initially, were interpreted as a result of two simultaneous reactions:

$$H_3AsO_3\ (aq) + Fe_2O_3\ (structural) \rightarrow H_3AsO_4\ (aq) + 2FeO\ (structural) \quad (1)$$

$$H_3AsO_4\ (aq) + 2Fe(OH)_2\ (aq) \rightarrow Fe_2O_3\ (sorbed) + H_3AsO_3\ (aq) + 2H_2O \quad (2)$$

The validity of reaction (2) was also confirmed by an independent experiment with $As^{5+}$ added to the clay suspensions with aqueous $Fe^{2+}$. The kinetics of reaction (1) is on the order of hours, while the kinetics for reaction (2) is on the order days. However, the presence of the oxidized As species – the product of the reaction (1) - decreases over time. This behavior indicates that the reactive sites associated with the nontronite clay are passivated over time, likely once they are occupied by adsorbed As species. There

was no reduction of $As^{5+}$ and $Sb^{5+}$ by the clay structural $Fe^{2+}$, while aqueous $Fe^{2+}$ present in clay suspensions was reactive.

The findings indicate that structural $Fe^{3+}$ does oxidize $As^{3+}$ and $Sb^{3+}$ quite effectively; however, in order for this reaction to take place, some $Fe^{2+}$ should be present in the clay structure together with $Fe^{3+}$. The oxidation capacity of the fully oxidized NAu-1 (only structural $Fe^{3+}$ present) is insignificant compared to the partially reduced NAu-1 (structural $Fe^{2+}$ and $Fe^{3+}$ are present). The Ti in kaolinite (KGa-1b) is much less effective in promoting $Sb^{3+}$ oxidation, compared to $As^{3+}$.

The main focus of Chapter 4 is to describe $Sb^{3+}$ and $Sb^{5+}$ partitioning on the Al-rich substrates. Macroscopic uptake studies were coupled with Extended X-ray Absorption Fine Structure (EXAFS) Spectroscopy to identify the mode of adsorption and the local molecular environment around Sb atoms. The kinetics of adsorption was relatively slow (~days), and inner-sphere adsorption complexes were identified on all the studied substrates. The oxidation state of Fe in nontronite clay influences the extent of the $Sb^{5+}$ uptake: the highest uptake was seen in the systems with partially reduced nontronite NAu-1.

In Chapter 5, the current research findings and their relevance to the natural environment are summarized, and ideas for the future work building from the results discussed in chapters 2 through 4 are presented.

## References

Ahuja, S. (Ed.), 2008. Arsenic contamination of groundwater: mechanism, analysis & remediation. John Wiley & Sons, Inc., 387 pp.

Arai, Y., Elzinga, E., Sparks, D., 2001. X-ray absorption spectroscopic investigation of arsenite and arsenate adsorption at the aluminum oxide–water interface. Journal of colloid and interface science, 235(1): 80-88.

Arai, Y., Sparks, D., 2002. Residence time effects on arsenate surface speciation at the aluminum oxide-water interface. Soil Science, 167(5): 303.

Arai, Y., Sparks, D., Davis, J., 2005. Arsenate adsorption mechanisms at the allophane-water interface. Environmental Science & Technology, 39(8): 2537-2544.

Beaulieu, B., Savage, K., 2005. Arsenate adsorption structures on aluminum oxide and phyllosilicate mineral surfaces in smelter-impacted soils. Environmental Science & Technology, 39(10): 3571-3579.

Belzile, N., Chen, Y., Wang, Z., 2001. Oxidation of antimony (III) by amorphous iron and manganese oxyhydroxides. Chemical Geology, 174(4): 379-387.

Cances, B. et al., 2005. XAS Evidence of As (V) Association with Iron Oxyhydroxides in a Contaminated Soil at a Former Arsenical Pesticide Processing Plant. Environmental Science & Technology, 39: 24.

Carlin Jr, J., 2010. Antimony, U.S. Geological Survey, Mineral Commodity Summaries. USGS.

Catalano, J., Park, C., Fenter, P., Zhang, Z., 2008. Simultaneous inner-and outer-sphere arsenate adsorption on corundum and hematite. Geochimica et cosmochimica acta, 72(8): 1986-2004.

Charlet, L. et al., 2005. Adsorption and heterogeneous reduction of arsenic at the phyllosilicate-water interface. In: O'Day, P., Vlassopoulos, D., Meng, X., Benning, L. (Eds.), Advances in Arsenic Research: Integration of Experimental and Observational Studies and Implications for Mitigation.

Craw, D., Chappell, D., Reay, A., Walls, D., 2000. Mobilisation and attenuation of arsenic around gold mines, east Otago, New Zealand. New Zealand Journal of Geology and Geophysics, 43(3): 373-384.

Fendorf, S., Eick, M., Grossl, P., Sparks, D., 1997. Arsenate and chromate retention mechanisms on goethite. 1. Surface structure. Environmental Science & Technology, 31(2): 315-320.

Filella, M., Belzile, N., Chen, Y., 2002. Antimony in the environment: a review focused on natural waters I. Occurrence. Earth Science Reviews, 57(1-2): 125-176.

Foster, A., 1999. Partitioning and transformation of arsenic and selenium in natural and laboratory systems, Ph. D. thesis, Stanford Univ., Stanford, California.

Foster, A., Brown, G., Parks, G., 1998. X-ray absorption fine-structure spectroscopy study of photocatalyzed, heterogeneous As (III) oxidation on kaolin and anatase. Environmental Science & Technology, 32: 1444-1452.

Foster, A., Brown, G., Parks, G., 2003. X-ray absorption fine structure study of As (V) and Se (IV) sorption complexes on hydrous Mn oxides. Geochimica et cosmochimica acta, 67(11): 1937-1953.

Frankenberger, W., 2002. Environmental chemistry of arsenic. CRC.

Gault, A., Cooke, D., Townsend, A., Charnock, J., Polya, D., 2005. Mechanisms of arsenic attenuation in acid mine drainage from Mount Bischoff, western Tasmania. Science of the Total Environment, 345(1-3): 219-228.

Gault, A. et al., 2003. Arsenic speciation in surface waters and sediments in a contaminated waterway: an IC–ICP-MS and XAS based study. Applied Geochemistry, 18(9): 1387-1397.

Gebel, T., 1997. Arsenic and antimony: comparative approach on mechanistic toxicology. Chemico-biological interactions, 107(3): 131-144.

Henke, K., Atwood, D., Blue, L., 2009. Arsenic: Environmental Chemistry, Health Threats and Waste Treatment. Wiley.

Hofstetter, T., Schwarzenbach, R., Haderlein, S., 2003. Reactivity of Fe (II) species associated with clay minerals. Environmental Science & Technology, 37(3): 519.

Hofstetter, T.B., Neumann, A., Schwarzenbach, R.P., 2006. Reduction of Nitroaromatic Compounds by Fe(II) Species Associated with Iron-Rich Smectites. Environmental Science & Technology, 40(1): 235-242.

Kinniburgh, D. et al., 2003. The scale and causes of the groundwater arsenic problem in Bangladesh. Arsenic in Ground Water: 211-257.

Kovalenko, P., 1958. Adsorption of trivalent antimony my manganese dioxide. Nauchnye doklady vysshei shkoly. Khimiia i khimicheskaia tekhnologiia: 710-713.

Ladeira, A., Ciminelli, V., Duarte, H., Alves, M., Ramos, A., 2001. Mechanism of anion retention from EXAFS and density functional calculations: Arsenic (V) adsorbed on gibbsite. Geochimica et cosmochimica acta, 65(8): 1211-1217.

Ladeira, A.C.Q., Ciminelli, V.S.T., 1998. Arsenic immobilization by adsorption on clay minerals, International Conference on Fundamentals of Adsorption (6th). Elsevier, Giens, France, pp. 515-520.

Leuz, A., Hug, S., Wehrli, B., Johnson, C., 2006a. Iron-mediated oxidation of antimony (III) by oxygen and hydrogen peroxide compared to arsenic (III) oxidation. Environmental Science & Technology, 40(8): 2565-2571.

Leuz, A., Johnson, C., 2005. Oxidation of Sb (III) to Sb (V) by $O_2$ and $H_2O_2$ in aqueous solutions. Geochimica et cosmochimica acta, 69(5): 1165-1172.

Leuz, A., Mönch, H., Johnson, C., 2006b. Sorption of Sb (III) and Sb (V) to Goethite: Influence on Sb (III) Oxidation and Mobilization. Environ. Sci. Technol, 40(23): 7277-7282.

Lin, Z., Puls, R., 2000. Adsorption, desorption and oxidation of arsenic affected by clay minerals and aging process. Environmental geology, 39(7): 753-759.

Lin, Z., Puls, R., 2003. Potential indicators for the assessment of arsenic natural attenuation in the subsurface. Advances in Environmental Research, 7(4): 825-834.

Manceau, A., Lanson, M., Geoffroy, N., 2007. Natural speciation of Ni, Zn, Ba, and As in ferromanganese coatings on quartz using X-ray fluorescence, absorption, and diffraction. Geochimica et cosmochimica acta, 71(1): 95-128.

Manning, B., 2005. Arsenic speciation in As(III)- and As(V)-treated soil using XANES spectroscopy. Microchimica Acta, 151(3-4): 181-188.

Manning, B., Fendorf, S., Bostick, B., Suarezs, D., 2002. Arsenic (III) oxidation and arsenic (V) adsorption reactions on synthetic birnessite. Environmental Science & Technology, 36(5): 976-981.

Manning, B., Goldberg, S., 1997. Adsorption and Stability of Arsenic (III) at the Clay Mineral- Water Interface. Environmental Science & Technology, 31(7): 2005-2011.

Manning, B.A., Fendorf, S., Goldberg, S., 1998. Surface structures and stability of arsenic(III) on geothite: Spectroscopic evidence for inner-sphere complexes. Environmental Science & Technology, 32(16): 2383-2388.

Morin, G. et al., 2002. EXAFS evidence of sorbed arsenic (V) and pharmacosiderite in a soil overlying the Echassières geochemical anomaly, Allier, France. Bulletin de la Societe Geologique de France, 173(3): 281.

O'Day, P. (Ed.), 2005. Advances in Arsenic Research: Integration of Experimental and Observational Studies and Implications for Mitigation. American Chemical Society, Washington, DC.

Ona-Nguema, G., Morin, G., Juillot, F., Calas, G., Brown Jr, G., 2005. EXAFS analysis of arsenite adsorption onto two-line ferrihydrite, hematite, goethite, and lepidocrocite. Environmental Science & Technology, 39(23): 9147-9155.

Oscarson, D., Huang, P., Liaw, W., 1981. Role of manganese in the oxidation of arsenite by freshwater lake sediments. Clays and Clay Minerals, 29(3): 219-225.

Rauf, M., Ikram, M., Hasany, S., 1994. Adsorption studies of antimony on manganese dioxide using radiometric techniques. Adsorption science & technology, 11(1): 41-50.

Ravenscroft, P., Brammer, H., Richards, K., 2009. Arsenic Pollution: A global synthesis. Wiley-Blackwell.

Ryker, S., 2003. Arsenic in Ground Water Used for Drinking Water in the United States. In: Welch, A., Stollenwerk, K. (Eds.), Arsenic in ground water: geochemistry and occurrence. Kluwer Academic Pub.

Sabadell, J., Axtmann, R., 1975. Heavy metal contamination from geothermal sources. Environmental Health Perspectives, 12: 1.

Scheinost, A. et al., 2006. Quantitative antimony speciation in shooting-range soils by EXAFS spectroscopy. Geochimica et cosmochimica acta, 70(13): 3299-3312.

Sherman, D., Randall, S., 2003. Surface complexation of arsenic (V) to iron (III)(hydr) oxides: structural mechanism from ab initio molecular geometries and EXAFS spectroscopy. Geochimica et cosmochimica acta, 67(22): 4223-4230.

Stollenwerk, K., 2003. Geochemical processes controlling transport of arsenic in groundwater: A review of adsorption. Arsenic in ground water: Geochemistry and occurrence: 67-100.

Strawn, D., Doner, H., Zavarin, M., McHugo, S., 2002. Microscale investigation into the geochemistry of arsenic, selenium, and iron in soil developed in pyritic shale materials. Geoderma, 108(3-4): 237-257.

Stucki, J., 2006. Properties and behaviour of iron in clay minerals. Handbook of Clay Science: 423–475.

Taylor, R., Shen, S., Bleam, W., Tu, S., 2000. Chromate removal by dithionite-reduced clays: evidence from direct X-ray adsorption near edge spectroscopy (XANES) of chromate reduction at clay surfaces. Clays and Clay Minerals, 48(6): 648.

Thanabalasingam, P., Pickering, W., 1990. Specific sorption of antimony (III) by the hydrous oxides of Mn, Fe, and Al. Water, Air, & Soil Pollution, 49(1): 175-185.

Vaughan, D.J., 2006. Arsenic. Elements, 2(2): 71-75.

Voegelin, A., Weber, F., Kretzschmar, R., 2007. Distribution and speciation of arsenic around roots in a contaminated riparian floodplain soil: Micro-XRF element mapping and EXAFS spectroscopy. Geochimica et cosmochimica acta, 71(23): 5804-5820.

Watkins, R. et al., 2006. Investigations into the kinetics and thermodynamics of Sb (III) adsorption on goethite ([alpha]-FeOOH). Journal of colloid and interface science, 303(2): 639-646.

Waychunas, G., Davis, J., Fuller, C., 1995. Geometry of sorbed arsenate on ferrihydrite and crystalline FeOOH: Re-evaluation of EXAFS results and topological factors in predicting sorbate geometry, and evidence for monodentate complexes. Geochimica et cosmochimica acta, 59(17): 3655-3661.

Waychunas, G. et al., 2005. Surface complexation studied via combined grazing-incidence EXAFS and surface diffraction: arsenate on hematite (0001) and (10–12). Analytical and bioanalytical chemistry, 383(1): 12-27.

Webster, J., Nordstrom, D., 2003. Geothermal arsenic. Arsenic in Ground Water: Geochemistry and Occurrence (AH Welch and KG Stollenwerk, editors). Kluwer Academic Publishers, Boston, USA: 101-125.

Wilson, S., Lockwood, P., Ashley, P., Tighe, M., 2010. The chemistry and behaviour of antimony in the soil environment with comparisons to arsenic: A critical review. Environmental Pollution(158): 1169-1181.

Xu, Y., Ohki, A., Maeda, S., 2001. Adsorption and removal of antimony from aqueous solution by an activated alumina. Toxicological & Environmental Chemistry, 80(3): 133-144.

# Chapter 2: Arsenic Speciation and Transport During the Utilization of Hydrothermal Resources for Electricity Production in Mutnovsky Field (Kamchatka, Russia)[1]


## Abstract

The use of geothermal fluids for the production of electricity poses the risk of contaminating surface waters when spent fluids are discharged into (near) surface environments. Arsenic (As) in particular is a common component in geothermal fluids and poses a potential risk to water quality when present in mobile and bioavailable forms. We have examined arsenic speciation and the extent of transport associated with the release of spent geothermal fluids at the Dachny geothermal fields (Mutnovsky geothermal region), Kamchatka, Russia- a high temperature field used for electricity production. In the spent fluids, the arsenic concentration reaches 9 ppm, while in natural hot water springs expressed in the vicinity of the field the As concentration is typically below 10 ppb. The aqueous phase arsenic speciation was determined using Liquid Chromatography (LC) coupled to an Inductively Coupled Plasma Mass Spectrometer (ICP-MS). The arsenic speciation in the bottom sediments (< 65 μm fraction) of the local surface waters was analyzed using X-ray Absorption Spectroscopy (XAS). Arsenic in the geothermal source fluids is predominantly found as $As^{3+}$, while a mixture of $As^{3+}/As^{5+}$ is found in the water and sediment of the Falshivaia River downstream from the power plant. The extent of elevated arsenic concentrations in water is limited by adsorption to the bottom sediment and dilution, as determined using $Cl^-$ from the deep well fluids as a tracer. Analysis of the Extended X-ray Absorption Fine Structure (EXAFS) spectra shows that sediment phase arsenic is associated with both Al- and Fe-rich phases with a bi-dentate corner sharing local geometry. The geothermal waste fluids released in the surface water create a localized area of arsenic contamination. The extent


[1] Ilgen A.G., Rychagov S.N., Trainor T.P. 2010. Arsenic speciation and transport during the utilization of hydrothermal resources for electricity production in Mutnovsky Field (Kamchatka, Russia). Prepared for submission in Chemical Geology

of transport of dissolved As is limited to ~ 7 km downstream from the source, while As associated with bottom sediment travels ~ 3 km farther.

## 2.1 Introduction

The toxicity and widespread occurrence of arsenic (As) in ground and surface water across the globe has stimulated research aimed at understanding its environmental behavior in a variety of natural settings. These studies have been recently summarized in several comprehensive reviews (Ahuja, 2008; Henke et al., 2009; O'Day, 2005; Ravenscroft et al., 2009; Vaughan, 2006; Welch and Stollenwerk, 2003). Ingestion of inorganic arsenic creates both acute and chronic deleterious effects on the cardiovascular, respiratory, gastrointestinal, hematological, hepatic, and neurological systems; the chronic exposure also affects dermal and reproductive functions (ATSDR, 2007). The long-term consumption of even small amounts of As through drinking contaminated water increases the risk of skin, bladder, lung, kidney, liver, and other types of cancer (Vaughan, 2006). Due to the high toxicity of As compounds, it is included in the USEPA priority pollutants list. The mobility of As in surface aqueous and soil environments is generally limited by (co)precipitation and adsorption reactions: Fe, Al, and Mn oxides, along with clay minerals, are capable of serving as effective sinks for As. The reduced form of arsenic $As^{3+}$, which is more toxic than the oxidized form, $As^{5+}$ (ATSDR, 2007) is also thought to be more mobile due to apparently lower affinity towards adsorption to mineral surfaces (Ravenscroft et al., 2009). Therefore, controls on the arsenic oxidation state play an important role in both environmental impact and transport properties of arsenic.

Among other common sources of arsenic to surface environments (e.g. rock weathering, acid mine drainage, industrial waste and pesticide use), it is also often observed in elevated concentrations in areas of volcanic and geothermal activity (Aiuppa et al., 2006; Ballantyne and Moore, 1988; Henke et al., 2009; Sakamoto et al., 1990; Webster and Nordstrom, 2003). The development of geothermal areas for energy production can significantly increase the output of heavily mineralized fluids, high in As,

into surface water systems (Arnórsson, 2004; Pascua et al., 2005; Webster-Brown and Lane, 2005b). For example, the largest single source of As (~40%) in the Waikato River, New Zealand, is the Wairakei geothermal power station. In this system the majority of As was found to be present in dissolved form, with only ~7% retained by bottom sediments (Webster-Brown and Lane, 2005b). It was also found that the seasonal increase of the dissolved arsenic concentration in the Waikato River is controlled by a decrease in the adsorption to suspended particulate material (SPM), and specifically by the variation of Fe content in SPM (Webster-Brown and Lane, 2005a). In an extensive analysis of the geothermal power plant pipe scales from the Akita prefecture geothermal field (northwestern Japan) by X-ray Diffraction (XRD), Attenuated Total Reflection Infrared (ATR IR), X-ray Fluorescence (XRF), X-ray Absorption Spectroscopy (XAS) and selective chemical extractions it was found that As is predominantly associated with Mg-rich smectite clays; adsorption was excluded as a retention mechanism, and As incorporation within the smectite structure or occurrence within mineral occlusions suggested (Pascua et al., 2005).

Spectroscopic studies of $As^{3+}/As^{5+}$ adsorption to synthetic Fe- (Fendorf et al., 1997; Manceau et al., 2007; Manning et al., 1998; Ona-Nguema et al., 2005; Sherman and Randall, 2003; Waychunas et al., 1995; Waychunas et al., 2005), Al- (Arai et al., 2001; Arai and Sparks, 2002; Arai et al., 2005; Foster, 1999; Ladeira et al., 2001), and Mn-oxides (Foster et al., 2003; Manning et al., 2002) and clay minerals (Foster, 1999) conclude that As generally binds as an inner sphere adsorption complex with a binuclear bidentate ($^2C$) geometry. Outer-sphere As complexes were also reported on the surfaces of corundum $Al_2O_3$ and hematite $Fe_2O_3$ (012) identified by resonant surface X-ray scattering (Catalano et al., 2008). Arsenic in mine tailings and contaminated soils in oxidizing conditions is most commonly found as $As^{5+}$ chemisorbed to Fe/Al-rich phases (Beaulieu and Savage, 2005; Cances et al., 2005; Foster et al., 1998; Gault et al., 2005; Gault et al., 2003; Manning, 2005; Morin et al., 2002; Strawn et al., 2002; Voegelin et al., 2007) or incorporated in minerals like scorodite or jarosite (Foster et al., 1998; Gault et al., 2005), ferric arsenates (Paktunc et al., 2003), or pharmacosiderite (Morin et al.,

2002). The reduction of $As^{5+}$ to $As^{3+}$ is seen in the bottom sediment (formed by precipitation of added $FeCl_2$) with increase in reducing conditions at depth below 10 cm (Kneebone et al., 2002; Root et al., 2007). Under sulfur reducing conditions $As^{-1}/As^0$ may be incorporated in sulfide minerals like arsenian pyrite (Foster, 2003).

While there have been numerous studies of arsenic speciation in ground water and soils affected by As mobilization from surrounded rocks, sulfide ore deposits, or pesticide use, there has been less work on the environments affected by the release of As from a geothermal source. The geochemical conditions in the geothermal fluids differ significantly from the low-temperature water (mainly due to the larger range of mineralization and pH) and therefore have the ability to alter the expected environmental behavior of As. There is ever growing interest in using alternative energy sources for electricity production leading to an increase in the use of geothermal energy (Arnórsson, 2004) with the associated potential for surface water contamination from spent fluids. One conventional way of dealing with it is re-injection of used thermal fluid back underground (Arnórsson, 2004); however, this is an expensive process and not always successful (Arnórsson, 2004; Chernev, 2005), therefore, there is a need to understand the degree of As transport and accumulation in cases of its release into surface water.

Here we detail a case study of the environmental behavior of As from a high temperature geothermal source originating from 400-2,000 m depth (Kiryukhin et al., 2005) and released into a surface water system. The goal of the present study is to characterize As transport and accumulation in the surface water/sediment environment and determine how the behavior correlates with the geochemical conditions of this system. In particular we are interested in understanding how the redox and sorption behavior of As varies with the rapid changes in fluid chemistry and redox potential after exposure of the fluids to the surface environment.

## 2.2 Study Area

The area of study is a high temperature geothermal field (Dachny field within larger Mutnovsky geothermal region) located near the Mutnovsky volcano on the

Kamchatka peninsula, Russia. The exploration of the geothermal field started in 1978 and has lasted for more than 30 years, and still continues. Since 1978, 92 wells have been drilled for the purpose of exploration and research (Kiryukhin et al., 2005). Thirteen production wells were used for generating electricity in 2005 (Chernev, 2005) with a discharge of about 170 kg/s of hydrothermal fluid (Kiryukhin et al., 2005). The concentrations of As in these fluids reached 9.3 ppm (current study). Re-injection of the used geothermal fluid has caused changes in the reservoir pressure (Chernev, 2005); the current operation allows some waste fluid to be cooled in settling ponds and then released into the local surface waters. In 2005 there was 11,096,000 tons of fluid extracted, from which 7,102,000 tons were re-injected (Chernev, 2005).

The geology of the Mutnovsky geothermal region area is dominated by tuffs and breccias of contrasting composition - from rhyolitic to basaltic. The tuff conglomerates, pumice tuffs, and ignimbrites are widely spread; the typical average rock composition is andesitic and andesitic-dacitic (Leonov, 1989). These volcanic rocks are characterized by high alkali metal content, especially potassium. The geothermal reservoir resides in the fractured rock fault zone. The fractured host rock is composed of diorites, Miocene-Pliocene sandstones, rhyolites and andesite tuffs and lavas. The geothermal reservoir is divided in two zones: liquid- (over 1,000 m deep) and steam-dominated (depth under 900 m) (Taran et al., 1986). The secondary hydrothermal alteration in the deeper zone results in a quartz-epidote-chlorite assemblage, while the shallower zone (steam – dominated, and characterized by a high degree of mixing with meteoric water) has calcite-chlorite-illite mineralization (Kiryukhin et al., 2004). The hot-springs discharging at the surface have $Na^{+}/SO_4^{2-}$ composition and acidic pH (Chudaev, 2003).

Due to the surface hydrothermal activity in the study area (Figure 2.1), the volcanic rocks are undergoing fast alteration. There are two geochemically distinct rock alteration zones: the upper zone extending from the surface to 0.5-0.7 m deep, and the lower zone which is 1.5-2 m deep (Slovtsov, 1994). In the upper zone, the characteristic minerals are kaolinite, elemental sulfur, limonite and some others, while montmorillonite, and illite-smectite are predominant in the lower zone along with pyrite, limonite, small

amounts of hematite, magnetite and Ti-magnetite (Slovtsov, 1994). Due to the large amount of atmospheric precipitation and elevation differences, the erosion processes are very fast, which leads to a large input of mineral alteration products from both zones to the Falshivaia River (Figure 2.1). The heavier mineral fractions tend to accumulate at the higher elevations closer to the source, including magnetite, quarts, pyroxene, ilmenite, hornblende, hematite, and some carbonate (Ilgen and Rychagov, 2007). The bottom sediments in the thermal lakes are composed of pyrite, limonite, ilmenite, quartz, calcite and dolomite, hematite, pyroxene, barite, and elemental sulfur; these mineral grains are commonly coated with limonite in association with kaolinite, montmorillonite and illite-smectite (Ilgen and Rychagov, 2007).

## 2.3 Experimental Procedures

### *2.3.1 Water sampling and chemical analysis*

The field sampling was conducted in August of 2006. The locations of field samples are shown on the map in Figures 2.1 and 2.2. A total of 50 water samples and 30 bottom sediment samples were collected (Figure 2.2), along with 11 clay samples from the areas of hydrothermal alteration around hot-springs and mud-pools (Figure 2.2 insert). Water samples were collected from the Kotiol stream and the Falshivaia River, as well as water from several natural hot-springs in the area, waste water settling ponds, waste streams, wellhead water (liquid phase), and condensed steam from the productive wells. To sample the wellhead fluid (wet steam), we used a stainless steel Webre separator, following the procedure outlined by Arnórsson and D'Amore (Arnórsson and D'Amore, 2000) to separately sample the steam and liquid phase of the well discharge. All water samples were filtered through a 0.45 μm high capacity disposable filter with a Versapor filter membrane (Geotech 73050004). These filtered samples are used to operationally define the dissolved content of the samples. We preserved the samples with ultrapure 6M $HNO_3$ to pH ~ 2 for major cation and trace metal analysis and with ultrapure 6M HCl for Fe, As and Sb speciation analysis. Samples for the determination of sulfide were collected in 125 ml bottles and preserved with 1 ml 1M zinc acetate and

titrated with 6N NaOH to pH $\geq$ 9. Bottom sediment samples were collected by wet sieving to obtain the <63 μm size fraction. Samples were collected / stored in HDPE bottles (HDPE amber bottles were used for As, Sb and Fe speciation samples) and kept at 4 °C until analysis. The oxidation-reduction potential (ORP), pH, conductivity and temperature were measured *in situ* using double junction ORPTestr10, ECTestr high+ and pH Testr30 (Oakton instruments).

Water samples were analyzed using ion chromatography (Dionex ICS-2000) for major cation (IonPac CS12A column) and anion (IonPac AS19 column) composition. The operational parameters suggested in the IC column manuals were optimized using standard solutions before sample analysis. The mobile phase for cation analysis was methanesulfonic acid (MSA, supplied by Dionex). To optimize the cation peak resolution, the concentration of MSA was varied from 10 mM at the beginning of the analytical run (0-3 minutes), to 3 mM (2.5-25 minutes), followed by linear increase to 15 mM (26.5-50 minutes). For the anion analysis, NaOH (Dionex) mobile phase was used. The optimum peak resolution was observed with the following sequence: 0.5 mM NaOH (0-3 minutes), linearly increased to 12 mM (3-12 minutes), and then linearly increased to 50 mM at 12-35 minutes. The conductivity cell temperature was set at 30 °C.

Milli-Q water with the resistivity of 18.2 MΩ·cm, 0.2 μm filtered and UV-irradiated (< 1 ppb total organic carbon) was used for preparing all solutions (Barnstead NANOpure® DIamond™).

Trace elements were measured using an inductively coupled plasma mass spectrometry (Agilent 7500ce ICP MS) (Creed et al., 1994). To remove $^{40}Ar^{35}Cl$ polyatomic interference during analysis of arsenic, the ICP MS was operated in a collision/reaction cell (CRC) mode using He gas.

Alkalinity was determined by titrating 100 ml of a filtered sample with 0.0200 N $H_2SO_4$ (Fisher) to a pH of 4.5 (Eaton and Franson, 2005). The resulting alkalinity (mg $CaCO_3 \cdot L^{-1}$) was calculated as 10 times volume of 0.0200 N $H_2SO_4$. For alkalinities < 20 $mg \cdot L^{-1}$ the titration was stopped in the range of pH from 4.3 to 4.6, and then continued

using micro-burette so that pH is exactly 0.3 units lower. The resulting alkalinity was calculated using the expression (Eaton and Franson, 2005):

$$Alk_{total}, mgCaCO_3 / L = \frac{(2B - C) \times N \times 50{,}000}{mLsample}$$

Where B is volume (ml) of $H_2SO_4$ used to the first recorded pH; C is total volume (ml) of $H_2SO_4$ to reach pH 0.3 unit lower; and N is normality of $H_2SO_4$ acid.

The level of dissolved sulfide was determined by potentiometric titration (Eaton and Franson, 2005) using a combination silver/sulfide electrode (Orion 94-16). The electrode performance was checked every 2 hours and calibration standards were measured every 4 hours. The ZnS precipitate formed during sample preservation was separated and dissolved in 50 ml of the alkaline antioxidant reagent and diluted to 100 ml volume with deoxygenated milli-Q water prior to the potential measurement; the alkaline antioxidant reagent was prepared by combining 80 g NaOH, 35 g ascorbic acid $C_6H_8O_6$, 67 g $Na_2H_2EDTA$ in deaerated milli-Q water and bringing the total volume to 1 L (Eaton and Franson, 2005).

The oxidation state of arsenic and antimony in water was determined using a liquid chromatography (LC) (Agilent 1100) coupled to an ICP MS (Agilent 7500ce). The separation was done using an arsenic speciation column (Agilent G3154-65001, 4.6 mm×150 mm i.d) and guard column (Agilent G3154-65002, 4.6 mm×10 mm i.d.) packed with chemical bonded hydrophilic anion exchange resin. The mobile phase for As speciation was prepared following the Agilent recommended recipe (As speciation analysis handbook, Agilent technical notes) and consisted of 2 mM $NaH_2PO_4$, 0.2 mM NaEDTA, adjusted to pH 6 with 1 M NaOH; it also contained 50 ppb of Ge as internal standard. The mobile phase for Sb oxidation state analysis consisted of 12 mM NaEDTA, 2mM phtalic acid and 3 vol.% methanol at pH ~ 4.5 (modified from (Zheng et al., 2001)). For arsenic speciation analysis the sensitivity optimization was done at a set radio-frequency (RF) power of 1400 W, and injection volume 50 µl, while for antimony the RF power was set at 1500 W, and sample injection volume was 100 µl. The flow rate of the mobile phase through the column was 1 ml·minute$^{-1}$. The detector count time for

$^{75}As$ was 0.5 seconds per point, total acquisition time was 800 seconds; count time for $^{121}Sb$ and $^{123}Sb$ was 0.5 seconds per point, total acquisition time was 450 seconds. The $As^{3+}$ and $As^{5+}$ peaks were centered at 112 and 435 seconds; the $Sb^{3+}$ and $Sb^{5+}$ peaks were centered at 210 and 130 seconds respectively.

The aqueous $Fe^{2+}$ and $Fe_{total}$ were determined by UV visible spectrophotometry (UV VIS) using the ferrozine method (To et al., 1999). Calibration standards with 0.004-1.6 ppm of $Fe^{2+}$ were prepared daily by diluting aliquots of an $Fe^{2+}$ stock solution (25 mM reagent grade $FeSO_4 \cdot 7H_2O$ in deoxygenated milli-Q water containing 1 v/v % ultrapure HCl) in deoxygenated milli-Q water. To prevent oxidation of $Fe^{2+}$ in standard solutions and to reduce $Fe^{3+}$ to $Fe^{2+}$ in samples intended for the $Fe_{total}$ measurement, we added a 1 ml aliquot of reagent grade 10 % w/v hydroxylamine hydrochloride solution to each 40 ml of standard solution or sample in a 50 ml volumetric flask. Then a 1 ml aliquot of 4.9 mM ferrozine reagent was added to all samples, and total volume of each sample was brought to 50 ml with milli-Q water. The concentration of $Fe^{2+}$ was determined by measuring the absorbance at 562 nm; $Fe^{3+}$ was calculated as difference between $Fe_{total}$ and $Fe^{2+}$.

The Visual MINTEQ interface, version 2.61 (Gustafsson, 2007) to the MINTEQ program (Felmy et al., 1983) and standard minteq thermodynamic database was used to calculate the saturation indexes in well water samples with respect to Al and Fe phases. In the input we used the concentrations of the major ions, total Al and Fe with fixed pH (measured in the field when water cooled to 50 °C) and temperature (99.99 °C). Since well fluids are in highly reducing conditions the total measured Fe was assumed to be $Fe^{2+}$. In order to calculate the saturation indexes in the fluid after it has been exposed at the oxidizing surface conditions we assumed measured $Fe_{total}$ to be $Fe^{3+}$. The Geochemist Workbench (GWB) software (Bethke, 1998) and Lawrence Livermore National Laboratory LLNL V8 R6 thermodynamic dataset (Delany and Lundeen, 1990) was used to calculate the distribution between ionic and hydrolyzed $Fe^{3+}$ species.

*2.3.2 Bottom sediment sampling and chemical analysis*

The bottom sediments were analyzed for major/minor composition using a PanAnalytical Axios 4 kilowatt wavelength dispersive X-ray Fluorescence Spectrometer (XRF). To minimize the sample matrix and self-absorption effects the samples were melted into glass beads using a Claisse M4 fluxer fueled with propane. One gram of air dried bottom sediment was mixed with 10 grams of 50/50 $Li_2B_4O_7/LiBO_2$ mixture (Claisse, pure grade) in a platinum crucible; the resulting dilution factor was 11. The total heating time was 20 minutes. The same recipe was used to prepare the calibration standards using geologic reference materials BIR-1, PCC-1, JA-2, JB-2, JP-1, JR-1, GXR-3, GXR-1, MPG-1, SGR-1; to optimize the calibration for sulfur $MgSO_4$ was added quantitatively to several standards. The loss on ignition was <7 % for the standards, and between 7-15 % for the samples.

For phase identity, randomly orientated dried sample powders were analyzed by X-ray powder diffraction using PANalytical Material Research Diffractometer (MRD) using Cu kα radiation. Scans were carried out with a 0.01 degree step size from 2 to 82 degrees 2θ, and counting time of 1 second per point. The resulting peak positions were matched manually using tabulated values (Chen, 1977).

The bottom sediment samples in the form of unaltered wet pastes were analyzed for As oxidation state and local bonding environment using synchrotron based x-ray absorption spectroscopy (XAS) at the bending magnet beamline 13 BMC at Advanced Photon Source, Argonne National Laboratory, IL. As K-edge (11,867 eV) spectra were collected under ambient temperature using a Canberra 16 element Ge detector (in fluorescence mode). The reference spectrum of a Au (L-edge 11,919 eV) foil placed in line after the sample was recorded with each scan in transmission mode using an ionization chamber. The beamline is equipped with a Si(111) water-cooled monochromator; a vertical focusing mirror was used to reject higher harmonics. The monochromator was also detuned by ~50 % to minimize contribution from the higher harmonics.

The monochromator step size was 5 eV in the pre-edge, 0.5 eV in the XANES region and 0.05 $Å^{-1}$ in the EXAFS region with a counting time of 2 seconds per point. For low concentration samples, counting time was longer at higher k (a power of 2 or 3 was applied). Each sample was scanned multiple times to improve signal-to-noise ratio. The comparison of a minimum 10 EXAFS scans showed that the oxidation state of As was not changing as a result of beam-induced redox chemistry during data acquisition in samples containing $As^{3+}$. Standards for As oxidation states were sodium meta-arsenite ($NaAsO_2$ 99.3% JT Baker) and sodium arsenate ($Na_2HAsO_4 \cdot 7H_2O$ 101.9% JT Baker). In addition we prepared a co-precipitation sample by adding 150 μL of 15 mM $Na_2HAsO_4$ solution to 10 ml of Milli-Q $H_2O$, then adding 21 ml of 0.5 M $Al(NO_3)_3$. After the solution was mixed precipitation took place during the slow titration with 6M NaOH to pH ~7.5. This co-precipitate was made to mimic possible co-precipitation process in the cooling well fluid.

The EXAFS/XANES data processing included background removal (AUTOBK algorithm (Newville et al., 1993)), normalization, aligning and averaging the scans as described elsewhere (Kelly et al., 2008). The Athena and Artemis interfaces (Ravel and Newville, 2005) to the IFEFFIT program (Newville, 2001) were used for data processing and fitting. The Fourier transformed As K-edge EXAFS spectra were analyzed by fitting theoretical calculated phase and amplitude functions for specified paths. The phase and amplitude functions were calculated using the FEFF6 code (Zabinsky et al., 1995). Theoretical As-O and As-Fe single scattering (SS) and multiple scattering (MS) paths were calculated based on the structure of scorodite $FeAsO_4 \cdot 2H_2O$ (Xu et al., 2007) and for As-O, As-Al and MS paths using the structure of esperanzaite $NaCa_2Al_2(AsO_4)2F_4(OH) \cdot 2H_2O$ (Foord et al., 1999). The shell-by-shell fitting approach was used; the final fitting was done in R-space using a Kaiser-Bessel window and k-weight of 3. Initially, the 1st shell (As-O) was fit using an R-range from 1.0 to 2.0 Å to determine an initial value for $\Delta E_0$ (energy shift between experimental and theoretical spectra). The k range used for fitting was chosen to be from 2.7 to approximately 9, 10, or 11 based on the data quality. Before performing the final fit, the isolated 2nd shell (As-

Al or As-Fe SS paths) was fit, and multiple scattering paths were accounted for as described in previous publications (Voegelin et al., 2007). Shortly, the included MS paths are 1) triangular As-O-As (MS1), with degeneracy of 12, R = 1.8165×$R_{As-O}$, and Debye-Waller parameter $\sigma^2 = \sigma^2_{As-O}$; 2) collinear As-O-As-O (MS2) with degeneracy of 4, R = 2×$R_{As-O}$, $\sigma^2 = 4\times\sigma^2_{As-O}$; and non-collinear As-O-As-O (MS3) with degeneracy of 12, R = 2×$R_{As-O}$, $\sigma^2 = 2\times\sigma^2_{As-O}$. The final fits were performed over the R-range from 1.0 to 4.2 Å, using a constrained value of $\Delta E_0$. The quality of the fit was determined based on the R-factor (the mean square misfit between the model and data) and had to be <0.05 for the fit to be acceptable (Kelly et al., 2008), the resulting R-factors for the field samples are 0.01-0.04.

## 2.4 Results and Discussion

The water sampling locations are shown in Figures 2.1 and 2.2. The water samples labeled as waste include all samples from the drainages that were visually identified as being impacted by the discharge from the power plant and samples from the settling ponds. The two phases of fluid from the productive wells are identified as well water and well steam; the other streams category includes streams that are contributing to the Falshivaia River and are not affected by the discharge from the power plant; the hot springs category includes several thermal springs along the Kotiol stream, Medvejia thermal field and Utinoie lake (Figure 2.1). The Falshivaia River samples include water samples both upstream and downstream from the power plant.

### *2.4.1 Major/Minor element aqueous chemistry*

The chemical composition of water samples from the Dachny area (Mutnovsky geothermal field) are shown in Table 2.1. From the ternary diagrams (Figure 2.3) we observe that the water samples can be distinguished based on their major cation and anion composition. The groupings indicate that well fluids (and resulting waste) have predominantly a $Na^+/K^+/Cl^-$ composition, whereas well steam is $Na^+/K^+$ and $SO_4^{2-}$ dominated. The natural hot-springs are discharging meteoric water heated by geothermal

steam and have a range of cation ($Ca^{2+}/K^{+}/Na^{+}$) composition, but are predominantly $SO_4^{2-}$ and $HCO_3^{-}$ in anionic composition, consistent with previous publication (Chudaev, 2003). The results of the well water sampling are also consistent with previous reports based on the well-water sampling in 1980-1984 (Taran et al., 1986): the deep well water has a $Na^{+}/Cl^{-}$ composition, while well steam has a mixed $Na^{+}/K^{+}/Ca^{2+}/SO_4^{2-}/HCO_3^{-}$ composition and low (<1 ppm) $Cl^{-}$ content. Compositionally, the water samples from the Falshivaia River plot in the middle of the observed range (Figure 2.3). The chloride content of the water differs depending on the origin of the sample (Figure 2.3 and Table 2.1). The well waters have the highest $Cl^{-}$ content (average at 232 ppm), while well steam, hot-spring water and other streams in the area have a $Cl^{-}$ concentration <1.7 ppm. The $Cl^{-}$ content in the Falshivaia River is elevated above the background level of 1.7 ppm (sample MF 27) due to the waste fluid input.

The redox potential ($E_H$) of the water samples was determined in the field using the ORP electrode, and also calculated from the analytical data based on three redox couples: $Fe^{2+}/Fe^{3+}$, $H_2S/SO_4^{2-}$ and $NO_3^{-}/NH_4^{+}$. These calculations are summarized in Table 2.2. For the $Fe^{2+}/Fe^{3+}$ redox couple, we used the standard redox potential for the reaction $Fe^{3+} + e^{-} \leftrightarrow Fe^{2+}$ from (Tagirov et al., 2000). The activities of the free ions ($Fe^{2+}$ and $Fe^{3+}$) were computed using the GWB software with the analytical totals for $Fe^{2+}$ and $Fe^{3+}$ as input. In these calculations the $Fe^{2+}$ and $Fe^{3+}$ redox was decoupled in order to compute the distribution of aqueous species for each oxidation state independently. The calculated standard redox potentials $E_H^{o}$ were corrected for different temperatures (measured in the field) for the $Fe^{2+}/Fe^{3+}$ couple (Tagirov et al., 2000) and for $H_2S/SO_4^{2-}$ and $NO_3^{-}/NH_4^{+}$ couples (Stefánsson et al., 2005). In computing the redox potential from the sulfur species $H_2S$ was assumed to be the dominant sulfide form below pH 7.04 ($pKa_1$) and $HS^{-}$ was assumed to dominate at pH>7.04. In the nitrogen calculations it was assumed that the $NH_4^{+}$ concentration determined by the IC analysis is the same as the concentration of the unhydrolyzed $NH_4^{+}$ species in the water samples.

The calculated redox potentials versus pH are shown in Figure 2.4. These findings show that there is a systematic offset between the couples (and ORP); there is a

positive correlation between the *in situ* ORP measurement and calculated redox potentials for all three couples (Figure 2.5). These observations are in agreement with previous studies of both cold and thermal water systems (Stefánsson et al., 2005), and suggest that there is a thermodynamic disequilibrium among the set of selected redox couples.

In Figure 2.6 the $E_H$ computed based on the $Fe^{2+}/Fe^{3+}$ redox couple is re-plotted vs. pH. Also depicted is the $E_H$/pH diagram ($Fe_{total}$ = 1 nM, at 25°C and $10^5$ Pa) from (Takeno, 2005) constructed based on the LLNL thermodynamic database (Delany and Lundeen, 1990). We also included an equilibrium line between $Fe^{2+}$ and amorphous $Fe(OH)_3$ computed using 1 μM concentration of $Fe_{total}$ (average for the field samples) and temperature of 15 °C. Stefánsson et al. (Stefánsson et al., 2005) observed that many non-thermal ground and surface waters sampled from Iceland appear to show a redox equilibrium between $Fe^{2+}$ and amorphous $Fe(OH)_3$. Similarly our surface water and hot spring samples show a trend that is in general agreement with the idea that iron redox chemistry includes the equilibrium between aqueous $Fe^{2+}$ and precipitated $Fe^{3+}$ phases. The geothermal well fluids and waste fluids are reducing and appear to be well undersaturated with respect to the precipitation of the $Fe^{3+}$ phases.

*2.4.2 Trace element chemistry*

Arsenic is often found in elevated concentrations in hydrothermal systems. Examining the trace element data for the Dachny area we observe that elevated (>10 ppb and up to 10 ppm) As concentrations were exclusively found in well water and waste fluids, and not in any of the hot springs (< 4 ppb As) in the area. Arsenic content was also low (<1 ppb) in the cold streams (the background samples). In addition to arsenic we observed that antimony was elevated in a number of samples. The antimony concentration was elevated in the settling pool (130 ppb), several well water samples and waste samples (~ 40 ppb).

We assume that chloride ion acts as a conservative tracer (Arnórsson and D'Amore, 2000) and, as discussed above, is a good indicator of mixing between pristine waters and waste fluids. In Figures 2.7 and 2.8 we show the correlation between As vs.

$Cl^-$ and Sb vs. $Cl^-$ for different water types. It is evident that high $Cl^-$ content in water samples corresponds to high contents of As and Sb. To further access whether decrease in As and Sb concentrations downstream the Falshivaia River is due to simple dilution with uncontaminated surface waters or if there is an additional immobilization mechanism (e.g. adsorption) we calculated predicted concentrations of As and Sb downstream from the source based on the dilution observed for $Cl^-$ ion. The dilution factors with respect to $Cl^-$ ion are defined as $DF_{Cl^-} = [Cl^-]/[Cl^-]_{source}$. The predicted concentrations for As and Sb were defined as $[Concentration]_{predicted} = [Concentration]_{source} \times DF_{Cl^-}$. The observed concentrations for both As and Sb fall below the predicted, which indicates that As and Sb do not behave conservatively (Figure 2.9). It was also found that bottom sediment samples have an elevated As concentration (determined by XRF analysis) in the area affected by mixing with high As water, therefore adsorption of As and transport with river sediment is an important pathway (Figure 2.10). The Sb content in HCl digested sediment samples was relatively low, likely due to low extractability of Sb using incomplete digestion method. The overall Sb content in different water types is summarized in Table 2.3.

Arsenic originating from reduced geothermal source fluids is most commonly present in the form of $H_3AsO_3$ or as thioarsenite complexes (Webster and Nordstrom, 2003). The oxidation of $As^{3+}$ to $As^{5+}$ happens quickly when reduced fluids come in contact with the atmosphere or are mixed with oxidized water, as for example, in hot spring outflows and receiving rivers (Webster and Nordstrom, 2003). The speciation of As in water as a function of the distance from the source is shown in Figure 2.11a. The predominant form of As in the Falshivaia River water is $As^{5+}$, with $As^{3+}$ being at the 0-13 ppb level. The point at ~ 5.8 km downstream from the headwater has higher $As^{3+}$ due to the input from well #022 (sample name MF 15-06). This well was the subject of hydrothermal explosions in 2003-2004 (Melnikov, 2004) and has been freely discharging hot fluid since then. This fluid enters the Falshivaia River. Exclusively $As^{3+}$ was found in well water samples, with $As^{5+}$< 1ppb. The summary of As speciation in water samples is shown in Table 2.4. By the time fluid mixes with oxygenated water in the Falshivaia

River, $S^{2-}$ drops to below detection limit due to its oxidation to $SO_4^{2-}$, while some $As^{3+}$, $Fe^{2+}$ and $NH_4^+$ can still be found. There is a positive correlation between the reduced forms of As, N and Fe ($As^{3+}$, $NH_4^+$ and $Fe^{2+}$) as observed in Figure 2.11b. These observations are consistent with an oxidation sequence of S→As/N→Fe. This sequence is in agreement with the tabulated redox potentials in natural waters for S, As and N species:

$SO_4^{2-} + 10H^+ + 8e^- \leftrightarrow H_2S + 4H_2O$ Eh = -0.221 V (Schlesinger, 1997)

$H_3AsO_4 + 2H^+ + 2e^- \leftrightarrow HAsO_2 + 2H_2O$ Eh = 0.560 V (Lide, 1993)

$2NO_3^- + 6H^+ + 6e^- \leftrightarrow N_2 + 3H_2O$ Eh = 0.747 V (Schlesinger, 1997)

However, the tabulated redox potential for the $Fe^{2+}/Fe^{3+}$ redox couple suggests that $Fe^{2+}$ should be oxidized before $NH_4^+$ and $As^{3+}$:

$Fe(OH)_3 + 3H^+ + e^- \leftrightarrow Fe^{2+} + 3H_2O$ Eh = -0.047 V (Schlesinger, 1997).

The observed discrepancy can be explained by the fact that the predominant source of $Fe^{2+}$ in the Falshivaia River water is not the hydrothermal fluid from the productive wells. The average content of dissolved $Fe^{2+}$ in the field samples was between 0.02-0.06 ppm in the well steam, well water, Falshivaia River and waste waters, while in the hot-spring waters the average concentration of $Fe^{2+}$ was 0.25 ppm (Table 2.4). There are multiple sources of the hot-spring waters (as opposed to the waste fluids) to the Falshivaia River contributing to the elevated $Fe^{2+}$ content downstream from the power plant.

Antimony originating from a geothermal source is also expected to be in the reduced form: $HSb_2S_4^-$ or $Sb(OH)_3$ (Spycher and Reed, 1989). We analyzed 8 water samples, where Sb was above the ICP-MS detection limit (>1 ppb), and found that the predominant form for aqueous antimony was $Sb^{5+}$ in both source (well water) and mixed waters. There possibly was some $Sb^{3+}$ in well water; however, we were not able to quantify it due to poor peak resolution for $Sb^{3+}$. The detection limit for $Sb^{3+}$ was ~5 ppb, and all the analyzed samples were below it. Further testing has shown that while HCl is an appropriate preservative for $As^{3+}/As^{5+}$ redox couple, it was likely not sufficient for preventing $Sb^{3+}$ oxidation to $Sb^{5+}$.

*2.4.3 Sediment chemistry and speciation*

The XRD analysis of the < 63 μm fraction of the bottom sediment showed the presence of volcanic plagioclase, stilbite and quartz as major components along with a lesser fraction of clay minerals, identified as montmorillonite.

The oxidation state of arsenic in the bottom sediments was determined using linear combination analysis of sample XANES spectra fit using the spectra of the two model compounds sodium meta-arsenite and sodium arsenate. Both $As^{3+}$ and $As^{5+}$ were found in the sediments affected by the waste fluid release (Figure 2.12, Table 2.5). Based on our data, the ratio between aqueous $As^{3+}$ and sediment $As^{3+}$ (0.04-10.6), compared to the ratio of the aqueous $As^{5+}$ and sediment $As^{5+}$ (0.09-93.1) are on the same order of magnitude and $As^{5+}$ has only slightly higher affinity towards the bottom sediments. The total As content in water and sediment are positively correlated (Figure 2.13) possibly indicating that adsorption to the bottom sediments is relatively fast; an outlier on this graph is sample MF 31-06 from one of the settling ponds; it is characterized by high dissolved As content, and limited amount of sediment phase available for adsorption. There is also a correlation between the oxidation state of As in the aqueous and sediment phases (Figure 2.14), however only seven sediment samples were analyzed for As speciation using XANES.

As indicated by the arsenic speciation analysis discussed above, the primary sources of arsenic into the surface environment are the high temperature hydrothermal fluids in which the speciation is dominated by the reduced $As^{3+}$ form. To determine whether well fluid is oversaturated with respect to the secondary mineral phases likely to precipitate under surface conditions we calculated the saturation indexes using the Visual MINTEQ interface, version 2.61 (Gustafsson, 2007) and standard minteq thermodynamic database. As an input we used concentrations of major ions, pH and temperature measured in situ (Table 2.1), and concentration of Fe and Al (Table 2.6) in well fluid. These calculations indicate that the concentrations of dissolved Al and Fe result in oversaturation of the fluid with respect to Al hydroxide phases like gibbsite and diaspore (Table 2.7). After the fluid is exposed to oxidizing surface conditions ($Fe^{2+}$ is oxidized to

$Fe^{3+}$) the fluids become oversaturated with respect to ferrihydrite and other Fe oxide phases in addition to the Al-rich phases (Table 2.7). As noted by other researchers (Taran et al., 1986) the deep well fluid is also characterized by high (up to 1 g/l) $H_4SiO_4$ content and colloidal silica is often observed in cooling well fluid. Therefore the secondary mineral formation is likely during cooling and oxidation of the spent well fluid.

The molar ratio of dissolved Al/Fe in well water samples varied from 4 to ~ 400 (Table 2.6), was between 2 and 7 in the Falshivaia River water, and between 0.1 and 15 in the hot spring water samples. Due to a large range of geochemical conditions in the rock alteration zones, the precipitated secondary phases (samples collected around hot-springs by Kotiol Stream, insert in Figure 2.2), have Al/Fe ratios ranging between 1 and 24. However, in the Falshivaia River sediments, this ratio does not vary as much and shows a slight increase between the point upstream from the power plant (distance 0 km from headwater) and downstream, likely indicative of the increased Al input from the waste fluids (Figure 2.15). The chemical composition of sediments and secondary mineral phases is presented in Table 2.8.

Our conceptual model of the As incorporation into the bottom sediment includes rapid cooling of the waste fluids during which Al and Fe (hydr)oxide phases precipitate and As adsorbs to, or co-precipitates with, these phases. This suspended matter then travels downstream and is incorporated in the bottom sediment of the Falshivaia River. In order to identify the predominant sorbent phase, whether it is an Fe- or Al-rich substrate, and in order to evaluate the possibility for the sediments to switch their behavior from being a sink to becoming a source, we used EXAFS spectroscopy to characterize the speciation of arsenic in the sediments.

Several spectroscopic studies on As adsorption indicate that both $As^{3+}$ and $As^{5+}$ can form inner-sphere sorption complexes with both Al- (Arai et al., 2001; Arai and Sparks, 2002; Foster, 1999) and Fe- (hydr)oxide substrates (Cances et al., 2005; Fendorf et al., 1997; Ona-Nguema et al., 2005; Waychunas et al., 1995). The distance between $As^{5+}$ and Al in a bi-dentate corner-sharing complex should be slightly shorter than that

for the analogous $As^{5+}$-Fe complex – 3.2 vs. 3.3 Å (Foster et al., 2003). Since the $As^{3+}$-O bond length is longer compared to the $As^{5+}$-O bond (1.79 vs. 1.69 Å) the resulting experimentally determined distances to the Al or Fe 2nd shell neighbor atom are about 0.1 Å longer (Arai et al., 2001; Voegelin et al., 2007). A number of previous studies have also pointed out that there is significant contribution to the EXAFS spectrum of adsorbed $As^{5+}$ species from the multiple scattering (MS) within the As-tetrahedron (Sherman and Randall, 2003; Voegelin et al., 2007). To a lesser extent, contribution from multiple scattering within $As(III)O_3$ pyramid is also observed for $As^{3+}$ EXAFS data (Ona-Nguema et al., 2005). In a recent publication (Voegelin et al., 2007), a systematic fitting procedure for including MS paths is presented. Briefly, when the Fourier transformed EXAFS spectrum of As sorbed to ferrihydrite was fitted using the theoretical As-Fe single path the resulting fit was worse than if using an As-Al calculated single scattering path, while allowing As-Fe, or As-Al distance to float. When the triangular, collinear and non-collinear multiple scattering paths were included in a constrained manner with fixed degeneracies, half-path lengths, and Debye-Waller parameters (Voegelin et al., 2007) both the As-Al and As-Fe models were improved, and an As-Fe model was improved to a better degree. The authors used this result to conclude that the model with Fe was better; however, there was no explanation whether the decrease of reduced $\chi^2$ and R-factors were statistically significant.

In this study we applied the same approach, using an Al hydroxide-$As^{5+}$ co-precipitate sample as a control. Field samples with sufficient EXAFS data quality included: MF 11-06, MF 29-06, MK 09-06 and MF 15-06. All, except for MF 15-06 are predominantly $As^{5+}$ (Figure 2.12, Table 2.5). The 2nd shell features are present in all the samples, which indicates an inner-sphere mode of As adsorption. The shell-by-shell fitting procedure gave reasonable fits for all samples using either esperanzaite (As-Al 2nd shell) or scorodite (As-Fe 2nd shell) structural models and theoretical calculated single scattering paths (Figures 2.16a and 2.16b). The fitted coordination number for the Al 2nd shell in the Al-As co-precipitate sample was 1.8(6) and is more consistent with the most common sorption complex found for arsenic: bi-nuclear corner-sharing, while for Fe it

was 0.3(6); the distances for As-Al and As-Fe paths are 3.2 and 3.3 Å respectively (Table 2.9). To make a statistical comparison of the two fits we used the procedure outlined by Kelly et al. (Kelly et al., 2008) where if $\frac{\chi_1^2}{\chi_2^2} - 1 \geq 2\sqrt{\frac{2}{\nu}}$ then the fit with $\chi_2^2$ is statistically better compared to the fit with a $\chi_1^2$ at the 95 % confidence level; where ν – number of degrees if freedom - is equal to the number of independent points minus number of variables (Kelly et al., 2008). Both Fe and Al in the 2nd shell gave an R value (mean square misfit) of approximately 0.02-0.03, which indicates reasonable fits. Since no difference in the goodness of fit is seen between models (including in the control sample with no Fe) when the entire dataset is considered (Figures 2.16a and 2.16b), we also fitted an isolated 2nd shell, assuming either Al or Fe along with the constrained MS paths. This approach resulted in statistically different fit models for the Al-As co-precipitate sample when Al vs. Fe paths were considered and an Al 2nd shell neighbor gave a better fit (Figure 2.17, Table 2.10).

The fitting procedure outlined above was used to try and distinguish between Fe and Al in the second shell of the field sample data. There was no statistical difference between Al and Fe fitted in the isolated second shell in MF 11-06 and MK 09-06 samples, which can be a result of noise in the data, or indicate that arsenic is adsorbed to both Al and Fe-rich mineral substrates in the bottom sediment. For the MF 15-06 sample, an As-Al 2nd shell model gave significantly better results, indicating that majority of As in this sample is associated with Al-rich substrates, while for MF 29-06 Fe was a better fit (Table 2.10). The EXAFS spectra and fit results for the field samples are shown in Figures 2.16a and 2.16b and structural data derived from the EXAFS fitting is summarized in Tables 2.9 and 2.10.

## 2.5 Summary

The elevated concentrations of arsenic in both water and sediments are associated with deep geothermal wells, while natural hot water features do not present a significant source of arsenic in the Dachny field. Reduced $As^{3+}$ originating from the waste

geothermal fluid, along with the reduced forms of sulfur, iron and nitrogen become oxidized quickly after mixing with surface water. First, sulfide is oxidized to sulfate, followed by arsenite oxidizing to arsenate simultaneously with ammonium to nitrate, and then ferrous iron is converted into ferric iron. The Eh calculations indicate that the different redox pairs are decoupled, and that the $Fe^{2+}/Fe^{3+}$ ratio in the cold oxygenated surface waters is controlled by the precipitation of $Fe^{3+}$ solid phases. Arsenic is transported downstream in the Falshivaia River in both dissolved form and adsorbed to the bottom sediment. The behavior of both Sb and As is not conservative in the Falshivaia River water as determined by comparing their dilution factors to the conservative $Cl^-$ ion. Both $As^{3+}$ and $As^{5+}$ were found in the bottom sediment, and both species form inner-sphere corner-sharing complexes. Both Al- and Fe-rich mineral phases are playing role in immobilizing arsenic as determined by the EXAFS data analysis. The extent of As transport is ~ 7 km downstream from the source for the dissolved form, while sediment is transported ~ 3 km farther.

**Acknowledgments**

The authors would like to thank Brandon Ilgen, Dr. Ivan I. Chernev, Anatoly Prihodyko, and Seth Mueller for help with field sampling, Dr. Matt Newville for help with collecting EXAFS data, Dr. Rainer Newberry for valuable input in the XRF and XRD data collection and analysis, and Vanessa Ritchie for consultations regarding LC-ICP-MS. We would also like to acknowledge the Inland Northwest Research Alliance (INRA) Fellowship, University of Alaska Fairbanks (UAF) graduate school travel grant, and Dr. John Eichelberger contributions to the funding of the field work. Support was also provided by the National Science Foundation (NSF) grant CHE-0431425.

## References

Ahuja, S. (Ed.), 2008. Arsenic contamination of groundwater: mechanism, analysis & remediation. John Wiley & Sons, Inc., 387 pp.

Aiuppa, A. et al., 2006. Mineral control of arsenic content in thermal waters from volcano-hosted hydrothermal systems: Insights from island of Ischia and Phlegrean Fields (Campanian Volcanic Province, Italy). Chemical Geology, 229(4): 313-330.

Arai, Y., Elzinga, E., Sparks, D., 2001. X-ray absorption spectroscopic investigation of arsenite and arsenate adsorption at the aluminum oxide–water interface. Journal of colloid and interface science, 235(1): 80-88.

Arai, Y., Sparks, D., 2002. Residence time effects on arsenate surface speciation at the aluminum oxide-water interface. Soil Science, 167(5): 303.

Arai, Y., Sparks, D., Davis, J., 2005. Arsenate adsorption mechanisms at the allophane-water interface. Environmental Science & Technology, 39(8): 2537-2544.

Arnórsson, S., 2004. Environmental impact of geothermal energy utilization. Energy, Waste and the Environment: a Geochemical Perspective, 236.

Arnórsson, S., D'Amore, F., 2000. Sampling of geothermal fluids: on-site measurements and sample treatment. In: Arnórsson, S. (Ed.), Isotopic and chemical techniques in geothermal exploration, development and use. IAEA.

ATSDR, U., 2007. Toxicological Profile for Arsenic. In: services, U.S.D.o.h.a.h. (Editor), ATSDR publication TP. Agency for Toxic Substances and Disease Registry.

Ballantyne, J., Moore, J., 1988. Arsenic geochemisty in geothermal systems. Geochimica et cosmochimica acta, 52(2): 475-483.

Beaulieu, B., Savage, K., 2005. Arsenate adsorption structures on aluminum oxide and phyllosilicate mineral surfaces in smelter-impacted soils. Environmental Science & Technology, 39(10): 3571-3579.

Bethke, C., 1998. The Geochemist's Workbench Release 3.0. University of Illinois at Urbana-Champaign, Champaign, IL.

Cances, B. et al., 2005. XAS Evidence of As (V) Association with Iron Oxyhydroxides in a Contaminated Soil at a Former Arsenical Pesticide Processing Plant. Environmental Science & Technology, 39: 24.

Catalano, J., Park, C., Fenter, P., Zhang, Z., 2008. Simultaneous inner-and outer-sphere arsenate adsorption on corundum and hematite. Geochimica et cosmochimica acta, 72(8): 1986-2004.

Chen, P., 1977. Table of key lines in x-ray powder diffraction patterns of mineral in clays and associated rocks. Geological Survey.

Chernev, I.I., 2005. Geothermal and mineral resources of modern volcanism areas. In: Rychagov, S.N. (Editor), International Kuril-Kamchatka field workshop. OTTISK, Petropavlovsk-Kamchatsky, pp. 460.

Chudaev, O.V., 2003. Sostav i uslovia obrazovaniia sovremennih gidrotermalnih sistem Dalnego Vostoka Rossii. Dalnauka, Vladivostok.

Creed, J., Brockhoff, C., Martin, T., 1994. EPA method 200.8, Revision 5.4 Determination of trace elements in waters and wastes by inductively coupled plasma - mass spectrometry. US Environmental Protection Agency.

Delany, J., Lundeen, S., 1990. The LLNL Thermodynamic Database. Lawrence Livermore National Laboratory.

Eaton, A., Franson, M., 2005. Standard methods for the examination of water & wastewater. Amer Public Health Assn.

Felmy, A., Girvin, D., Jenne, E., 1983. MINTEQ: A computer program for calculating aqueous geochemical equilibria. US Environmental Protection Agency, Washington, DC.

Fendorf, S., Eick, M., Grossl, P., Sparks, D., 1997. Arsenate and chromate retention mechanisms on goethite. 1. Surface structure. Environmental Science & Technology, 31(2): 315-320.

Foord, E. et al., 1999. Esperanzaite, NaCa2Al2 (AsO4)2 F4 (OH). 2H2O, a new mineral species from the La Esperanza mine, Mexico: descriptive mineralogy and atomic arrangement. The Canadian Mineralogist, 37: 67-72.

Foster, A., 1999. Partitioning and transformation of arsenic and selenium in natural and laboratory systems, Ph. D. thesis, Stanford Univ., Stanford, California.

Foster, A., 2003. Spectroscopic investigations of arsenic species in solid phases. Arsenic in Ground Water: 27-65.

Foster, A., Brown Jr, G., Parks, G., 2003. X-ray absorption fine structure study of As (V) and Se (IV) sorption complexes on hydrous Mn oxides. Geochimica et cosmochimica acta, 67(11): 1937-1953.

Foster, A., Brown Jr, G., Tingle, T., Parks, G., 1998. Quantitative arsenic speciation in mine tailing using X-ray absorption spectroscopy. American Mineralogist, 83(5-6): 553-568.

Gault, A., Cooke, D., Townsend, A., Charnock, J., Polya, D., 2005. Mechanisms of arsenic attenuation in acid mine drainage from Mount Bischoff, western Tasmania. Science of the Total Environment, The, 345(1-3): 219-228.

Gault, A. et al., 2003. Arsenic speciation in surface waters and sediments in a contaminated waterway: an IC–ICP-MS and XAS based study. Applied Geochemistry, 18(9): 1387-1397.

Gustafsson, J., 2007. Visual Minteq version 2.61. KTH (Royal Institute of Technology), Sweden.

Henke, K., Atwood, D., Blue, L., 2009. Arsenic: Environmental Chemistry, Health Threats and Waste Treatment. Wiley.

Ilgen, A., Rychagov, S., 2007. Mishiak v prirodnih vodah i otrabotannom teplonositele Mutnovskoi geotermalnoi stancii (Kamchatka, Rossiia), Problemi geokhimii endogennih processov i okruzhaiushei sredi, Irkutsk, Russia, pp. 104-108.

Kelly, S., Hesterberg, D., Ravel, B., 2008. Analysis of Soils and Minerals Using X-ray Absorption Spectroscopy. In: Ulery, A., Drees, L. (Eds.), Methods of Soil Analysis: Part 5--Mineralogical Methods.

Kiryukhin, A., Tranbenkova, A., Bortnikova, S., Fazlullin, S., 2005. Gas and Chemical Monitoring of the Mutnovsky (Dachny) Geothermal Field Exploitation (Kamchatka, Russia), World Geothermal Congress, Turkey.

Kiryukhin, A., Xu, T., Pruess, K., Apps, J., Slovtsov, I., 2004. Thermal-hydrodynamic-chemical (THC) modeling based on geothermal field data. Geothermics, 33(3): 349-381.

Kneebone, P., O'Day, P., Jones, N., Hering, J., 2002. Deposition and fate of arsenic in iron-and arsenic-enriched reservoir sediments. Environmental Science & Technology, 36(3): 381-386.

Ladeira, A., Ciminelli, V., Duarte, H., Alves, M., Ramos, A., 2001. Mechanism of anion retention from EXAFS and density functional calculations: Arsenic (V) adsorbed on gibbsite. Geochimica et cosmochimica acta, 65(8): 1211-1217.

Leonov, V., 1989. Structurnie usloviia localizacii visokotemperaturnih gidroterm. Nauka, Moscow, 104 pp.

Lide, D., 1993. CRC handbook of chemistry and physics. CRC press.

Manceau, A., Lanson, M., Geoffroy, N., 2007. Natural speciation of Ni, Zn, Ba, and As in ferromanganese coatings on quartz using X-ray fluorescence, absorption, and diffraction. Geochimica et cosmochimica acta, 71(1): 95-128.

Manning, B., 2005. Arsenic speciation in As(III)- and As(V)-treated soil using XANES spectroscopy. Microchimica Acta, 151(3-4): 181-188.

Manning, B., Fendorf, S., Bostick, B., Suarezs, D., 2002. Arsenic (III) oxidation and arsenic (V) adsorption reactions on synthetic birnessite. Environmental Science & Technology, 36(5): 976-981.

Manning, B.A., Fendorf, S., Goldberg, S., 1998. Surface structures and stability of arsenic(III) on geothite: Spectroscopic evidence for inner-sphere complexes. Environmental Science & Technology, 32(16): 2383-2388.

Melnikov, D.V., 2004. Some Features of Morphology of Hydrothermal Explosions in Area Mutnovsky of Hydrothermal Power Plant Vestnik KRAUNTS 4: 120-124.

Morin, G. et al., 2002. EXAFS evidence of sorbed arsenic (V) and pharmacosiderite in a soil overlying the Echassières geochemical anomaly, Allier, France. Bulletin de la Societe Geologique de France, 173(3): 281.

Newville, M., 2001. IFEFFIT: interactive XAFS analysis and FEFF fitting. Journal of Synchrotron Radiation, 8(2): 322-324.

Newville, M., Livins, P., Yacoby, Y., Rehr, J., Stern, E., 1993. Near-edge x-ray-absorption fine structure of Pb: A comparison of theory and experiment. Physical Review B, 47(21): 14126-14131.

O'Day, P. (Ed.), 2005. Advances in Arsenic Research: Integration of Experimental and Observational Studies and Implications for Mitigation. American Chemical Society, Washington, DC.

Ona-Nguema, G., Morin, G., Juillot, F., Calas, G., Brown Jr, G., 2005. EXAFS analysis of arsenite adsorption onto two-line ferrihydrite, hematite, goethite, and lepidocrocite. Environmental Science & Technology, 39(23): 9147-9155.

Paktunc, D., Foster, A., Laflamme, G., 2003. Speciation and characterization of arsenic in Ketza River mine tailings using X-ray absorption spectroscopy. Environmental Science & Technology, 37(10): 2067.

Pascua, C. et al., 2005. Arsenic-bearing smectite from the geothermal environment. Mineralogical Magazine, 69(5): 897.

Ravel, B., Newville, M., 2005. ATHENA, ARTEMIS, HEPHAESTUS: data analysis for X-ray absorption spectroscopy using IFEFFIT. Journal of Synchrotron Radiation, 12(4): 537-541.

Ravenscroft, P., Brammer, H., Richards, K., 2009. Arsenic Pollution: A global synthesis. Wiley-Blackwell.

Root, R. et al., 2007. Arsenic sequestration by sorption processes in high-iron sediments. Geochimica et cosmochimica acta, 71(23): 5782-5803.

Sakamoto, H., Tomiyasu, T., Yonehara, N., 1990. The contents and distributions of arsenic , antimony , and mercury in the rivers and the hot spring sediments that flow into the northern Kagoshima bay. Kagoshima Daigaku Rigakubu Kiyo, Sugaku, Butsurigaku, Kagaku, 23: 159-167.

Schlesinger, W., 1997. Biogeochemistry, an analysis of global change 2nd edition. Academic Press.

Sherman, D., Randall, S., 2003. Surface complexation of arsenic (V) to iron (III)(hydr) oxides: structural mechanism from ab initio molecular geometries and EXAFS spectroscopy. Geochimica et cosmochimica acta, 67(22): 4223-4230.

Slovtsov, I., 1994. Mineralogo-geokhimicheskie kriterii phiziko-khimicheskih uslovii v nedrah geotermal'nih mestorozhdenii (na primere Mutnovskogo geotermal'nogo mestorozhdenia, Kamchatka), Moscow.

Spycher, N.F., Reed, M.H., 1989. Arsenic(III) and antimony(III) sulfide complexes: An evaluation of stoichiometry and stability from existing experimental data. Geochimica et Cosmochimica Acta 53(9): 2185-2194.

Stefánsson, A., Arnórsson, S., Sveinbjörnsdóttir, A., 2005. Redox reactions and potentials in natural waters at disequilibrium Chemical Geology, 221(3-4): 289-311.

Strawn, D., Doner, H., Zavarin, M., McHugo, S., 2002. Microscale investigation into the geochemistry of arsenic, selenium, and iron in soil developed in pyritic shale materials. Geoderma, 108(3-4): 237-257.

Tagirov, B., Diakonov, I., Devina, O., Zotov, A., 2000. Standard ferric–ferrous potential and stability of FeCl2+ to 90° C. Thermodynamic properties of Fe (aq) 3+ and ferric-chloride species. Chemical Geology, 162(3-4): 193-219.

Takeno, N., 2005. Atlas of Eh-pH diagrams. Intercomparison of thermodynamic databases, Geological Survey of Japan Open File Report, 419.

Taran, Y.A., Pilipenko, V.P., Rozhkov, V.N.M., 1986. Geokhimiia gidrotermalnih rastvorov i gazov Mutnovskoi gidrotermalnoi sistemi, Geotermicheskie i geokhimicheskie issledovaniia visokotemperaturhih gidroterm. Nauka, Moscow.

To, T., Nordstrom, D., Cunningham, K., Ball, J., McCleskey, R., 1999. New method for the direct determination of dissolved Fe (III) concentration in acid mine waters. Environmental Science & Technology, 33(5): 807-813.

Vaughan, D.J., 2006. Arsenic. Elements, 2(2): 71-75.

Voegelin, A., Weber, F., Kretzschmar, R., 2007. Distribution and speciation of arsenic around roots in a contaminated riparian floodplain soil: Micro-XRF element

mapping and EXAFS spectroscopy. Geochimica et cosmochimica acta, 71(23): 5804-5820.

Waychunas, G., Davis, J., Fuller, C., 1995. Geometry of sorbed arsenate on ferrihydrite and crystalline FeOOH: Re-evaluation of EXAFS results and topological factors in predicting sorbate geometry, and evidence for monodentate complexes. Geochimica et cosmochimica acta, 59(17): 3655-3661.

Waychunas, G. et al., 2005. Surface complexation studied via combined grazing-incidence EXAFS and surface diffraction: arsenate on hematite (0001) and (10–12). Analytical and bioanalytical chemistry, 383(1): 12-27.

Webster-Brown, J., Lane, V., 2005a. Modeling seasonal arsenic behavior in the Waikato River, New Zealand. American Chemical Society, pp. 253-266.

Webster-Brown, J.G., Lane, V., 2005b. The Environmental Fate of Geothermal Arsenic in a Major River System, New Zealand World Geothermal Congress, Antalya, Turkey.

Webster, J., Nordstrom, D., 2003. Geothermal arsenic. Arsenic in Ground Water: Geochemistry and Occurrence (AH Welch and KG Stollenwerk, editors). Kluwer Academic Publishers, Boston, USA: 101-125.

Welch, A., Stollenwerk, K., 2003. Arsenic in ground water: geochemistry and occurrence. Kluwer Academic Pub.

Xu, Y., Zhou, G., Zheng, X., 2007. Redetermination of iron (III) arsenate dihydrate. Acta Crystallographica Section E: Structure Reports Online, 63(3): i67-i69.

Zabinsky, S., Rehr, J., Ankudinov, A., Albers, R., Eller, M., 1995. Multiple-scattering calculations of x-ray-absorption spectra. Physical Review B, 52(4): 2995-3009.

Zheng, J., Iijima, A., Furuta, N., 2001. Complexation effect of antimony compounds with citric acid and its application to the speciation of antimony (III) and antimony (V) using HPLC-ICP-MS. Journal of Analytical Atomic Spectrometry, 16(8): 812-818.

Table 2.1 Major and minor element composition of water samples from the Dachny area, Kamchatka, Russia (continued on the next page)

| *Sample ID* | *Sample type* | *pH (±0.5)* | *ORP mV* | *Temp, °C* |
|---|---|---|---|---|
| 029W COND | Well steam | 5.0 | -154 | boiling[a] |
| 029W SEP | Well water | 8.5 | -279 | boiling |
| 42 SEP | Well water | 9.7 | -240 | boiling |
| A2 COND | Well steam | 5.3 | -158 | boiling |
| A2 SEP | Well water | 8.4 | -138 | boiling |
| GK1 COND | Well steam | 5.3 | -140 | boiling |
| GK1 SEP | Well water | 8.0 | -350 | boiling |
| M013 COND | Well steam | 5.7 | -201 | boiling |
| M013 SEP | Well water | 6.5 | -186 | boiling |
| M016 COND | Well steam | 5.4 | -178 | boiling |
| M024 COND | Well steam | 5.4 | -127 | boiling |
| M024 SEP | Well water | 9.0 | -249 | boiling |
| M026 COND | Well steam | 5.2 | -122 | boiling |
| M037 COND | Well steam | 6.0 | -193 | boiling |
| M037 SEP | Well water | 7.8 | -295 | boiling |
| M4E COND | Well steam | 5.0 | -94 | boiling |
| M4E SEP | Well water | 5.0 | -293 | boiling |
| MF 11-06 | Waste | 6.5 | 76 | 16.0 |
| MF 11-06 dup | Waste | 6.8 | 76 | 16.0 |
| MF 12-06 | Falshivaia River | 6.7 | 239 | 4.0 |
| MF 13-06 | Falshivaia River | 6.7 | 189 | 4.0 |
| MF 14-06 | Falshivaia River | 6.1 | 195 | 4.0 |
| MF 15-06 | unseparated well fluid | 6.6 | -27 | 77.0 |
| MF 16-06 | Falshivaia River | 6.5 | 155 | 4.0 |
| MF 17-06 | Small cold stream | | | |
| MF 18-06 | Perevalnii Stream | 6.1 | 240 | 2.0 |
| MF 19-06 | Falshivaia River | 6.6 | 194 | 4.0 |
| MF 20-06 | Hot spring | 6.2 | -140 | 88.0 |
| MF 26-06 | unseparated well fluid | 9.1 | | 24.0 |
| MF 27-06 | Falshivaia River | 6.6 | 220 | 2.0 |
| MF 28-06 | unseparated well fluid | 8.9 | -204 | boiling |
| MF 29-06 | Waste | 7.1 | 140 | 25.0 |
| MF 30-06 | Waste | 7.1 | 48 | 13.0 |
| MF 31-06 | Waste | 7.7 | 64 | 63.0 |
| MF 31-06 dup | Waste | 7.8 | 64 | 63.0 |
| MK 01-06 | Kotiol Stream | 5.8 | 302 | 1.0 |
| MK 02-06 | Hot spring | 4.4 | 28 | 7.0 |
| MK 03-06 | Hot spring | 5.6 | -120 | 93.0 |
| MK 04-06 | Hot spring | 3.6 | 85 | 53.0 |
| MK 06-06 | Kotiol Stream | 5.4 | 207 | 25.0 |
| MK 07-06 | Pr. Falshivaia River | 6.4 | 289 | 1.0 |
| MK 08-06 | Pr. Falshivaia River | 6.2 | 243 | 2.0 |
| MK 09-06 | Waste | 7.0 | 211 | 3.0 |
| MK 10-06 | Pr. Falshivaia River | 5.8 | 195 | 3.0 |
| MUT 24-06 | Hot spring | 6.9 | 74 | 23.0 |
| MUT 25-06 | Hot spring | 6.3 | 75 | 26.0 |
| MV 23-06 | Mutnovsky crater | 0.1 | 312 | boiling |

Table 2.1 *Continued*

| ***Sample ID*** | ***F ppm (±0.15)*** | ***$Cl^-$ ppm (±0.25)*** | ***$Br^-$ ppm (±0.53)*** | ***$NO_3^-$ ppm (±0.99)*** | ***$PO_4^{3-}$ ppm (±3.20)*** | ***$SO_4^{2-}$ ppm (±1.10)*** | ***$S^{2-}$ ppm (±10%)*** | ***$HCO_3^-$ mg $CaCO_3$ (±10%)[c]*** |
|---|---|---|---|---|---|---|---|---|
| 029W COND | ldl[b] | 0.11 | 0.01 | ldl | 9.29 | 6.01 | 3.02 | <0.01 |
| 029W SEP | 2.43 | 199.69 | 0.67 | ldl | ldl | 172.93 | 5.65 | 43.9 |
| 42 SEP | 3.62 | 223.43 | 0.46 | ldl | ldl | 207.74 | 0.87 | 115.1 |
| A2 COND | ldl | 0.09 | 0.01 | ldl | 11.16 | 9.11 | 4.60 | <0.01 |
| A2 SEP | 2.48 | 274.32 | 0.63 | 1.49 | ldl | 110.20 | 0.93 | 55.0 |
| GK1 COND | ldl | 0.24 | ldl | 0.27 | 7.71 | 4.17 | 2.90 | 0.4 |
| GK1 SEP | 2.58 | 214.75 | 0.74 | ldl | 19.21 | 166.92 | 2.17 | 53.9 |
| M013 COND | ldl | 0.28 | 0.00 | ldl | 27.66 | 9.12 | 1.50 | <0.01 |
| M013 SEP | 0.79 | 78.29 | 0.13 | ldl | 36.57 | 47.26 | 3.10 | 3.2 |
| M016 COND | 0.01 | 0.19 | ldl | 0.07 | 23.71 | 8.75 | 2.75 | 0.3 |
| M024 COND | ldl | 0.12 | 0.02 | ldl | 6.56 | 4.60 | 3.02 | 0.2 |
| M024 SEP | 3.14 | 214.94 | 0.59 | ldl | ldl | 228.09 | 3.39 | 75.1 |
| M026 COND | ldl | 0.02 | ldl | 0.14 | 23.40 | 6.72 | 8.53 | 0.6 |
| M037 COND | ldl | 0.10 | ldl | ldl | 34.17 | 9.13 | 2.50 | 0.2 |
| M037 SEP | 2.70 | 230.92 | 0.43 | ldl | 39.05 | 133.88 | 5.97 | 69.5 |
| M4E COND | 0.01 | 0.19 | 0.01 | ldl | 8.26 | 4.03 | 3.52 | <0.01 |
| M4E SEP | 2.97 | 191.13 | 0.46 | ldl | ldl | 205.85 | 4.90 | 64.0 |
| MF 11-06 | 0.43 | 35.10 | 0.07 | 5.99 | ldl | 38.04 | ldl | 8.6 |
| MF 11-06 dup | 0.43 | 34.67 | 0.06 | 5.53 | ldl | 37.59 | ldl | 8.9 |
| MF 12-06 | 0.08 | 4.43 | ldl | 0.73 | ldl | 4.78 | ldl | 6.5 |
| MF 13-06 | 0.13 | 7.98 | 0.02 | 0.27 | ldl | 8.29 | ldl | 4.6 |
| MF 14-06 | 0.09 | 4.84 | 0.01 | 0.17 | ldl | 5.05 | ldl | 4.7 |
| MF 15-06 | 1.35 | 290.53 | 0.94 | ldl | 20.49 | 205.66 | 0.77 | 5.7 |
| MF 16-06 | 0.06 | 3.64 | ldl | 1.24 | ldl | 4.89 | ldl | 2.6 |
| MF 17-06 | 0.04 | 1.20 | ldl | 0.18 | ldl | 8.81 | | |
| MF 18-06 | 0.02 | 0.62 | ldl | ldl | ldl | 3.52 | ldl | 1.2 |
| MF 19-06 | 0.03 | 1.15 | ldl | 0.04 | ldl | 3.50 | ldl | 2.3 |
| MF 20-06 | 0.11 | 1.57 | ldl | 0.36 | 38.64 | 60.49 | 0.18 | 1.4 |
| MF 26-06 | 5.96 | 165.95 | 0.60 | ldl | ldl | 283.00 | 2.53 | 179.8 |
| MF 27-06 | 0.04 | 1.67 | ldl | ldl | ldl | 2.27 | ldl | 5.2 |
| MF 28-06 | 2.97 | 234.10 | ldl | ldl | ldl | 179.88 | 0.98 | 81.5 |
| MF 29-06 | 0.64 | 47.05 | ldl | 0.58 | ldl | 85.60 | ldl | 11.0 |
| MF 30-06 | 0.06 | 1.00 | 0.00 | ldl | ldl | 5.99 | 0.28 | 6.4 |
| MF 31-06 | 2.89 | 271.31 | 0.90 | ldl | ldl | 128.02 | ldl | 33.8 |
| MF 31-06 dup | 2.82 | 274.11 | 0.57 | ldl | ldl | 128.10 | ldl | 32.3 |
| MK 01-06 | 0.02 | 0.58 | ldl | 0.06 | ldl | 5.20 | ldl | 0.2 |
| MK 02-06 | 0.03 | 0.62 | ldl | 0.11 | ldl | 9.15 | 0.59 | <0.01 |
| MK 03-06 | 0.11 | 1.02 | 0.09 | 0.05 | ldl | 106.19 | 0.39 | 0.1 |
| MK 04-06 | 0.03 | 0.39 | ldl | 0.02 | ldl | 35.29 | 0.42 | <0.01 |
| MK 06-06 | 0.03 | 0.63 | ldl | 0.15 | ldl | 8.72 | ldl | 1.0 |
| MK 07-06 | 0.02 | 0.52 | 0.00 | 0.14 | ldl | 1.06 | ldl | 2.2 |
| MK 08-06 | 0.02 | 0.53 | ldl | 0.55 | ldl | 2.29 | ldl | 1.4 |
| MK 09-06 | 0.10 | 1.10 | ldl | 0.52 | ldl | 4.06 | ldl | 7.1 |
| MK 10-06 | 0.02 | 0.55 | ldl | 0.07 | ldl | 4.15 | ldl | <0.01 |
| MUT 24-06 | 0.08 | 1.60 | ldl | 0.26 | ldl | 16.76 | 0.23 | 17.7 |
| MUT 25-06 | 0.10 | 1.22 | ldl | 0.07 | ldl | 26.95 | 0.04 | 2.6 |
| MV 23-06 | 28.24 | 26851 | ldl | ldl | 22.57 | 2649.65 | 0.15 | <0.01 |

Table 2.1 *Continued*

| *Sample ID* | *$Li^+$ ppm (±0.07)* | *$Na^+$ ppm (±0.35)* | *$NH_4^+$ ppm (±0.08)* | *$K^+$ ppm (±0.43)* | *$Mg^{2+}$ ppm (±2.34)* | *$Ca^{2+}$ ppm (±0.40)* | *$Fe_{total}$ ppm (±10%)* | *charge balance %* |
|---|---|---|---|---|---|---|---|---|
| 029W COND | 0.04 | 0.16 | 3.84 | 0.15 | 0.00 | 0.02 | 0.01 | 3 |
| 029W SEP | 1.20 | 205.34 | 0.10 | 26.21 | ldl | 2.25 | 0.01 | 0 |
| 42 SEP | 1.38 | 257.31 | 0.06 | 31.79 | ldl | 1.96 | 0.04 | 1 |
| A2 COND | 0.00 | 0.05 | 5.92 | 0.11 | 0.00 | 0.02 | 0.04 | 5 |
| A2 SEP | 0.45 | 198.52 | 0.24 | 31.99 | ldl | 1.69 | 0.01 | -6 |
| GK1 COND | | 0.12 | 4.01 | 0.14 | 0.00 | 0.04 | 0.01 | 14 |
| GK1 SEP | 0.30 | 216.37 | 0.21 | 32.53 | ldl | 3.05 | 0.01 | 0 |
| M013 COND | 0.01 | 0.23 | 8.68 | 0.10 | 0.00 | 0.03 | 0.02 | 2 |
| M013 SEP | 0.52 | 63.36 | 4.41 | 9.97 | ldl | 0.41 | 0.09 | -4 |
| M016 COND | 0.00 | 0.43 | 8.05 | 0.12 | 0.00 | 0.03 | 0.02 | 4 |
| M024 COND | 0.00 | 0.28 | 3.01 | 0.12 | 0.02 | 0.03 | 0.01 | 6 |
| M024 SEP | 1.34 | 247.38 | 0.03 | 30.87 | ldl | 2.98 | 0.02 | 0 |
| M026 COND | 0.00 | 0.02 | 7.23 | 0.03 | 0.06 | 0.02 | 0.02 | 3 |
| M037 COND | 0.00 | 0.11 | 10.99 | 0.08 | 0.00 | 0.02 | 0.02 | 6 |
| M037 SEP | 1.22 | 206.59 | 0.47 | 27.92 | ldl | 1.15 | 0.03 | -4 |
| M4E COND | 0.00 | 0.30 | 3.39 | 0.06 | 0.00 | 0.02 | 0.02 | 10 |
| M4E SEP | 1.19 | 222.90 | 0.08 | 27.31 | ldl | 2.27 | 0.01 | 0 |
| MF 11-06 | 0.16 | 35.59 | 0.04 | 6.24 | 0.12 | 1.65 | 0.08 | -4 |
| MF 11-06 dup | 0.15 | 35.15 | 1.14 | 5.89 | 0.12 | 1.59 | 0.20 | -3 |
| MF 12-06 | 0.01 | 5.90 | 0.02 | 1.09 | 0.12 | 1.02 | 0.03 | 6 |
| MF 13-06 | 0.05 | 9.05 | 0.10 | 1.61 | 0.08 | 0.73 | 0.05 | 4 |
| MF 14-06 | 0.03 | 5.88 | 0.01 | 1.01 | 0.06 | 0.62 | 0.01 | 4 |
| MF 15-06 | 0.15 | 188.45 | 14.94 | 28.61 | 1.41 | 20.40 | 0.23 | -7 |
| MF 16-06 | 0.01 | 3.43 | 0.14 | 0.72 | 0.14 | 1.33 | 0.01 | 0 |
| MF 17-06 | 0.00 | 1.03 | 0.01 | 0.19 | 0.31 | 2.95 | | 1 |
| MF 18-06 | 0.00 | 0.61 | ldl | 0.15 | 0.10 | 1.25 | 0.00 | -1 |
| MF 19-06 | 0.00 | 1.33 | 0.00 | 0.32 | 0.10 | 1.16 | 0.02 | 1 |
| MF 20-06 | 0.00 | 16.46 | 5.28 | 5.28 | 1.06 | 6.53 | 0.04 | -5 |
| MF 26-06 | 1.28 | 275.62 | ldl | 30.81 | 0.21 | 2.02 | 0.05 | 1 |
| MF 27-06 | 0.00 | 2.35 | ldl | 0.52 | 0.19 | 1.10 | | 11 |
| MF 28-06 | 1.35 | 245.23 | 0.03 | 32.05 | ldl | 2.08 | 0.03 | 2 |
| MF 29-06 | 0.20 | 61.12 | 6.12 | 7.76 | 0.09 | 1.75 | 0.12 | 1 |
| MF 30-06 | 0.00 | 3.34 | ldl | 0.95 | 0.25 | 1.38 | 0.08 | 9 |
| MF 31-06 | 1.46 | 213.91 | 0.05 | 32.80 | 0.08 | 2.12 | 0.03 | -2 |
| MF 31-06 dup | 0.00 | 213.99 | 0.07 | 32.66 | ldl | 1.57 | 0.07 | -3 |
| MK 01-06 | 0.00 | 0.59 | ldl | 0.11 | 0.18 | 1.26 | 0.02 | -9 |
| MK 02-06 | 0.00 | 0.69 | 0.04 | 0.18 | 0.23 | 1.63 | 0.05 | -8 |
| MK 03-06 | 0.00 | 15.71 | 6.58 | 7.00 | 1.47 | 13.40 | 0.25 | -5 |
| MK 04-06 | 0.00 | 2.40 | 1.02 | 0.94 | 0.52 | 3.00 | 0.40 | -8 |
| MK 06-06 | 0.00 | 0.98 | 0.10 | 0.30 | 0.25 | 1.82 | 0.04 | -11 |
| MK 07-06 | 0.00 | 0.47 | 0.01 | 0.11 | 0.05 | 0.64 | 0.00 | -2 |
| MK 08-06 | 0.00 | 0.59 | 0.02 | 0.15 | 0.08 | 0.87 | 0.01 | -3 |
| MK 09-06 | 0.00 | 3.07 | 0.04 | 0.74 | 0.09 | 1.97 | 0.01 | 13 |
| MK 10-06 | 0.00 | 0.88 | 0.02 | 0.20 | 0.13 | 1.17 | 0.10 | 6 |
| MUT 24-06 | 0.00 | 6.59 | 0.07 | 4.29 | 1.40 | 5.18 | 0.18 | 15 |
| MUT 25-06 | 0.00 | 5.95 | 1.09 | 2.87 | 0.82 | 3.02 | 0.65 | 0 |
| MV 23-06 | | 111.32 | 2.85 | 131.88 | 26.52 | 166.50 | 0.33 | 0 |

[a] pH was measured when samples cooled to <50 °C; [b] < detection limit; [c] for alkalinity <5 mg/l $CaCO_3$ error is ±20%

Table 2.2 Summary of Eh calculation using three redox couples $Fe^{2+}/Fe^{3+}$, $H_2S/SO_4^{2-}$ and $NO_3^-/HN_4^+$

| Redox couple | Calculation | Reaction | Reference for thermo data |
|---|---|---|---|
| $Fe^{2+}$ $Fe^{3+}$ | $Eh = Eh^0 + \frac{2.3RT}{F}\log\frac{[Fe^{3+}]}{[Fe^{2+}]}$ | $Fe^{3+} + e^- \leftrightarrow Fe^{2+}$ | Tagirov et al., 2000 |
| $H_2S$ $SO_4^{2-}$ | $Eh = \frac{0.2875RT}{F}\left(\log\frac{[SO_4^{2-}]}{[H_2S]} - 10pH - \log K\right)$ | $H_2S(aq)+4H_2O \leftrightarrow SO_4^{2-}+10H^++8e^-$ | Stefánsson et al., 2005 |
| $NO_3^-$ $NH_4^+$ | $Eh = \frac{0.2875RT}{F}\left(\log\frac{[NO_3^-]}{[NH_4^+]} - 10pH - \log K\right)$ | $NH_4^+ + 2H_2O \leftrightarrow NO_3^- + 10H^+ + 8e^-$ | Stefánsson et al., 2005 |

Table 2.3 Antimony content in different water types in the Dachny geothermal area

| Sample | Sb, ppb | Sample type |
|---|---|---|
| MF 14-06 | 2.4 | Falshivaia River |
| MF 13-06 | 4.6 | Falshivaia River |
| MF 12-06 | 1.7 | Falshivaia River |
| MF 16-06 | 1.0 | Falshivaia River |
| MF 19-06 | 0.0 | Falshivaia River |
| MK 09-06 | 1.2 | Waste water |
| MF 29-06 | 32.6 | Waste water |
| MF 31-06 | 129.9 | Waste water |
| M 037 SEP | 1.7 | Well water |
| 42 SEP | 37.3 | Well water |
| M 024 SEP | 1.4 | Well water |
| MF 28-06 | 22.2 | Well fluid |
| MF 26-06 | 25.8 | Well fluid |

Table 2.4 Oxidation state of As (determined by LC-ICP-MS) and Fe (determined by UV VIS) in water samples

| Sample | Category | As(III) ppb | As(V) ppb | As total ppb | Fe(II) ppm | Fe(III) ppm |
|---|---|---|---|---|---|---|
| M016 COND | Well Steam | <1 ppb | <1 ppb | <1 ppb | 0.018 | 0.003 |
| M013 COND | Well Steam | 3.0 | <1 ppb | 3.0 | 0.012 | 0.004 |
| 029W COND | Well Steam | 2.8 | <1 ppb | 2.8 | 0.008 | 0.001 |
| A2 COND | Well Steam | 2.6 | <1 ppb | 2.6 | 0.016 | 0.020 |
| M4E COND | Well Steam | 5.1 | <1 ppb | 5.1 | 0.021 | 0.002 |
| MF 19-06 | Falshivaia river | <1 ppb | 7.7 | 8.0 | 0.013 | 0.004 |
| MF 27-06 | Falshivaia river | <1 ppb | 6.5 | 6.5 | | |
| MF 16-06 | Falshivaia river | 13.0 | 29.6 | 42.6 | 0.010 | 0.001 |
| MF 12-06 | Falshivaia river | 7.8 | 64.4 | 72.2 | 0.021 | 0.012 |
| MF 14-06 | Falshivaia river | 17.5 | 79.1 | 96.6 | 0.010 | 0.005 |
| MF 13-06 | Falshivaia river | 13.3 | 136.6 | 150.0 | 0.026 | 0.023 |
| MF 20-06 | Hot spring | 1.2 | <1 ppb | 1.2 | 0.039 | 0.000 |
| MK 05-06 | Hot spring | <1 ppb | <1 ppb | <1 ppb | 0.413 | 0.045 |
| MUT 25-06 | Utinoie lake (hot-springs) | 8.1 | 8.8 | 16.9 | 0.387 | 0.263 |
| MUT 24-06 | Utinoie lake (hot-springs) | 1 | <1 ppb | 0.8 | 0.157 | 0.021 |
| 42 SEP | Well water | 4343 | <1 ppb | 4343 | 0.027 | 0.008 |
| M024 SEP | Well water | 2557 | 2.6 | 2559 | 0.010 | 0.008 |
| M013 SEP | Well water | 407.5 | <1 ppb | 407.5 | 0.089 | 0.000 |
| M37 SEP | Well water | 1912 | <1 ppb | 1912 | 0.026 | 0.005 |
| 4E SEP | Well water | 2265 | <1 ppb | 2265 | 0.013 | 0.000 |
| 029 SEP | Well water | 2085 | <1 ppb | 2085 | 0.010 | 0.001 |
| GK1 SEP | Well water | 2115 | <1 ppb | 2115 | 0.003 | 0.003 |
| A2 SEP | Well water | 3875 | <1 ppb | 3875 | 0.008 | 0.001 |
| MV 22-06 | Mutnovsky volcano | 63.9 | 302.8 | 366.7 | 0.269 | 0.927 |
| MV 21-06 | Mutnovsky volcano | 3.3 | 13.8 | 17.1 | 0.624 | 0.000 |
| MF 30-06 | Waste | <1 ppb | <1 ppb | <1 ppb | 0.079 | 0.005 |
| MK 09-06 | Waste | <1 ppb | 53.8 | 54.5 | 0.007 | 0.003 |
| MF 11-06 | Waste | 1.9 | 756.1 | 758.0 | 0.025 | 0.050 |
| MF 29-06 | Waste | 32.0 | 920.7 | 952.7 | 0.022 | 0.102 |
| MF 31-06 | Waste | <1 ppb | 6461 | 6461 | 0.027 | 0.005 |
| MF 15-06 | Well Fluid | 3494 | <1 ppb | 3494 | 0.218 | 0.011 |
| MF 26-06 | Well Fluid | 9317 | <1 ppb | 9317 | 0.041 | 0.006 |
| MF 28-06 | Well Fluid | 4243 | <1 ppb | 4243 | 0.025 | 0.006 |

Table 2.5 The oxidation state of As in bottom sediments affected by the release of geothermal fluid based on linear combination fitting of XANES spectra

| Sample | As(III), % ±10% | As(V), % ±10% |
|---|---|---|
| MF 11-06 | 19 | 81 |
| MF 15-06 | 56 | 44 |
| MF 31-06 | 15 | 85 |
| MF 29-06 | 3 | 97 |
| MF 13-06 | 0 | 100 |
| MK 09-06 | 0 | 100 |
| MUT 25-06 | 30 | 70 |

Table 2.6 Al/Fe molar ratios in well water

| Sample ID | Fe, μM | Al, μM | Al/Fe | As, ppm |
|---|---|---|---|---|
| 029W SEP | 0.20 | 40.32 | 205 | 0.02 |
| 42 SEP | 0.63 | 60.11 | 96 | 5.52 |
| A2 SEP | 0.16 | 45.16 | 280 | 0.20 |
| GK1 SEP | 0.11 | 45.23 | 421 | 0.10 |
| M013 SEP | 1.58 | 5.98 | 4 | 0.13 |
| M024 SEP | 0.32 | 41.62 | 129 | 0.44 |
| M037 SEP | 0.56 | 49.89 | 90 | 0.01 |
| M4E SEP | 0.23 | 44.55 | 191 | 0.04 |

Table 2.7 Saturation indexes for well water with respect to Al and Fe

| | ***Before oxidation*** | | | | | | | |
|---|---|---|---|---|---|---|---|---|
| **Well** | **M4E** | **M013** | **M037** | **GK1** | **A2** | **029W** | **M024** | **42** |
| Depth, m | 1896 | ~600 | 1771 | ~1200 | ~2000 | 1071 | 1300 | ~1500 |
| pH | 5.0 | 6.5 | 7.8 | 8.0 | 8.4 | 8.5 | 9.0 | 9.7 |
| $Al(OH)_3$ (Soil) | 1.37 | 0.08 | | | | | | |
| Diaspore | 2.72 | 1.42 | 1.15 | 0.91 | 0.51 | 0.36 | | |
| Gibbsite | 1.92 | 0.63 | 0.35 | 0.11 | | | | |
| | ***After oxidation*** | | | | | | | |
| $Al(OH)_3$ (Soil) | 1.37 | 0.08 | | | | | | |
| Diaspore | 2.72 | 1.42 | 1.15 | 0.91 | 0.51 | 0.36 | | |
| Ferrihydrite | 3.05 | 5.02 | 3.53 | 2.56 | 2.34 | 2.32 | 2.03 | 1.65 |
| Gibbsite | 1.92 | 0.63 | 0.35 | 0.11 | | | | |
| Hematite | 11.40 | 15.34 | 12.34 | 10.41 | 9.96 | 9.94 | 9.35 | 8.60 |
| Maghemite | | 2.99 | | | | | | |

Table 2.8 Chemical composition of bottom sediment and clay samples (sample locations are shown in Figures 2.1 and 2.2) (continued on the next page)

| Sample name | Sum (%) | $Na_2O$ (%) | MgO (%) | $Al_2O_3$ (%) | $SiO_2$ (%) | $P_2O_5$ (%) | $K_2O$ (%) | CaO (%) | $TiO_2$ (%) | MnO (%) | $Fe_2O_3$ (%) | S (%) |
|---|---|---|---|---|---|---|---|---|---|---|---|---|
| Bottom sediment (<62 μm fraction) | | | | | | | | | | | | |
| MF 11-06 | 98.85 | 2.42 | 1.85 | 20.1 | 57.77 | 0.41 | 1.4 | 3.53 | 1.36 | 0.1 | 9.33 | 0.20 |
| MF 12-06 | 101.53 | 2.72 | 2.16 | 20.22 | 58.83 | 0.66 | 1.48 | 4.15 | 1.34 | 0.14 | 9.41 | 0.08 |
| MF 13-06 | 100.98 | 3.47 | 1.99 | 19.22 | 59.78 | 0.68 | 1.75 | 4.67 | 1.13 | 0.13 | 7.79 | 0.06 |
| MF 14-06 | 100.77 | 3.49 | 1.88 | 19.21 | 59.77 | 0.68 | 1.84 | 4.46 | 1.14 | 0.13 | 7.81 | 0.05 |
| MF 15-06 | 100.74 | 2.53 | 3.18 | 18.14 | 60.3 | 0.16 | 1.37 | 5.45 | 0.84 | 0.1 | 7.95 | 0.43 |
| MF 16-06 | 103.04 | 2.53 | 2.51 | 19.96 | 60.14 | 0.37 | 1.39 | 4.72 | 1.15 | 0.14 | 9.71 | 0.13 |
| MF 18-06 | 100.36 | 1.49 | 1.97 | 21.26 | 61.32 | 0.24 | 1.49 | 2.36 | 0.95 | 0.09 | 8.7 | 0.27 |
| MF 19-06 | 101.19 | 1.78 | 2.87 | 20.51 | 56.68 | 0.22 | 0.74 | 3.82 | 1.15 | 0.12 | 12.74 | 0.33 |
| MF 20-06 | 98.58 | 2.37 | 1.23 | 21.63 | 56.83 | 0.21 | 1.4 | 2.42 | 1.37 | 0.09 | 9.31 | 1.38 |
| MF 29-06 | 101.62 | 2.26 | 1.32 | 21.9 | 61.22 | 0.43 | 1.24 | 3 | 1.4 | 0.11 | 8.31 | 0.07 |
| MF 30-06 | 100.52 | 1.12 | 1.02 | 25.26 | 57.54 | 0.61 | 1.23 | 1.59 | 1.72 | 0.05 | 9.45 | 0.50 |
| MF 31-06 | 99.57 | 3.07 | 1.49 | 18.91 | 61.14 | 0.42 | 1.64 | 4.17 | 1.16 | 0.12 | 6.89 | 0.06 |
| MK 01-06 | 100.81 | 1.72 | 2.37 | 20.41 | 60.23 | 0.29 | 1.31 | 2.97 | 1.15 | 0.09 | 9.83 | 0.19 |
| MK 02-06 | 98.68 | 1.1 | 1.65 | 23.07 | 57.51 | 0.37 | 1.24 | 1.9 | 1.3 | 0.06 | 9.55 | 0.65 |
| MK 03-06 | 102.13 | 1.5 | 2.16 | 15.92 | 47.44 | 0.14 | 0.99 | 2.7 | 1.68 | 0.12 | 25.78 | 3.37 |
| MK 04-06 | 104.73 | 0.66 | 1.48 | 24.72 | 61.93 | 0.16 | 0.9 | 1.13 | 1.26 | 0.06 | 11.16 | 1.02 |
| MK 05-06 | 102.45 | 0.86 | 1.49 | 22.42 | 61.19 | 0.46 | 1.18 | 1.29 | 1.42 | 0.06 | 10.97 | 0.82 |
| MK 06-07 | 100.23 | 1.86 | 2.66 | 18.78 | 55.31 | 0.33 | 1.26 | 3.43 | 1.47 | 0.1 | 13.76 | 0.99 |
| MK 07-06 | 101.04 | 2.11 | 3.03 | 19.6 | 57.8 | 0.28 | 1.36 | 4.68 | 1.18 | 0.15 | 10.47 | 0.12 |
| MK 08-06 | 100.13 | 1.88 | 2.6 | 20.04 | 57.45 | 0.35 | 1.34 | 3.75 | 1.2 | 0.11 | 11 | 0.15 |
| MK 09-06 | 100.58 | 1.82 | 1.34 | 21.04 | 62.13 | 0.39 | 1.13 | 2.58 | 1.24 | 0.12 | 8.28 | 0.08 |
| MK 10-06 | 100.68 | 2.13 | 2.67 | 19.24 | 55.99 | 0.41 | 1.27 | 4.04 | 1.33 | 0.13 | 12.99 | 0.19 |
| MUT 24-06 | 98.77 | 2.26 | 1.57 | 24 | 54.86 | 0.57 | 1.36 | 3.05 | 1.42 | 0.1 | 9.04 | 0.21 |
| MUT 25-06 | 100.66 | 3.14 | 1.22 | 21.05 | 59.55 | 0.52 | 1.65 | 3.13 | 1.19 | 0.08 | 8.12 | 0.61 |
| MV 21-06 | 99.39 | 1.3 | 1.06 | 12.48 | 71.55 | 0.15 | 0.53 | 2.03 | 1.41 | 0.03 | 6.3 | 2.27 |
| MV 22-06 | 101.91 | 1.23 | 1.09 | 25.07 | 55.58 | 0.25 | 0.49 | 1 | 1.11 | 0.02 | 7.6 | 8.20 |

Table 2.8 *Continued*

| Sample name | Sum (%) | $Na_2O$ (%) | MgO (%) | $Al_2O_3$ (%) | $SiO_2$ (%) | $P_2O_5$ (%) | $K_2O$ (%) | CaO (%) | $TiO_2$ (%) | MnO (%) | $Fe_2O_3$ (%) | S (%) |
|---|---|---|---|---|---|---|---|---|---|---|---|---|
| Secondary mineral phases forming around hot-springs | | | | | | | | | | | | |
| MKC 1-06 | 100.33 | 1.01 | 1.08 | 19.42 | 49.79 | 0.71 | 0.92 | 1.14 | 0.93 | 0.04 | 20.27 | 4.83 |
| MKC 2-06 | 99.32 | 2.43 | 1.65 | 19.15 | 63.77 | 0.22 | 1.84 | 2.61 | 1.64 | 0.07 | 4.86 | 0.78 |
| MKC 4-06 | 102.03 | 1.46 | 1.51 | 21.77 | 62.88 | 0.15 | 1.09 | 1.87 | 1.02 | 0.07 | 8.99 | 1.01 |
| MKC 5-06 | 100.14 | 0.27 | 0 | 9.17 | 85.64 | 0.17 | 0.32 | 0.13 | 2.56 | 0.01 | 0.8 | 0.72 |
| MKC 6-06 | 101.51 | 0.86 | 0.47 | 18.41 | 65.84 | 0.14 | 1.02 | 0.6 | 1.28 | 0.03 | 11.74 | 0.90 |
| MKC 8-06 | 99.22 | 1.55 | 1.47 | 22.02 | 58.24 | 0.15 | 1.17 | 2.33 | 1.1 | 0.06 | 8.19 | 2.69 |
| MKC 9-06 | 99.66 | 1.57 | 1.26 | 19.38 | 60.29 | 1.12 | 1.25 | 2.08 | 0.94 | 0.05 | 11.09 | 0.40 |
| MKC 11-06 | 100.72 | 1.32 | 0.67 | 15.43 | 72.77 | 0.18 | 1.33 | 1.57 | 1.63 | 0.03 | 4.24 | 1.24 |
| MKC 13-06 | 103.11 | 0.12 | 0.25 | 27.92 | 70.26 | 0.04 | 0.44 | 0.06 | 1.32 | 0.01 | 2.44 | 0.06 |
| MKC 19-06 | 99.28 | 0.94 | 0.62 | 30.01 | 47.88 | 0.62 | 0.88 | 1.27 | 1.73 | 0.05 | 9.96 | 4.91 |
| MVC 23-06 | 97.54 | 0.57 | 1.09 | 15.75 | 70.19 | 0.09 | 0.38 | 0.84 | 1.31 | 0.02 | 5.22 | 1.89 |

Table 2.8 *Continued*

| Sample name | As (ppm) | Ba (ppm) | V (ppm) | Cr (ppm) | Cu (ppm) | Zn (ppm) | Rb (ppm) | Sr (ppm) | Zr (ppm) | Pb (ppm) |
|---|---|---|---|---|---|---|---|---|---|---|
| Bottom sediment (<62 μm fraction) | | | | | | | | | | |
| MF 11-06 | 253.5 | 509.6 | 479 | 91.2 | 103.2 | 180.7 | 32.5 | 307.8 | 306.3 | 19.6 |
| MF 12-06 | 91.7 | 358.4 | 469.9 | 41.6 | 99 | 201.9 | 28.9 | 320.6 | 295.4 | 13.4 |
| MF 13-06 | 111.9 | 401.8 | 399.6 | 24.9 | 82.1 | 117.8 | 35 | 340.3 | 285.9 | 23.9 |
| MF 14-06 | 50 | 381.3 | 407.9 | 34.3 | 90.4 | 120 | 32.1 | 327.4 | 297.3 | 15.6 |
| MF 15-06 | 585.8 | 233.9 | 309.8 | 53.8 | 122.1 | 65.4 | 32.6 | 319.6 | 121.8 | 16.5 |
| MF 16-06 | 59.6 | 280.7 | 406.4 | 31.7 | 125.9 | 106 | 26.6 | 341.1 | 194.3 | 12.4 |
| MF 18-06 | 32 | 234.9 | 352.8 | 38.3 | 113.4 | 72 | 27.6 | 217.7 | 148.6 | 15.8 |
| MF 19-06 | 38.3 | 27.7 | 415.2 | 37.3 | 158.5 | 88.3 | 10.1 | 284.7 | 109.6 | 13.9 |
| MF 20-06 | 20 | 486.2 | 473.6 | 28.7 | 78.6 | 215.8 | 23.7 | 262.9 | 381.3 | 19.3 |
| MF 29-06 | 361.2 | 203.1 | 486.2 | 48.7 | 105.1 | 238.9 | 43.9 | 255.8 | 342.2 | 12.4 |
| MF 30-06 | 84.1 | 704.5 | 605.3 | 53 | 110.4 | 113.8 | 24.2 | 360.1 | 461.3 | 24 |
| MF 31-06 | 82.1 | 479.7 | 404.9 | 42.9 | 77.5 | 1021.8 | 40.9 | 324.6 | 308.3 | 12.1 |
| MK 01-06 | 16.7 | 222.7 | 407 | 39 | 114.5 | 87.1 | 24.8 | 266.5 | 185.7 | 12.7 |
| MK 02-06 | 16.6 | 286.8 | 460.7 | 40.4 | 95.6 | 58.6 | 24.1 | 299.1 | 261.7 | 16 |
| MK 03-06 | 9.4 | 202.9 | 582.2 | 75.7 | 119.1 | 173.2 | 16.3 | 253.4 | 306 | 13 |
| MK 04-06 | 10.5 | 258 | 459.8 | 23.6 | 114 | 87.7 | 13.2 | 196.3 | 217.2 | 15.4 |
| MK 05-06 | 9.6 | 339.2 | 501.2 | 29 | 74.6 | 66.5 | 25.1 | 293.6 | 315.6 | 12.5 |
| MK 06-07 | 14.7 | 64 | 525.4 | 72.1 | 119.9 | 83.6 | 23 | 283.8 | 268.7 | 18.1 |
| MK 07-06 | 20.5 | 64.1 | 427.1 | 68.7 | 154.6 | 98.3 | 21.8 | 295.7 | 185.1 | 25.9 |
| MK 08-06 | 23.8 | 173.2 | 436.9 | 50 | 132.7 | 85.3 | 26.5 | 280.9 | 200.5 | 13.9 |
| MK 09-06 | 358.4 | 502.8 | 437.2 | 42.2 | 108.9 | 496.4 | 28 | 233.5 | 295.1 | 108.8 |
| MK 10-06 | 35.2 | 218.6 | 478.1 | 52 | 114.5 | 108.6 | 26.1 | 298 | 237.2 | 16 |
| MUT 24-06 | 25.4 | 386.5 | 492.7 | 34.9 | 118.9 | 122.7 | 30.8 | 264 | 360 | 16.3 |
| MUT 25-06 | 137.6 | 400.5 | 417.1 | 42.9 | 181.1 | 381.4 | 31.5 | 307 | 325.3 | 35.3 |
| MV 21-06 | 47.9 | 503.8 | 504.2 | 43.6 | 95.9 | 43 | 3.6 | 300.7 | 120.7 | 19.3 |
| MV 22-06 | 106.3 | 69.6 | 417.9 | 81.5 | 101.3 | 81.4 | 2.6 | 456.3 | 92.1 | 3.6 |

Table 2.8 *Continued*

| Sample name | As (ppm) | Ba (ppm) | V (ppm) | Cr (ppm) | Cu (ppm) | Zn (ppm) | Rb (ppm) | Sr (ppm) | Zr (ppm) | Pb (ppm) |
|---|---|---|---|---|---|---|---|---|---|---|
| Secondary mineral phases forming around hot-springs | | | | | | | | | | |
| MKC 1-06 | 6.1 | 147 | 355.6 | 30.4 | 129.6 | 40.1 | 16.5 | 151 | 119.8 | 13.3 |
| MKC 2-06 | 0.7 | 333 | 567.2 | 22 | 66 | 40.5 | 26.3 | 382.1 | 245.9 | 7 |
| MKC 4-06 | 15.1 | 207 | 379.5 | 27.8 | 130.6 | 56 | 14.6 | 189.3 | 127.7 | 19.2 |
| MKC 5-06 | 26.8 | 406.4 | 860.9 | | 29.5 | 17.4 | | 217.6 | 424.1 | 33.4 |
| MKC 6-06 | 11.8 | 241.6 | 457 | 22.3 | 85.1 | 30.3 | 12.3 | 191.2 | 201.2 | 14.6 |
| MKC 8-06 | 7.3 | 332.3 | 397.1 | 33.9 | 104.7 | 58.2 | 14.2 | 313.3 | 176.8 | 13.2 |
| MKC 9-06 | 5.2 | 360.3 | 351.9 | 31.5 | 56.7 | 50.9 | 24.2 | 298.8 | 183 | 13.7 |
| MKC 11-06 | 7.9 | 453.4 | 563 | 4.1 | 54.6 | 23.4 | 15.2 | 375.6 | 288.6 | 14.1 |
| MKC 13-06 | 6.9 | 120.9 | 463.4 | 12.7 | 33.5 | 17.9 | 9.6 | 81.6 | 252.8 | 8.9 |
| MKC 19-06 | 52.2 | 271.3 | 625.3 | 101.5 | 202 | 119.7 | 12.8 | 405.9 | 362.9 | 41.7 |
| MVC 23-06 | 38.5 | | 455.6 | 32.5 | 120.4 | 54.3 | 4.7 | 171.2 | 92.8 | 15.5 |

Table 2.9 Summary of the EXAFS fit results for the field samples. The margin of error shown in parentheses represents a 95% confidence level (continued on the next page)

| *Sample* | *FEFF model* | *R-range (Å)* | *k-range* | *Shell* | *N* | *R (Å)* | $\sigma^2$ | *ΔEo* | *R-factor* | *Red* $\chi^2$ | *Indep. Pts* |
|---|---|---|---|---|---|---|---|---|---|---|---|
| ***Al-As-coppt*** | Scorodite | 1.000 - 4.173 | 2.773 - 11.300 | As-O | 4.1(5) | 1.68(2) | 0.001(1) | 4(6) | 0.022 | 9.3 | 16 |
| | | | | As-Fe | 0.3(6) | 3.3(1) | 0.001(6) | | | | |
| | | | | MS-1 | 12 | 3.06 | 0.001 | | | | |
| | | | | MS-2 | 4 | 3.37 | 0.004 | | | | |
| | | | | MS-3 | 12 | 3.38 | 0.002 | | | | |
| | | | | As-O | 4(5) | 4.38(8) | 0.0035 | | | | |
| ***Al-As-coppt*** | Esperanzaite | 1.000 - 4.173 | 2.773 - 11.300 | As-O | 4.0(6) | 1.68(1) | 0.001(1) | 3(3) | 0.026 | 10.8 | 16 |
| | | | | As-Al | 1.8(6) | 3.17(2) | 0.004(5) | | | | |
| | | | | MS-1 | 12 | 3.05 | 0.001 | | | | |
| | | | | MS-2 | 4 | 3.36 | 0.004 | | | | |
| | | | | MS-3 | 12 | 3.36 | 0.002 | | | | |
| | | | | As-O | 3(6) | 4.4(1) | 0.004(9) | | | | |
| ***MF 11-06*** | Scorodite | 1.000-4.100 | 2.778-10.9 | As-O | 3.9(2) | 1.69(1) | 0.003(2) | 4.6(8) | 0.009 | 4 | 16 |
| | | | | As-Fe | 1.4(4) | 3.23(3) | 0.005(2) | | | | |
| | | | | MS-1 | 12 | 3.07 | 0.003 | | | | |
| | | | | MS-2 | 4 | 3.38 | 0.012 | | | | |
| | | | | MS-3 | 12 | 3.39 | 0.006 | | | | |
| | | | | As-O | 8(3) | 4.38(8) | 0.012(8) | | | | |

Table 2.9 *Continued*

| *Sample* | *FEFF model* | *R-range (Å)* | *k-range* | *Shell* | *N* | *R (Å)* | $\sigma^2$ | *ΔEo* | *R-factor* | *Red* $\chi^2$ | *Indep. Pts* |
|---|---|---|---|---|---|---|---|---|---|---|---|
| ***MF 11-06*** | Esperanzaite | 1.00-4.10 | 2.778-10.9 | As-O | 3.7(8) | 1.69(1) | 0.002(2) | 4.2(1) | 0.012 | 5.4 | 16 |
| | | | | As-Al | 1.8(6) | 3.13(3) | 0.002(2) | | | | |
| | | | | MS-1 | 12 | 3.08 | 0.002 | | | | |
| | | | | MS-2 | 4 | 3.39 | 0.008 | | | | |
| | | | | MS-3 | 12 | 3.39 | 0.004 | | | | |
| | | | | As-O | 8(3) | 4.4(1) | 0.01(2) | | | | |
| ***MF 15-06*** | Scorodite | 1.00-4.20 | 3.010-9.016 | As-O | 2.0(8) | 1.67(1) | 0.002(4) | 10(4) | 0.017 | 21.4 | 12 |
| | | | | As-Fe | 0.6(6) | 3.22(6) | 0.007(9) | | | | |
| | | | | MS-1 | 12 | 3.04 | 0.002 | | | | |
| | | | | MS-2 | 2 | 3.34 | 0.008 | | | | |
| | | | | MS-3 | 6 | 3.36 | 0.004 | | | | |
| | | | | As-O | 11(8) | 0.06 | 0.02(6) | | | | |
| ***MF 15-06*** | Esperanzaite | 1.00-4.20 | 3.010-9.016 | As-O | 2.5(4) | 1.67(2) | 0.002(2) | 8(2) | 0.022 | 21.4 | 12 |
| | | | | As-Al | 0.9(3) | 3.07(6) | 0.005(4) | | | | |
| | | | | MS-1 | 12 | 3.04 | 0.002 | | | | |
| | | | | MS-2 | 2 | 3.34 | 0.008 | | | | |
| | | | | MS-3 | 6 | 3.34 | 0.004 | | | | |
| | | | | As-O | 4(4) | 4.42(2) | 0.01(2) | | | | |
| ***MF 29-06*** | Scorodite | 1.14-4.20 | 2.767-9.267 | As-O | 4.0(9) | 1.71(2) | 0.001(2) | 9(4) | 0.04 | 15.6 | 10 |
| | | | | As-Fe | 2.1(8) | 3.31(4) | 0.008(4) | | | | |
| | | | | MS-1 | 12 | 3.1 | 0.001 | | | | |
| | | | | MS-2 | 4 | 3.41 | 0.004 | | | | |
| | | | | MS-3 | 12 | 3.42 | 0.002 | | | | |

Table 2.9 *Continued*

| *Sample* | *FEFF model* | *R-range (Å)* | *k-range* | *Shell* | *N* | *R (Å)* | $\sigma^2$ | *ΔEo* | *R-factor* | *Red* $\chi^2$ | *Indep. Pts* |
|---|---|---|---|---|---|---|---|---|---|---|---|
| ***MF 29-06*** | Esperanzaite | 1.14-4.20 | 2.767-9.267 | As-O | 4.6(8) | 1.68(2) | 0.001(2) | 2(3) | 0.03 | 13.3 | 10 |
| | | | | As-Al | 2(1) | 3.13(4) | 0.003(4) | | | | |
| | | | | MS-1 | 12 | 3.06 | 0.001 | | | | |
| | | | | MS-2 | 4 | 3.37 | 0.004 | | | | |
| | | | | MS-3 | 12 | 3.37 | 0.002 | | | | |
| ***MK 09-06*** | Scorodite | 1.00-4.20 | 1.868-10.165 | As-O | 4.7(4) | 1.68(2) | 0.0004(7) | 8(1) | 0.02 | 6.7 | 16 |
| | | | | As-Fe | 2(1) | 3.31(4) | 0.006(4) | | | | |
| | | | | MS-1 | 12 | 3.06 | 0.0004 | | | | |
| | | | | MS-2 | 4 | 3.37 | 0.0016 | | | | |
| | | | | MS-3 | 12 | 3.38 | 0.0008 | | | | |
| | | | | As-O | 9(6) | 4.44(5) | 0.004(6) | | | | |
| ***MK 09-06*** | Esperanzaite | 1.00-4.20 | 1.868-10.165 | As-O | 4.5(6) | 1.68(2) | 0.0001(6) | 7(1) | 0.02 | 7.2 | 16 |
| | | | | As-Al | 2(1) | 3.16(3) | 0.003(4) | | | | |
| | | | | MS-1 | 12 | 3.06 | 0.0001 | | | | |
| | | | | MS-2 | 4 | 3.37 | 0.0004 | | | | |
| | | | | MS-3 | 12 | 3.37 | 0.0002 | | | | |
| | | | | As-O | 9(6) | 4.45(6) | 0.003(6) | | | | |

Table 2.10 Summary of the isolated 2nd shell fits for the field samples and Al-As co-precipitate control sample; the error shown in parentheses represents a 95% confidence level

| *Sample* | *2nd shell* | *R-range (Å)* | *N* | *R (Å)* | *$\sigma^2$* | *R-factor* | *Red $\chi^2$* | *Indep. Pts* |
|---|---|---|---|---|---|---|---|---|
| ***Al-As-coppt*** | Al | 2.296 - 3.230 | 1.8(6) | 3.17(2) | 0.004(5) | 0.05 | 1.00 | 5 |
| | Fe | 2.296 - 3.230 | 0.3(6) | 3.3(1) | 0.001(6) | 0.22 | 4.10 | 5 |
| ***MF 11-06*** | Al | 2.104 - 3.289 | 1.8(6) | 3.13(3) | 0.002(2) | 0.08 | 4.14 | 6 |
| | Fe | 2.104 - 3.289 | 1.4(4) | 3.23(3) | 0.005(2) | 0.11 | 6.06 | 6 |
| ***MF 15-06*** | Al | 2.102 - 3.201 | 0.9(3) | 3.07(6) | 0.005(4) | 0.04 | 3.65 | 4 |
| | Fe | 2.102 - 3.201 | 0.6(6) | 3.22(6) | 0.007(9) | 0.28 | 25.4 | 4 |
| ***MF 29-06*** | Al | 2.346 - 3.450 | 2(1) | 3.13(4) | 0.003(4) | 0.197 | 10.69 | 4 |
| | Fe | 2.346 - 3.450 | 2.1(8) | 3.31(4) | 0.008(4) | 0.059 | 3.19 | 4 |
| ***MK 09-06*** | Al | 2.337 - 3.576 | 2(1) | 3.16(3) | 0.003(4) | 0.16 | 5.2 | 6 |
| | Fe | 2.337 - 3.576 | 2(1) | 3.31(4) | 0.006(4) | 0.17 | 5.5 | 6 |

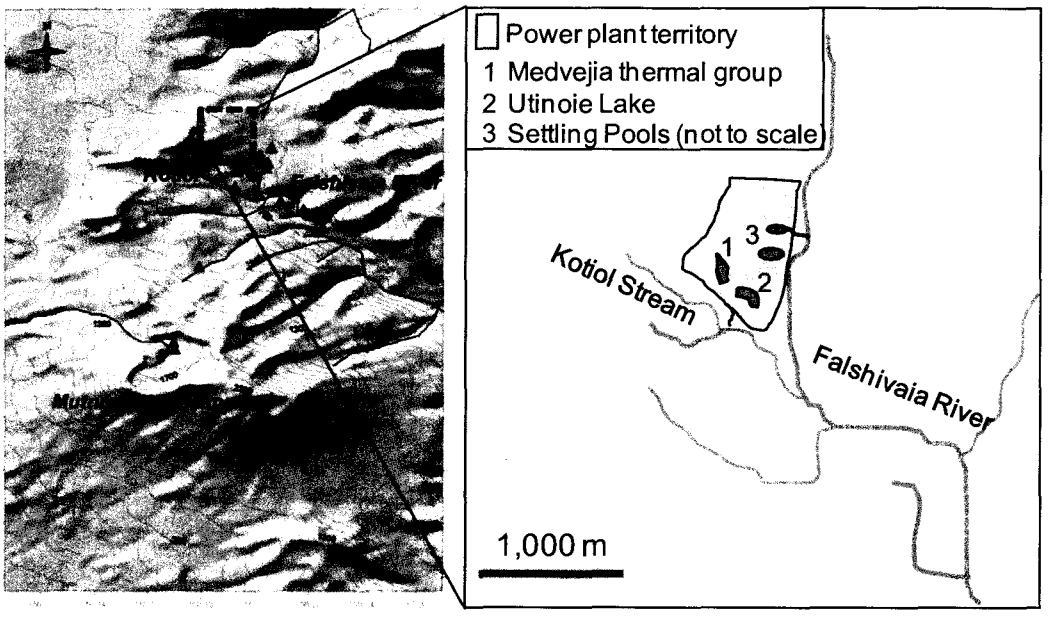


Figure 2.1 Map of the study area. The sampling locations are shown as triangles; the power plant territory is outlined with a rectangle. The plant is located at the head of the Falshivaia River; Insert: sampling locations discussed in text

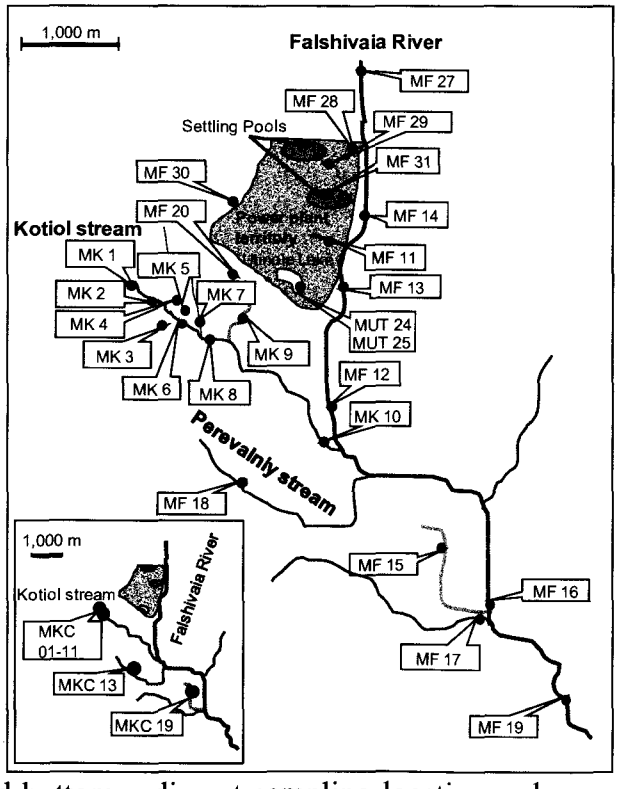


Figure 2.2 Water and bottom sediment sampling locations; clay samples around natural geothermal features are shown in the insert

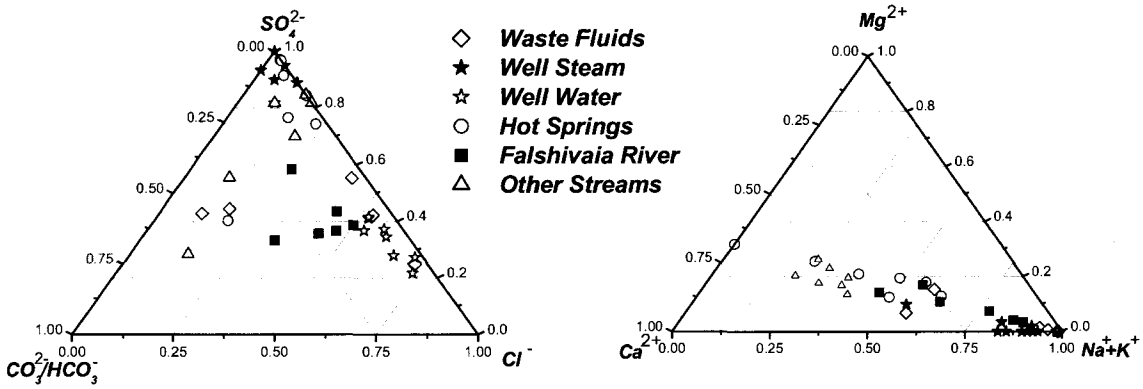


Figure 2.3 Ternary diagrams of water samples from the Dachny area

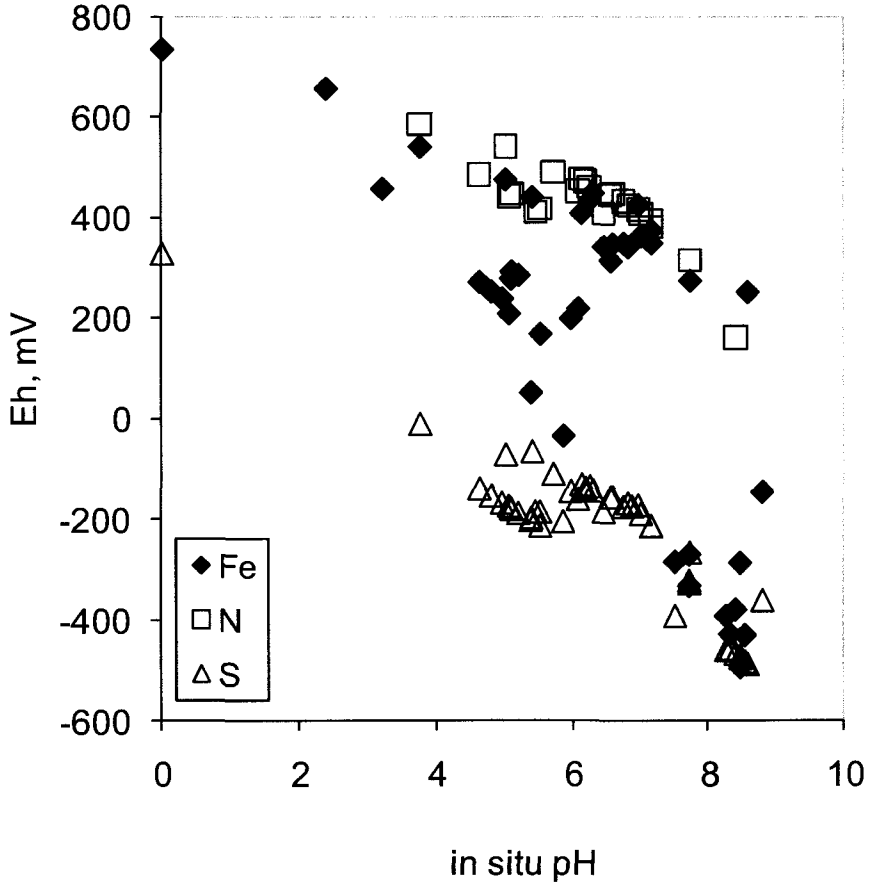


Figure 2.4 Calculated $E_H$ vs. in situ pH

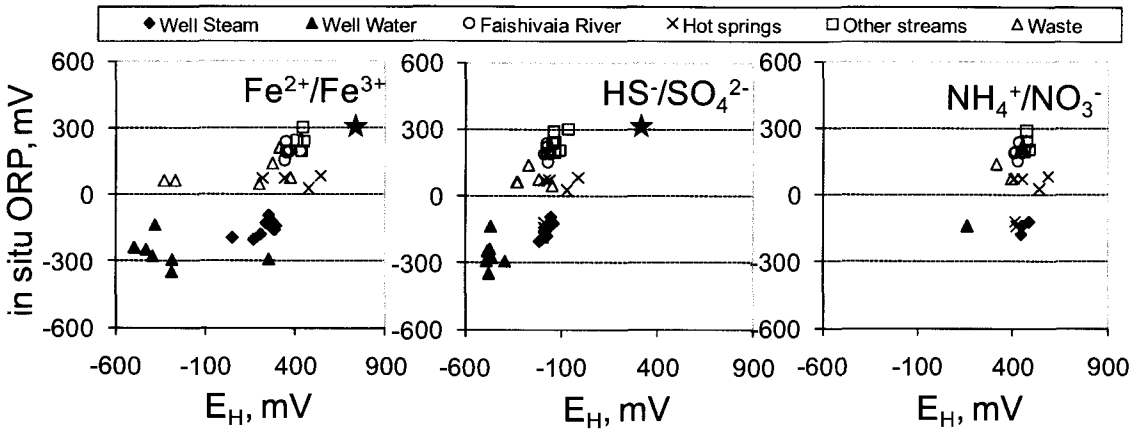


Figure 2.5 Correlation between in situ ORP and calculated $E_H$

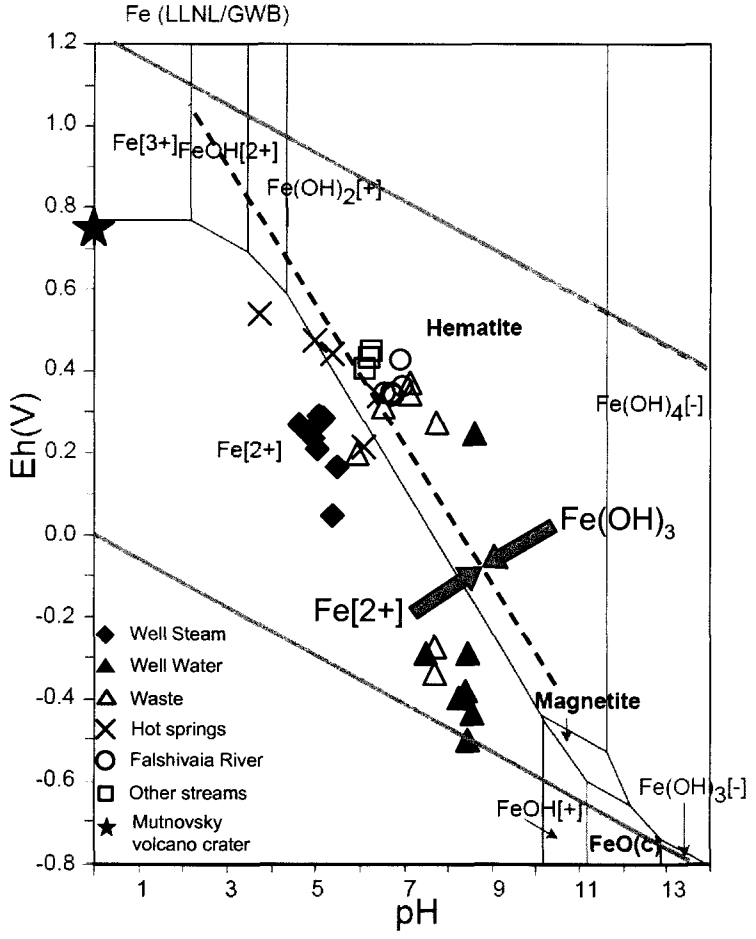


Figure 2.6 $E_H$/pH diagram from Takeno (2005) ($Fe_{total}$ = 1 nM, at 25°C and $10^5$ Pa) is shown as solid lines; dashed line represents boundary between aqueous $Fe^{2+}$ and amorphous $Fe(OH)_3$ ($Fe_{total}$ = 1 μM at 15 °C and $10^5$ Pa). $E_H$ calculated based on $Fe^{2+}/Fe^{3+}$ couple indicates that surface waters are in equilibrium with amorphous $Fe(OH)_3$

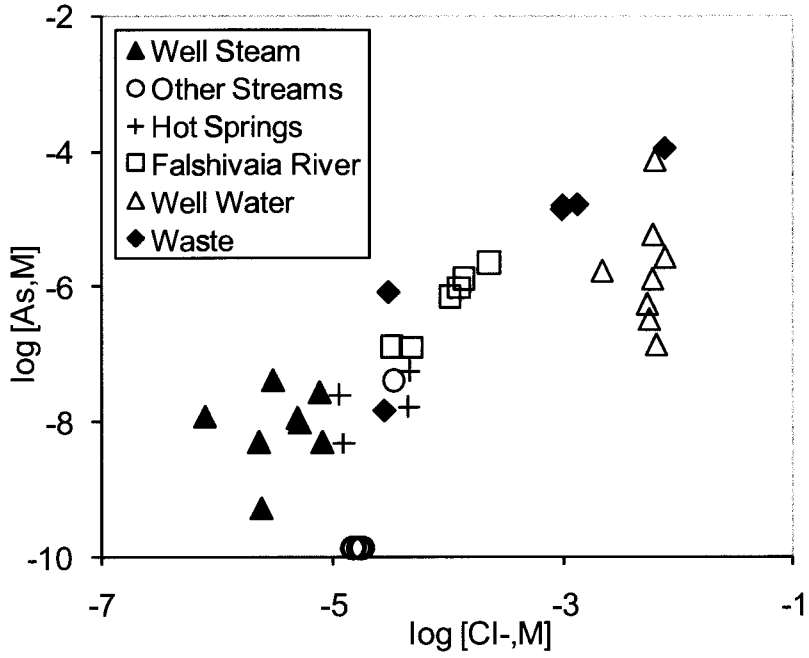


Figure 2.7 Correlation between As and $Cl^-$ in the different water types

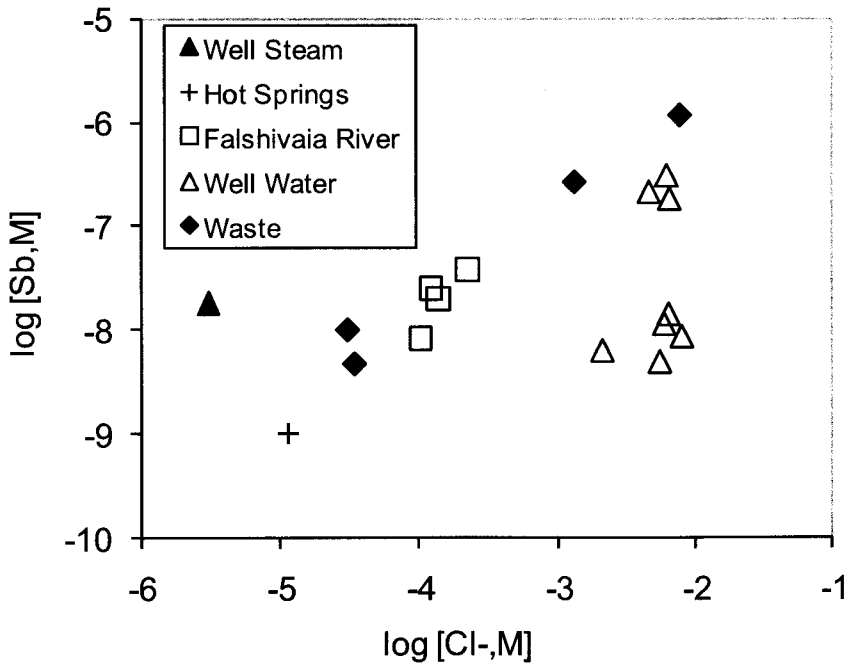


Figure 2.8 Correlation between Sb and $Cl^-$ in the different water types

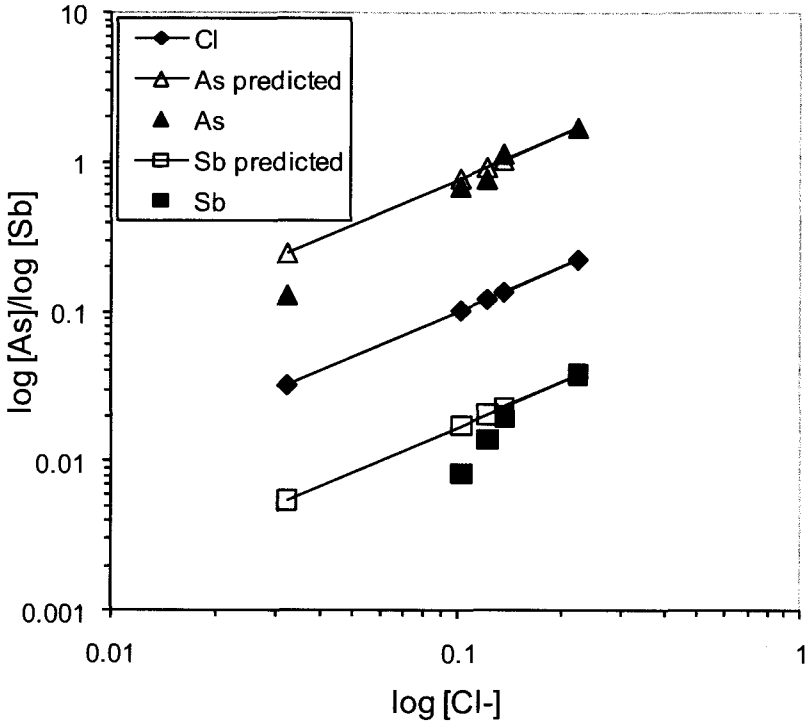


Figure 2.9 Sb and As dilution with respect to $Cl^-$ in the Falshivaia River water

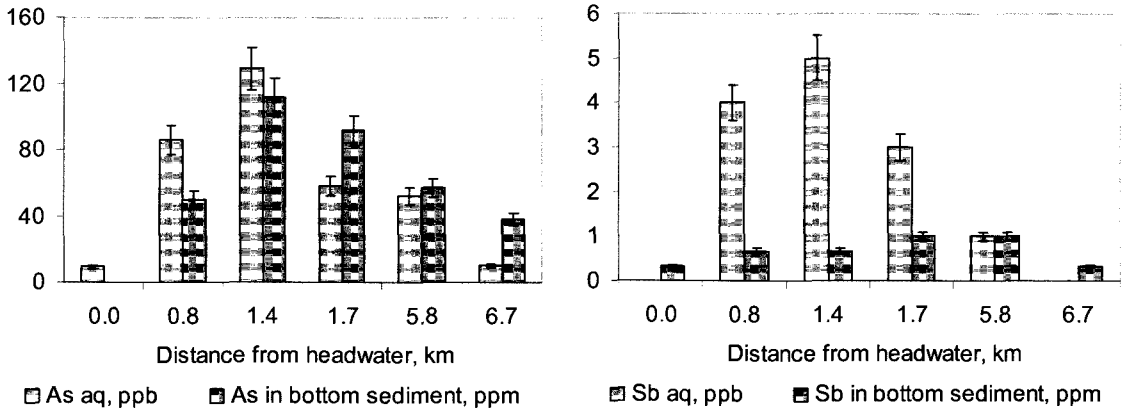


Figure 2.10 The downstream profile of As and Sb in water and bottom sediment of the Falshivaia River

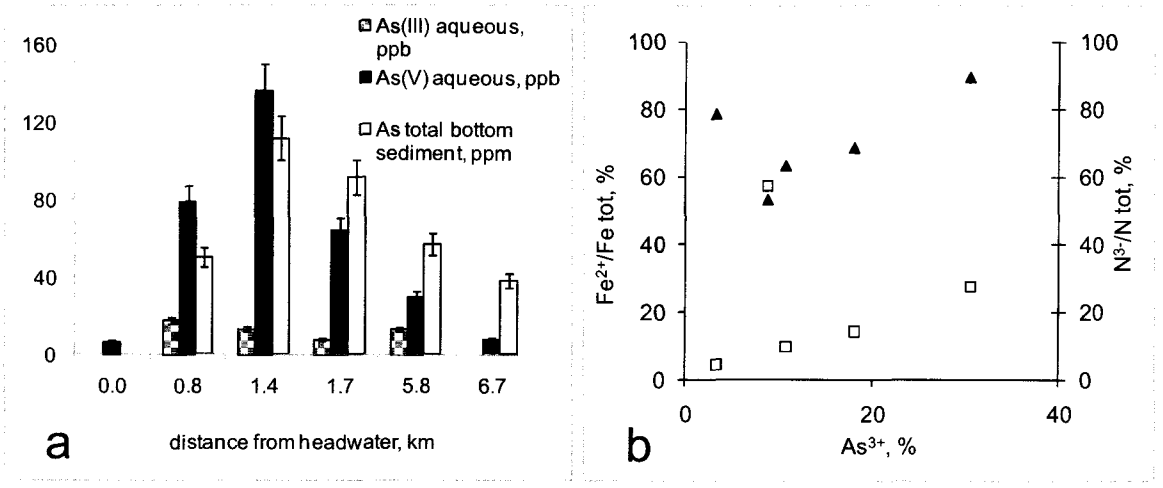


Figure 2.11 (a) Arsenic oxidation state in water and bottom sediments in the Falshivaia River; (b) Correlation between reduced As, Fe and N species

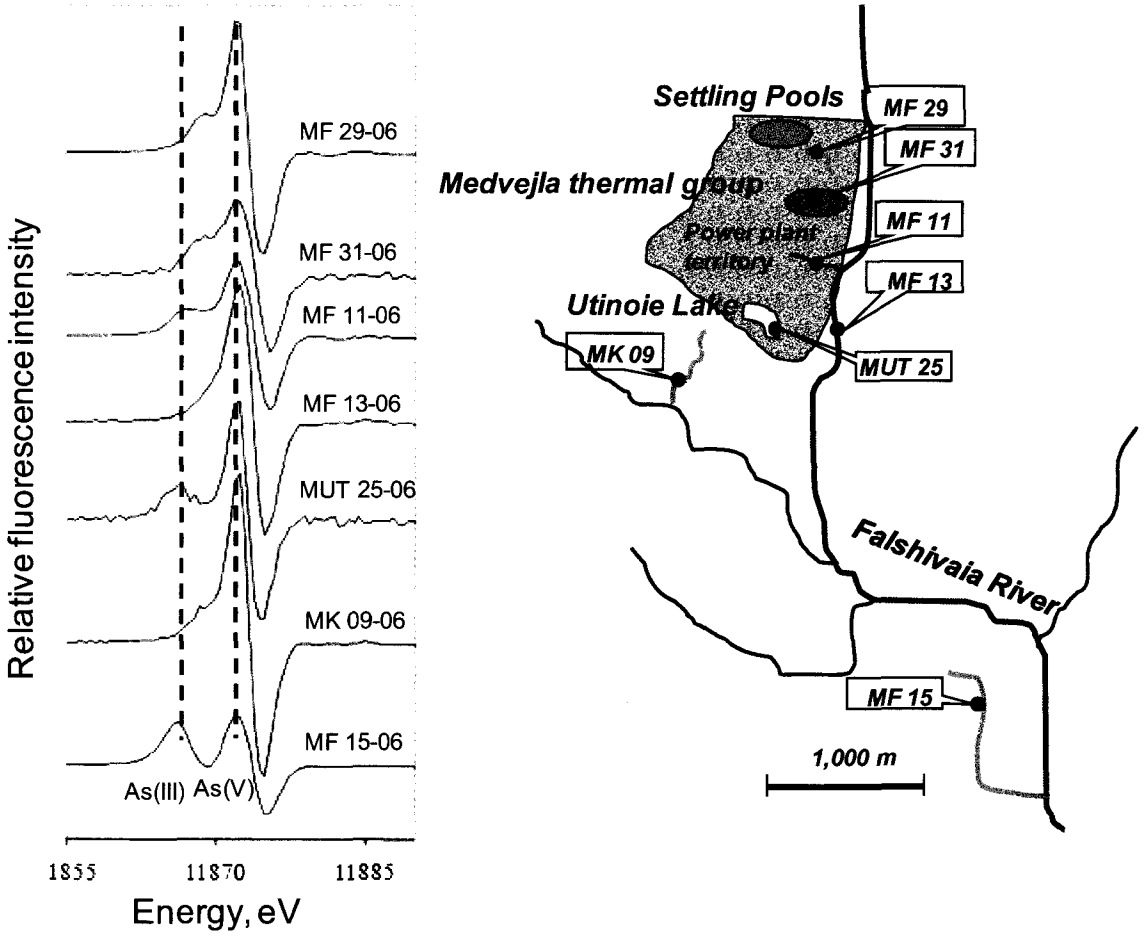


Figure 2.12 Locations of sediment samples and corresponding XANES data

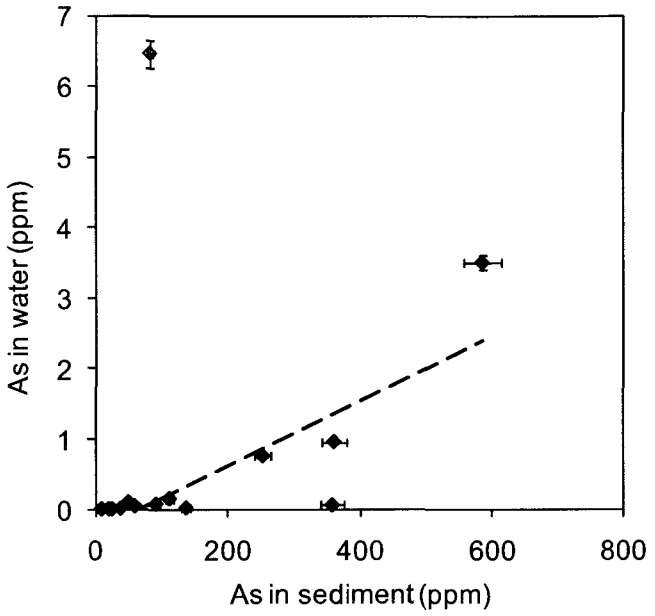


Figure 2.13 Correlation between the total As content in water and sediment samples

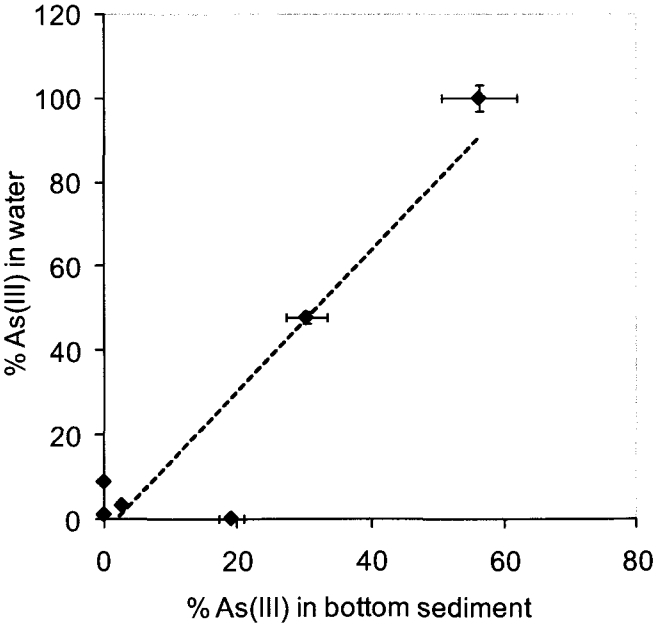


Figure 2.14 Correlation between As(III) content in sediment and aqueous samples

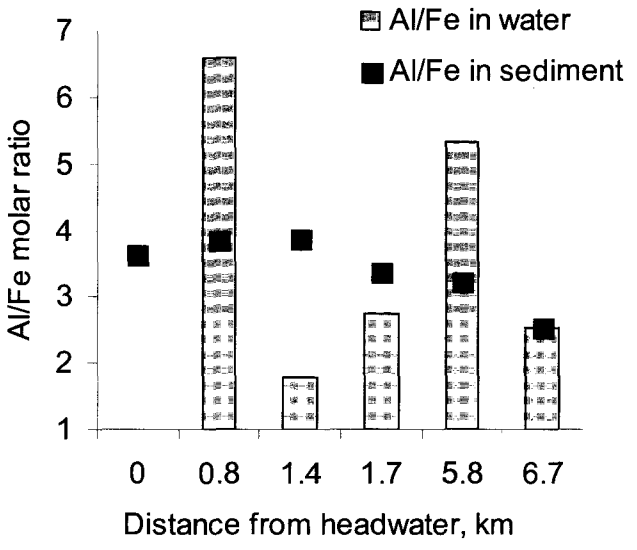


Figure 2.15 Al/Fe ratio decreases downstream from the power plant

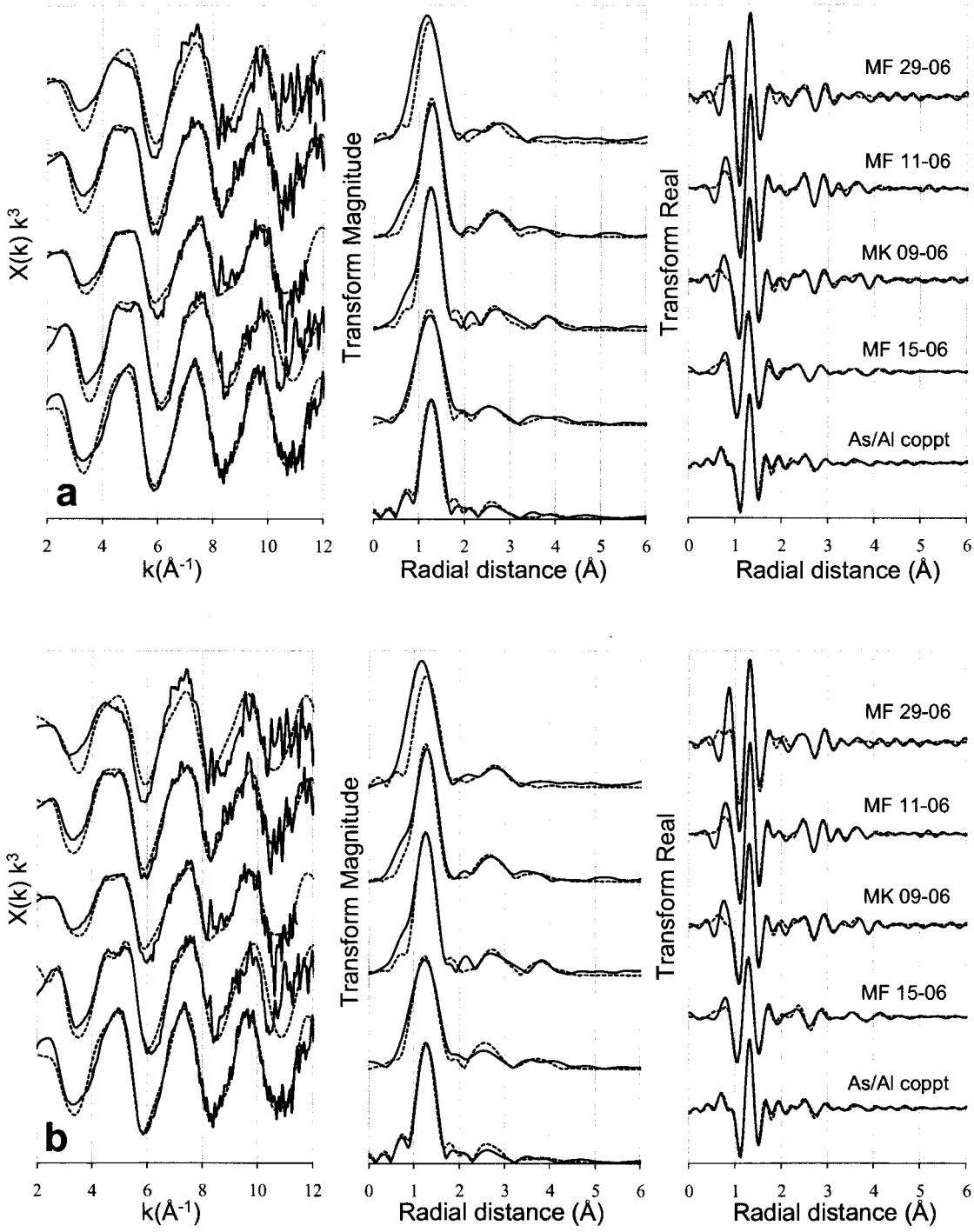


Figure 2.16 (a) EXAFS data (solid lines) and fits (dashed lines) of the field samples and Al-As co-precipitate sample based on the esperanzaite structural model; (b) EXAFS data (solid lines) and fits (dashed lines) of the field samples and Al-As co-precipitate sample based on the scorodite structural model

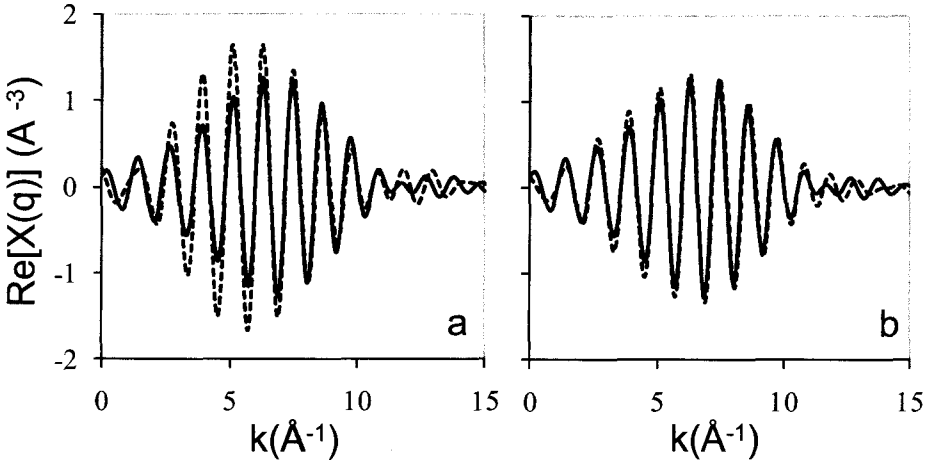


Figure 2.17 Fitting isolated 2nd shell of the Al-As co-precipitate sample with a) As-Fe or b) As-Al SS paths. MS paths are constrained

# Chapter 3: Role of Structural Fe in Nontronite NAu-1 and Dissolved $Fe^{2+}$ in Redox Transformations of Arsenic and Antimony[1]


## Abstract

Oxidation state is a major factor affecting the mobility of arsenic (As) and antimony (Sb) in soil and aquatic systems. Metal-oxide and clay minerals are effective sorbents, and some of these substrates may also promote redox reactions on their surfaces via direct or indirect facilitation of electron transfer. Iron, which substitutes for Al in the octahedral lattice sites in clays, has the potential to be in variable oxidation states. In soil clays, cycling between $Fe^{2+}/Fe^{3+}$ is a common process. This experimental work was conducted to determine whether structural Fe in clays can affect the oxidation state of As and Sb adsorbed at the clay surface and possibly cause their re-mobilization, and also to compare reactivity of structural $Fe^{2+}$ to $Fe^{2+}$ present in dissolved/adsorbed forms.

The experimental systems included batch reactors with various concentrations of $As^{3+}$, $Sb^{3+}$, $As^{5+}$, or $Sb^{5+}$ equilibrated with substrate suspensions including oxidized or reduced nontronite (NAu-1), hydrous aluminum oxide (HAO) or kaolinite (KGa-1b) under aerobic or anaerobic conditions. The reaction times ranged from 0.5 to 720 hours, and pH was constrained at either 5.5 or 8.0. The oxidation state of As and Sb in the liquid phase was determined by Liquid Chromatography in line with an Inductively Coupled Plasma Mass Spectrometer (LC-ICP-MS), and in the adsorbed form by X-ray Absorption Spectroscopy (XAS). Structural $Fe^{2+}$ was not able to reduce $As^{5+}/Sb^{5+}$ under the given conditions, while reduction was seen when aqueous $Fe^{2+}$ was present in the systems. The ability of the structural Fe in nonronite clay NAu-1 to promote oxidation of $As^{3+}/Sb^{3+}$ was greatly affected by its oxidation state: if all structural Fe was in oxidized $Fe^{3+}$ form, no oxidation was observed; however, when ~ 20 % of structural Fe was reduced to $Fe^{2+}$, this clay promoted the most extensive oxidation under both aerobic and


[1] Ilgen A.G., Foster A.L, and Trainor T.P. 2010 Role of structural Fe in nontronite NAu-1 and dissolved $Fe^{2+}$ in redox transformations of arsenic and antimony. Prepared for submission in Geochimica et Cosmochimica Acta

anaerobic conditions. Electron balance considerations suggest that structural $Fe^{3+}$ in the reduced NAu-1 was the sole oxidant in the anaerobic setup, while dissolved $O_2$ also contributes in aerobic conditions. Long-term batch experiments revealed the complex dynamics of As aqueous speciation in anaerobic and aerobic systems where reduced arsenic ($As^{3+}$) was initially added: the initial fast disappearance of $As^{3+}$ due to oxidation to $As^{5+}$, followed by a slow increase of aqueous $As^{3+}$. This behavior is explained by two simultaneous reactions: fast oxidation of $As^{3+}$ by structural $Fe^{3+}$ (anaerobic) or $Fe^{3+}$ and dissolved $O_2$ (aerobic) and the slow reduction of $As^{5+}$ by dissolved $Fe^{2+}$. These reactions are likely to take place in a natural soil or aquifer environment with seasonal cycling or slightly reducing conditions with an abundance of clay minerals and dissolved $Fe^{2+}$. The re-mobilization of As due to $As^{5+}$ reduction by aqueous $Fe^{2+}$ is likely to happen in aquifers with the residence time of water about one month.

### 3.1 Introduction

One of the major factors affecting water quality around the world is elevated concentrations of toxic elements. In particular, arsenic (As) and antimony (Sb) pose serious concern at even very low levels. The potential for water contamination with As exists across the globe. The environmental behaviour of As has received a great deal of attention in recent decades, following the revelation of the massive arsenic-related health problems in large parts of Asia (Ahuja, 2008; Henke et al., 2009; O'Day, 2005; Ravenscroft et al., 2009; Smedley and Kinniburgh, 2002). The discovery of serious long term health effects caused by drinking water with a relatively low concentration of As raises concerns in other areas, including the U.S. and Europe (Ryker, 2003; Vaughan, 2006).

Human exposure to As and Sb most commonly occurs through contaminated drinking water and, less commonly, through ingesting contaminated food and the inhalation of dust (As and Sb oxides) from burning coal and metal smelters (Frankenberger, 2002). Long term consumption of arsenic-contaminated water causes skin cancer and increases the risk of developing bladder, lung, kidney, liver, and other

types of cancer (Vaughan, 2006). Antimony and arsenic share similar toxicological properties; for example, they both act as clastogens (cause chromosomal breaks) but do not have mutagenic properties in the trivalent oxidation state (Gebel, 1997). Antimony is considered a possible human carcinogen, whereas arsenic is a known carcinogen (Gebel, 1997). Due to the high toxicity of As and Sb compounds, they are included in the USEPA priority pollutants list. Safe drinking water concentrations are limited to 6 ppb for Sb and 10 ppb for As.

The major sources of As and Sb in natural water are mineral weathering, volcanic activity, and anthropogenic sources. Arsenic is included in pesticides and often found in conjunction with gold deposits and released by gold mining (Craw et al., 2000). With the declining use of As containing pesticides, the natural mobilization of As becomes a more significant threat to water quality than As from industrial sources (Smedley and Kinniburgh, 2002). Antimony leaching is associated with mineral weathering, geothermal systems, and industrial wastes and mining (Filella et al., 2002a); Pb-Sb alloys are used in ammunition and, as a result, shooting range soils are commonly contaminated with Sb from the weathering bullets (Scheinost et al., 2006). The worldwide production of Sb is around 140,000 tons a year, with antimony being used in flame retardants, transportation materials, batteries, fine chemicals, ceramics and glass (Filella et al., 2002a).

Arsenic and antimony belong to the same chemical group, have $s^2p^3$ outer orbital electron configuration, and both are most commonly found in +3 or +5 oxidation states in the typical surface environments. The mobility of As and Sb in a natural environment is often limited by adsorption on Fe, Al, Mn oxides, and clay minerals (Foster et al., 1998b; Stollenwerk, 2003; Violante and Pigna, 2002). The extent of partitioning depends on the oxidation state ($As^{3+}$ and $Sb^{5+}$ are presumed to be more mobile), pH, the presence of competing ions, and the nature of the sorbent surface functional groups. Some of these sorbents may facilitate redox reactions on their surfaces (Hofstetter et al., 2003; Manning and Goldberg, 1997; Oscarson et al., 1981) through catalysis or direct electron transfer. The homogeneous oxidation of $As^{3+}$ in groundwater by $O_2$ is slow, with a half-life of 4-9

days (Kim and Nriagu, 2000). Therefore, heterogeneous reactions may dominate over the slower, homogeneous oxidation of $As^{3+}$ and $Sb^{3+}$, if oxygen is the only oxidant present. The kinetics of Sb redox transformations is not well understood: in some cases $Sb^{3+}$ was found in oxidizing conditions and $Sb^{5+}$ - in reducing (Filella et al., 2002b).

The oxidation of $As^{3+}$ under aerobic conditions by ferryhydrite and goethite has been previously observed (Stollenwerk, 2003). The clay minerals kaolinite (KGa-1) and illite (IMt-2) have also been shown to enhance $As^{3+}$ oxidation (Manning and Goldberg, 1997), which was attributed, according to one study, to a small amount of Mn oxides present in these clays (Manning and Goldberg, 1997); though, according to another study, oxidation resulted from significant titanium impurities (Foster et al., 1998a). Under anaerobic conditions, $As^{3+}$ has also been shown to be oxidized by the iron oxyhydroxides goethite, lepidocrocite, and green rust (Lin and Puls, 2000); however, another study showed that $As^{3+}$ oxidation on ferryhydrite, hematite, goethite and lepidocrocite happens via the Fenton mechanism and requires the presence of dissolved $O_2$ (Ona-Nguema et al., 2005). The clay minerals kaolinite, halloysite, illite, illite/montmorillonite, and chlorite have been shown to promote the oxidation of $As^{3+}$ to $As^{5+}$ under anaerobic conditions (Lin and Puls, 2000; Lin and Puls, 2003).

The homogeneous reduction of $As^{5+}$ by $Fe^{2+}$ is relatively slow with a half-life on the order of 10 days (Bose and Sharma, 2002). The reduction of $As^{5+}$ by dissolved $Fe^{2+}$ catalyzed by muscovite and montmorillonite surfaces was observed (Charlet et al., 2002; Charlet et al., 2005). The proposed reaction mechanism included inner-sphere adsorption of $As^{5+}$ and $Fe^{2+}$ with reduction taking place at the edge surfaces of phlogopite (mica) resulting in formation of $Fe^{3+}$-oxide-As precipitates localized at the edge sites (Charlet et al., 2002).

Currently, there are few studies involving Sb mobility in soil systems (Filella et al., 2002a; Filella et al., 2002b). In laboratory systems in the absence of $O_2$ and UV light, $Sb^{3+}$ has been observed to partially oxidize in the presence of goethite (Leuz et al., 2006). Iron (II)-mediated oxidation of $Sb^{3+}$ in the presence of $O_2$ or $H_2O_2$ was also observed to occur through the Fenton mechanism (Leuz and Johnson, 2005). Natural and synthetic Fe

and Mn oxyhydroxides are capable of oxidizing $Sb^{3+}$ to $Sb^{5+}$, and the oxidation by Mn is faster (Belzile et al., 2001). In shooting range soils contaminated with Sb that originates from bullets made from Pb-Sb alloys, the predominant forms are $Sb^0$ and $Sb^{5+}$ (Scheinost et al., 2006), leading to the conclusion that the oxidation of the $Sb^{3+}$ in surface conditions is fast; however, others report finding $Sb^{3+}$ in aerobic conditions and $Sb^{5+}$ in anaerobic, which suggests slow kinetics of redox transformations (Filella et al., 2002b; Leuz and Johnson, 2005). Currently, there are no studies investigating antimony redox behavior in clay systems to the best of our knowledge. The sorption and redox reactions facilitated by clay surfaces are of particular interest due to the high abundance of clay minerals in a majority of aqueous and soil environments. The structural Fe occupying octahedral lattice sites (substituting for Al) within clay has the potential for existing in variable oxidation states ($Fe^{2+}/Fe^{3}$). In soils cycling of the structural Fe between oxidation states happens in response to changing redox conditions (Stucki, 2006). Clay minerals of the smectite group with high structural iron content are capable of reducing organic contaminants by direct electron transfer from structural $Fe^{2+}$ (Hofstetter et al., 2003). Similar mechanisms could be proposed for the reduction or oxidation of As and Sb species adsorbed to Fe-rich smectites. There is evidence for As redox transformations resulting from reactions with specific clay minerals (Lin and Puls, 2000), and these mechanisms may be applicable to Sb. The main goal of this study was to investigate the role of the structural $Fe^{2+}/Fe^{3+}$ and compare it to the reactivity of adsorbed $Fe^{2+}$ associated with clay minerals in the redox transformations of As and Sb under pertinent environmental conditions.

## 3.2 Materials and Methods

### *3.2.1 Characterization and treatment of clay substrates*

To investigate the reactivity of structural Fe in the oxidation of $As^{3+}$ and $Sb^{3+}$, the following substrates were used: synthetic hydrous aluminium oxide [$Al(OH)_3$; (HAO)] as an Fe-free substrate, source clay kaolinite KGa-1b, and special clay nontronite NAu-1 available from the Source Clays Repository of the Clay Minerals Society. Milli-Q water

with the resistivity of 18.2 MΩ·cm, 0.2 μm filtered and UV-irradiated (< 1 ppb total organic carbon) was used for preparing all solutions (Barnstead NANOpure® DIamond™). Hydrous aluminium oxide was precipitated by titrating 12.82 mM $Al(NO_3)_3 \cdot 9H_2O$ (Baker analyzed, <0.002 % Fe) with 1 M NaOH (Mallinckrodt) until the pH reached 8.9 ±0.2 (Trivedi and Axe, 1999). After the precipitation, it was centrifuged and washed once with Milli-Q $H_2O$. Nontronite clay was ground gently, suspended in Milli-Q $H_2O$ and fractionated to < 2 μm particle size by settling (McKay, 1992). In order to remove amorphous Fe-oxide impurities and to reduce the octahedral $Fe^{3+}$ to $Fe^{2+}$, the NAu-1 was reduced following the citrate-bicarbonate-dithionite procedure (Stucki et al., 1984a; Stucki et al., 1984b). The procedure was carried out in an anaerobic (95 % $N_2$ and 5 % $H_2$ mixture) glove box with palladium oxygen-scrubbing catalyst and $O_2$(g) sensor with detection limit of 1 ppm. The clay was suspended in a de-oxygenated citrate-bicarbonate buffer: 8 parts by volume of 0.3 M $Na_3C_6H_5O_7 \cdot 2H_2O$ (EMS) and 1 part of 1 M $NaHCO_3$ (EMD); 53.38 mg of $Na_2S_2O_4$ (Fisher Scientific) per each 100 mg of nontronite was added to a centrifuge tube (Nalgene, air-tight caps) with the clay suspension. After sodium dithionite was added, the centrifuge tubes were closed tightly, shaken, and taken out of the glove box. They were kept in a 70° C water bath for 30 minutes, and shaken periodically. After 30 minutes, the clay was centrifuged and the centrifuge tubes were brought back into the glove box to be decanted. The clays were then re-suspended in de-oxygenated $5x10^{-3}$ M NaCl (JT Baker), followed by centrifugation. To remove $Fe^{2+}$ bound to the surface, the clay was washed twice with a de-oxygenated 2 M NaCl solution at pH 4 (acidified with ultrapure HCl) , then once with $5x10^{-3}$ M NaCl. This procedure has been shown to reduce ~20 % of octahedral Fe in Fe-rich Garfield nontronite clay (API No. 33-a) (Stucki et al., 1984b). A portion of nontronite was re-oxidized by purging with $O_2$ for over 40 hours until the clay color changed from dark blue to the original greenish. Both kaolinite and nontronite were washed with a 1 M ammonium acetate-acetic acid buffer (pH 5) to remove possible carbonate impurities, then centrifuged and washed once with Milli-Q $H_2O$. A buffer was prepared by combining 137.1 g of ammonium acetate $C_2H_7NO_2$ (Fisher Chemical) and

60.23 ml of glacial acetic acid (EMD, HPLC grade) with Milli-Q $H_2O$ and bringing the total volume to 1 l. To saturate the ion-exchange sites with $Na^+$ both reduced and oxidized nontronite, as well as kaolinite clay suspensions were washed with 1 M NaCl 3 times, followed by washing 3 times with Milli-Q $H_2O$. Then the clays were re-suspended in a 0.01 M NaCl solution. All solutions used to treat the reduced NAu-1 clay were de-oxygenated by purging for 3 hours with $N_2$, and then kept under a vacuum for a minimum of 30 minutes. All the glassware used in all the experiments was acid washed with 2 % $HNO_3$ and soaked in Milli-Q $H_2O$ prior to use. A fraction of each clay sample was freeze-dried and analysed using the Brunauer-Emmett-Teller (BET) $N_2$ adsorption method to determine the surface area. The clay samples were out-gassed at 60 °C for 30 hours prior to the analysis. All pH measurements were done using a Thermo ORION meter with combination pH electrode (PerpHectRoss).

*3.2.2 Analysis*

The two main analytical techniques used in this study were (1) X-Ray Absorption Spectroscopy (XAS), to directly determine the speciation of arsenic and antimony adsorbed by clay surfaces, and (2) Liquid Chromatography in line with Inductively Coupled Plasma Mass Spectrometer (LC-ICP-MS), to study the liquid phase speciation and uptake of As and Sb after equilibration with clay suspensions. In order to get sufficient quality XAS data the concentration of adsorbed As and Sb should be in the order of 100 ppm, which requires clays to be equilibrated with a high As/Sb solution concentration. On the other hand, ICP-MS has a typical limit of detection in the order of 1-5 ppb, and to avoid possible errors caused by large dilutions, the experimental samples had to be prepared with a relatively low initial aqueous As/Sb concentration. Due to this logistical limitation, we used multiple experimental procedures to test the ability of the structural $Fe^{2+}/Fe^{3+}$ in clay and of adsorbed $Fe^{2+}$ to change the oxidation state of As and Sb.

*3.2.3 As and Sb XAS experiments*

Samples were prepared in the laboratory by equilibrating the substrates (HAO, KGa-1b, NAu-1 and reduced NAu-1) with $As^{3+}$, $As^{5+}$, $Sb^{3+}$ or $Sb^{5+}$ solutions. The background electrolyte in all cases was 0.01 M NaCl. The pH was adjusted to 5.5 in the beginning of each experiment, allowed to drift, and then measured at the end; drift did not exceed 1 pH unit in all cases. A summary of the experimental conditions for the samples is presented in Tables 3.1 and 3.2.

The majority of the XAS scans were done in the near edge region (X-ray Absorption Near Edge Spectroscopy [XANES]), since the main analytical purpose was to determine whether there are shifts in the oxidation states of As and Sb immobilized at the surface of a substrate. Antimony analysis requires the monochromator to be shifted to the low angle (high energy), which leads to some loss of peak resolution, so several Extended X-ray Absorption Fine Structure (EXAFS) scans for selected Sb samples we also recorded. XANES and EXAFS data was collected at sectors 13 GSECARS, and 20 BM, Advanced Photon Source (APS), of the Argonne National Laboratory in Illinois at the bending magnet beamlines equipped with a Si(111) water-cooled monochromator, and at the Stanford Synchrotron Radiation Lightsource (SSRL) at the 4-1 beamline, with a Si(220) $LN_2$-cooled monochromator. For As XAS measurements a vertical focusing mirror was used to reject higher harmonics. Due to the high energy of Sb K-edge, an uncollimated X-ray beam was used; for harmonic rejection the monochromator was detuned by ~50 %. The monochromator was calibrated for As and Sb measurements using Au (L-edge 11,919 eV) or As (K-edge 11,867 eV), or Sb (K-edge 30,491 eV) containing foils. The monochromator step size was 5 eV in the pre-edge, 0.5 eV in the XANES region and 0.05 $Å^{-1}$ in the EXAFS region. The counting time was 2 seconds per point; for low concentration samples counting time was longer at higher k (power of 2 or 3 was applied). Arsenic and antimony K-edge (11,867 eV and 30,491 eV) spectra were collected using a $LN_2$ cold stage or LHe cryostat to avoid X-ray beam-induced redox reactions. Fluorescent counts were recorded using a Canberra 16 element Ge detector. To account for possible monochromator position shifts, reference spectra were recorded

using ionization chamber counts of Au (L-edge 11,919 eV) and Sb (K-edge 30,491 eV) foils placed in line after the sample. The ionization chambers $I_0$, $I_1$ and $I_2$ were filled with $N_2$, $N_2$, and Ar gasses respectively for As measurements, while for Sb all three chambers were filled with Ar gas. Each sample was scanned multiple times to improve signal-to-noise ratio. Standards for As oxidation states were sodium meta-arsenite ($NaAsO_2$ 99.3 % JT Baker) and sodium arsenate ($Na_2HAsO_4 \cdot 7H_2O$ 101.9 % JT Baker), and for Sb – antimony trichloride $SbCl_3$ (JT Baker), or antimony oxide $Sb_2O_3$ precipitated from $SbCl_3$ and potassium pyroantimonate $KSb(OH)_6$ (EMS). The XANES scans were also performed on the stock solutions used to prepare the samples. To avoid sample oxidation during sample transport to the facility, they were mounted in teflon sample holders in a glove box, then sealed in gas-impermeable bags with an $O_2$ scrubber inside and packed in dry ice; after the bag was opened, the samples were stored in liquid nitrogen prior to data acquisition.

The EXAFS/XANES data processing was done as described elsewhere (Kelly et al., 2008) using the Athena interface (Ravel and Newville, 2005). The linear combination fitting (LCF) algorithm with $NaAsO_2$ and $Na_2HAsO_4 \cdot 7H_2O$ end members for As XANES samples was used in the interval -20 to 30 eV around the As K-edge. The Fourier transformed Sb K-edge EXAFS spectra were analyzed using the Artemis interface (Ravel and Newville, 2005) by fitting theoretical Ifeffit (Newville, 2001) calculated paths, using the structure of bahianite $Al_5Sb_3O_{14}(O,OH)_2$ (Moore and Araki, 1976) or stibiconite $Sb_3O_6(OH)$. (Dihlström and Westgren, 2004). The initial data analysis revealed an unexpected outcome: in the presence of reduced nontronite and $O_2$, $As^{3+}$ was oxidized noticeably more than in the presence of other substrates; therefore, a batch experiment was set up to study this reaction in more detail in a laboratory setting.

*3.2.4 Batch sample preparation*

The experimental setup to study the **oxidation of $As^{3+}$ by reduced nontronite** included three batch reactors: (1) $As^{3+}$ added to the oxidized nontronite suspension under ambient conditions (22 °C, $O_2$ present); (2) $As^{3+}$ added to the reduced nontronite

suspension under ambient conditions (22 °C, $O_2$ present) and (3) $As^{3+}$ added to the reduced nontronite suspension in an anaerobic glove box. A large beaker with a substrate (0.5 g of clay in 100 ml of 0.01 M NaCl background electrolyte) was spiked with stock $NaAsO_2$ solution so that the final $As^{3+}$ concentration was 8.16 μM. The pH was then adjusted to 5.5 (±0.1) in the beginning of the experiment with 0.5 M NaOH or 0.5 M HCl solutions. The 10 ml aliquots were taken after 0.5, 3, 24, 72, 216 and 720 hours. Each aliquot was filtered using 0.2 μm Whatman Nylon membrane disposable filter and preserved with 6 M ultrapure HCl (ULTREX® II) so that the final HCl content was 0.036 M. Then samples were stored at 4 °C until analysis (maximum for 50 days). The left over clay was frozen, and later digested by an addition of 10 ml of 0.5 M ultrapure HCl, left on a rotary shaker for 48 hours, then filtered through 0.2 μm Whatman Nylon membrane disposable filter. The digestion was not complete and will be discussed in the results section.

To evaluate the role of $Fe^{2+}$ species adsorbed to the clay surface, an experiment was set up to evaluate the **reduction of $As^{5+}$ in the presence of KGa-1b or NAu-1 and dissolved $Fe^{2+}$.** The experiment was conducted in an $N_2/H_2$ filled anaerobic chamber set up as described above. Three suspensions of kaolinite, oxidized and reduced nontronite (0.5 g of substrate in 100 ml of 0.01 M NaCl) were prepared. Then 0.2 ml of ~10 mM $Fe^{2+}$ solution ($FeCl_2 \cdot 4H_2O$ (Acros) dissolved in de-oxygenated Milli-Q $H_2O$ ) were added so that the resulting concentration of $Fe^{2+}$ was about 20 μM. Sodium arsenate solution was added making the initial concentration of $As^{5+}$ 23.13 uM; then, the pH was adjusted to 5.5 (±0.1). The 10 ml aliquots were taken after 0.5, 3, 24, 72, 216 and 720 hours. Each aliquot was filtered and preserved, and the left over clay was frozen and then digested as described for the previous experiment.

To compare the redox behaviour of arsenic and antimony, we also studied **$Sb^{3+}$ oxidation** in the presence of three substrates: KGa-1b, NAu-1, and reduced NAu-1. Samples were prepared in individual centrifuge tubes (polypropylene, BD Falcon). 1.5 ml of the substrate suspensions were added to each tube so that the amount of substrate was 0.042 (KGa-1b), 0.062 (NAu-1), and 0.068 g (NAu-1, reduced). The experiment

included three equilibration times: 24, 168 and 720 hours at ambient atmosphere ($O_2$ not excluded), ionic strength was 0.01 M (NaCl), and light was not excluded. To conclude whether or not dissolved $O_2$ is the primary oxidizing species, a similar experiment was performed in the anaerobic glove box set up as described above. The total volume of each sample was 12.5 ml, and pH was adjusted to 5.5 (±0.1); several duplicate samples were prepared at pH 8 (±0.1).

*3.2.5 As and Sb LC-ICP-MS analysis*

Standards for the LC-ICP-MS analysis were made by diluting the same As and Sb stock solutions used in the experiments above. The concentration range was 0-250 ppb for As and 0-300 ppb for Sb; the standards were acidified with 6 M ultrapure HCl so that the resulting HCl concentration was 0.036 M. The total concentration of As and Sb in these standards was verified by ICP MS analysis prior to LC analysis. The resulting calibration curves had an $R^2$ value of 0.9999. The mobile phase for the As LC analysis consisted of 2 mM $NaH_2PO_4$ (OmniPur), 0.2 mM NaEDTA (Fisher Scientific), pH adjusted to 6 with 1 M NaOH and 50 ppb Ge ICP MS standard solution (ULTRA Scientific) was added as an internal standard. The mobile phase for Sb oxidation state analysis had the following composition: 12 mM NaEDTA (Fisher Scientific), 2 mM phtalic acid (Aldrich) and 3 vol.% methanol (JT Baker), the resulting pH was ~ 4.5, and 50 ppb of In ICP MS standard solution (ULTRA Scientific) was added as an internal standard.

Chromatographic data was exported to the Microcal Origin 6.0 software for background subtraction and integration of peaks. Arsenic ($^{75}As$) and antimony ($^{121}Sb$) counts were normalized by the internal standard ($^{72}Ge$ or $^{115}In$) counts. A small amount of $As^{5+}$ was found in the $As^{3+}$ standards. It was below the detection limit for all the standards, except for the two most concentrated, however $As^{5+}$ did not exceed 0.5-0.6 % of the As total. The $As^{5+}$ and $Sb^{5+}$ standards were pure, no detectable $As^{3+}$ or $Sb^{3+}$ were found. Freshly prepared $Sb^{3+}$ standards had $Sb^{5+}$ present at the level of ~0.2 ppb for the

1.2 ppb Sb total (the lowest standard) and 4.7 ppb for the 302 ppb Sb total (the highest standard).

## 3.3 Results and Discussion

### *3.3.1 As redox transformations in the XANES experiment*

The summary of the experimental conditions of all the As XANES samples (including duplicates) considered in this study is presented in Table 3.2. It appears that under various conditions, structural $Fe^{2+}$ was not able to reduce $As^{5+}$ in both aerobic and anaerobic setups. On the other hand, the addition of 10 mM dissolved $Fe^{2+}$ to the systems in anaerobic conditions caused ~ 40 % reduction to $As^{3+}$ in kaolinite, ~ 10 % in nontronite, and trace amount in reduced nontronite systems, noticeble after 24 hours of reaction. This reaction was more pronounced in the presence of KGa-1b compared to both reduced and oxidized NAu-1. When the concentration of aqueous $Fe^{2+}$ was decreased to 2 mM (still twice the concentration of $As^{5+}$ added to the system) there was no evidence for reduction after 200 hours. The Ti-catalysed photooxidation of $As^{3+}$ by dissolved $O_2$ in the presence of KGa-1b was described earlier (Foster et al., 1998a). In this study, we have noticed that in the aerobic system with reduced NAu-1 and $As^{3+}$, the extent of As oxidation was close to 100 % and exceeded that in an analogous system with KGa-1b (~ 50 % oxidation); however, in the presence of oxidized NAu-1 no oxidation was observed. This implies that the oxidation of $As^{3+}$ is affected by the nature of the adsorbing substrate, and when some (~20 % in this study) of the structural Fe in notronite clay is reduced to $Fe^{2+}$, the clay promotes a much more extensive oxidation of arsenic when compared to the other studied substrates under aerobic conditions. No dependence of this reaction on light was observed. The results of LCF for the samples are also shown in Table 3.2.

### *3.3.2 As redox transformations in the low initial concentration aqueous experiments*

The uptake of As by clays in the **oxidation of $As^{3+}$** batch experiment varied as a function of time (Figure 3.1). In general the uptake was 3-12 % of As total by reduced

nontronite (corresponds to 0.002-0.007 μmoles/$m^2$), and 6-22 % by oxidized nontronite (0.003-0.010 μmoles/$m^2$). The amount of arsenic oxidized varied considerably in the three nontronite suspensions studied, indicating that the oxidation state of structural Fe has a strong impact on the speciation of aqueous As. Contrary to our original hypothesis that structural $Fe^{2+}$ may be able to reduce $As^{5+}$ to $As^{3+}$, or prevent oxidation of $As^{3+}$, reduced nontronite promoted the most complete oxidation. Close to 100 % of the added $As^{3+}$ was oxidized in the batch reactor with a reduced nontronite suspension in equilibrium with the air, and there was a significant amount of $As^{3+}$ converted to $As^{5+}$ in the batch reactor kept in the anaerobic conditions: up to 70 % after 24 hours of reaction (Figure 3.2). However, the concentration of aqueous $As^{3+}$ began to increase starting from ~24 hours and up until the termination of the experiment after 720 hours. Exvclusively oxidized form $As^{5+}$ was detected in the digested clay samples. Due to this complex behaviour, the rate of $As^{3+}$ oxidation in the studied system can not be explained with a simple kinetic model. The observed initial fast disappearance of $As^{3+}$ can not be explained exclusively by adsorption, since the increace of aqueous concentration of $As^{5+}$ correlates extremely well with the disappearence of $As^{3+}$ (Figure 3.3). This indicates that regardless of whether oxidation occurs predominantly in the aqueous phase or on the clay surfaces, the sorption/desorption reaction is not the rate limiting step.

The amount of arsenic oxidized under anaerobic conditions is significantly larger than what would be expected if dissolved $O_2$ was the primary oxidant. The maximum concentration of $O_2$ in the anaerobic chamber was 1 ppm (~$10^{-6}$ atm). Using Henrys' Law's constant value of 0.0013 $mol \cdot kg^{-1} \cdot bar^{-1}$ (Linstrom and Mallard, 2005) (or 769.2 $L \cdot atm \cdot mol^{-1}$), the expected concentration of aqueous $O_2$ should be under 1.3 nM, while the maximum concentration of oxidized arsenic reached 13.8 μM. This implies that dissolved oxygen could not be the primary oxidant in the studied system. The chemical formula of NAu-1 is $M^{+}_{1.05}[Si_{6.98}Al_{1.02}][Al_{0.29}Fe_{3.68}Mg_{0.04}]O_{20}(OH)_4$ (Keeling et al., 2000), and the amount of structural Fe in $Na^{+}$-saturated nontronite is therefore 24.18 wt.%; no $Fe^{2+}$ is originally present. Since ~20 % of the structural $Fe_{total}$ was converted to $Fe^{2+}$ by chemical reduction, the left over amount of $Fe^{3+}$ is about 19 wt.%, which

corresponds to ~$1.7 \cdot 10^{-3}$ moles of $Fe^{3+}$ in the beginning of the experiment. The total number of moles of As in the system was $21 \times 10^{-6}$. Since no other possible oxidants were present in the system, $As^{3+}$ was most likely oxidized by the structural $Fe^{3+}$ in NAu-1.

The amount of As recovered from the digested samples was 105.2-107.6 %. On the other hand, the clay was not completely dissolved by 10 % HCl and therefore the amount of Fe recovered from HCl digested samples is below the total amount of Fe. The trend over time shows that solubility of NAu-1 increased during the experiment (Figure 3.4). The concentration of the total $Fe^{2+}$ (aqueous and recovered from digested clay) normalized by the total amount of Fe stayed about the same after the first 24 hours, and then decreased over time for the rest of the experiment in all three systems, coupled to the increase of the normalized total $Fe^{3+}$ (Figure 3.5). A detectable $Fe^{2+}$ in the oxidized nontronite suspension (~0.2 ppm) in the beginning of the experiment was an artefact resulting from the initial reduction procedure. The change in the overall oxidation state of Fe and decrease in $Fe^{2+}$ aqueous concentration correlates with the change of the oxidation state of As and increasing aqueous $As^{3+}$ (Figure 3.6a); therefore, the observed re-reduction of As happens due to $e^-$ transfer between adsorbed or aqueous $As^{5+}$ and aqueous $Fe^{2+}$.

The changes in the oxidation state of arsenic in the studied systems can be explained by two simultaneous reactions - the fast oxidation of $As^{3+}$ by the structural $Fe^{3+}$, and the slow reduction of adsorbed or aqueous $As^{5+}$ by aqueous $Fe^{2+}$:

$$H_3AsO_{3\,(aq)} + Fe_2O_{3\,(structural)} \rightarrow H_3AsO_{4\,(aq)} + 2FeO_{\,(structural)} \qquad (1)$$

$$H_3AsO_{4\,(sorbed)} + 2Fe(OH)_{2\,(aq)} \rightarrow Fe_2O_{3\,(sorbed)} + H_3AsO_{3\,(aq)} + 2H_2O_{\,(l)} \qquad (2)$$

It is apparent that this system does not come to an equilibrium state when $As^{3+}/As^{5+}$ ratio would be controlled by the relative forward and backward reaction rates. The products of the slower re-reduction reaction are predominant at the end of the experiment. This indicates that one of the reactants in the oxidation reaction (1) is being

fully consumed. Since the proposed oxidant – structural $Fe^{3+}$ - is associated with clay surface, it is likely that reaction (1) stops over time due to the clay surface passivation. The proposed scenario is illustrated in Figure 3.7 and includes the following steps 1) Initial adsorption of $As^{3+}$ at the clay surface by a tri-octahedral domain containing $Fe^{2+}/Fe^{2+}/Fe^{3+}$ moiety; 2) Oxidation of adsorbed $As^{3+}$ to $As^{5+}$ by structural $Fe^{3+}$; 3) desorption of $As^{5+}$ and release of $Fe^{2+}$ from edge site of the nontronite clay; 4) homogeneous reduction of $As^{5+}$ by $Fe^{2+}$; 5) Adsorption of $As^{5+}$ by tri-octahedral domains containing two $Fe^{3+}$ sites.

Since common Fe oxides (ferrihydrite, hematite, goethite and lepidocrocite) do not oxidize $As^{3+}$ under anaerobic conditions on a time scale of 24 hours (Manning et al., 1998; Ona-Nguema et al., 2005), there is no kinetic data available for comparison. In this experiment it is likely that $Fe^{3+}$ is the oxidant, however the oxidation only happens when there is some structural $Fe^{2+}$, and, as a result, when aqueous $Fe^{2+}$ is present in the system.

### *3.3.3 Reduction of $As^{5+}$ by aqueous $Fe^{2+}$*

In this experimental setup, maximum uptake was observed after about 200 hours of equilibration; the uptake was 43 and 73 % for reduced and oxidized nontronites (0.04 and 0.06 μmoles/$m^2$), and 88 % (0.6 μmoles/$m^2$) for kaolinite. As with the re-reduction of the $As^{5+}$ suggested above, the observed reduction rate was slow, and no $As^{3+}$ was detected before 72 hours from the beginning of the experiment; however, after 720 hours the fraction of the aqueous As reduced to $As^{3+}$ reached about 60 % in kaolinite, and over 90 % in nontronite and reduced nontronite suspensions. The amount of As recovered in liquid and digested samples was 90 % in the KGa-1b system, 101 % in the oxidized and 113 % in the reduced NAu-1 systems. The amount of Fe recovered from HCl-digested samples was not constant for nontronite and reduced nontronite, and as with the previous experiment, the solubility of these clays increased over the duration of the experiment. The solubility of kaolinite KGa-1b was constant and, therefore, the amount of Fe recovered from digested kaolinite samples was constant for all samples. Again, as with

the previous experiment, the $Fe^{2+}/Fe_{tot}$ ratio decreases and $Fe^{3+}/Fe_{tot}$ increases long term, leading to the conclusion that $Fe^{2+}$ is reducing $As^{5+}$ to $As^{3+}$ (Figure 3.6b).

Due to the reduction procedure, there was some $Fe^{2+}$ present in the reduced NAu-1 suspension in the beginning of the experiment and, therefore, the actual starting concentration of $Fe^{2+}$ was higher, compared to the intended 20 μM. To account for this difference, the initial concentration of $Fe^{2+}$ was back calculated based on the analysis of aqueous and digested samples collected after 0.5-24 hours of reaction. The results indicate that in the beginning of the experiment, the concentration of $Fe^{2+}$ was 6.8 μM in the KGa-1b, 23.5 μM in the oxidized NAu-1, and 224 μM in the reduced NAu-1 suspensions. The ratio of the number of moles of $Fe^{2+}$ consumed over the number of moles of $As^{3+}$ produced over the course of the experiment is 1.7 for the KGa-1b system and falls close to the theoretical stoichiometry of the redox reaction between $As^{3+}$ and $Fe^{2+}$.

When the rates of re-reduction of As in all six arsenic experiments are compared, the increase of $As^{3+}/As^{5+}$ ratio over time appears to be similar, with the exception of 2 systems: re-reduction of $As^{5+}$ under aerobic conditions in oxidized NAu-1 system, and reduction of $As^{5+}$ by dissolved $Fe^{2+}$ in reduced NAu-1 system in an anaerobic setup (Figure 3.8). This differences can be explained by a low concentration of $As^{5+}$ available for re-reduction in the first case, and by a large excess of dissolved $Fe^{2+}$ in the second.

### *3.3.4 Sb redox transformations in the high concentration experiments*

Determination of Sb oxidation state by shift in edge position is difficult due to the high energy position of the Sb K-edge (30,491 eV for $Sb^0$). The monochromator is positioned at the lower angle with respect to the incoming white radiation based on Braggs' Law. Due to the lower monochromator resolution, it was not always possible to reliably conclude whether there were differences in the oxidation state of Sb in the samples by comparing the absorption edge positions. Both reduced $Sb^{3+}$ and oxidized $Sb^{5+}$ in aqueous systems exist as oxyanions (Filella et al., 2002b) and have different coordination with respect to oxygen atoms: $Sb^{3+}$ has a trigonal pyramidal coordination,

while $Sb^{5+}$ is octahedrally coordinated (Filella et al., 2002b; Scheinost et al., 2006); therefore, the changes in the oxidation state of Sb were determined based on the EXAFS fit results for the 1st shell coordination number (CN). The theoretical paths were calculated using the structure of bahianite $Al_5Sb_3O_{14}$ (Moore and Araki, 1976) and stibiconite $Sb_3O_6$ (Dihlström and Westgren, 2004). The amplitude reduction factor ($S_0$) was determined from fitting $KSb(OH)_6$ EXAFS spectra recorded at each analytical run and was 0.87-0.98.

The changes in CN due to the reduction of $Sb^{5+}$ by dissolved $Fe^{2+}$ and oxidation of $Sb^{3+}$ immobilized at the surface of KGa-1b, reduced and oxidized NAu-1 are summarized in Table 3.1 and shown in Figure 3.9. The results indicate that under identical experimental conditions, the extent of reduction of $Sb^{5+}$ was dependent on the nature of the sorbent present in the system. The extent of reduction was more pronounced in the presence of kaolinite KGa-1b when compared to Fe-rich nontronite NAu-1. In these systems, some reduction was seen after about 24 hours of reaction. While it appears that the nature of the substrate affects the extent of reduction (either by sorption of the reactants/products, or by oxidation of aqueous $Fe^{2+}$) it is impossible to conclude whether the observed heterogeneous reduction rate is significantly different from the homogeneous rate due to the lack of data in the literature on the homogeneous reduction of $Sb^{5+}$ by $Fe^{2+}$. Since nontronite NAu-1 has higher surface area compared to kaolinite KGa-1b (85 vs.11 $m^2/g$), it would create more adsorption sites for $Fe^{2+}$ and therefore might impede the aqueous reduction of $Sb^{5+}$.

The ability of $Fe^{2+}$ containing mineral phases to reduce $Sb^{5+}$ to $Sb^{3+}$ is not known at this time. It was reported that $Sb^{5+}$ is reduced to $Sb^{3+}$ when adsorbed to green rust under anaerobic conditions (Mitsunobu et al., 2008a) whereas in a nearly identical study this phenomenon was not observed (Mitsunobu et al., 2008b). Some reduction of $Sb^{5+}$ to $Sb^{3+}$ associated with Fe-oxides was observed under reducing soil conditions (Mitsunobu et al., 2010). In our study there was no evidence that structural $Fe^{2+}$ in clays is capable of reducing $Sb^{5+}$, while dissolved $Fe^{2+}$ was able to do so. On the other hand, the presence of

some structural $Fe^{2+}$ in clay promoted the most complete oxidation of $Sb^{3+}$ under aerobic conditions; the extent of $Sb^{3+}$ oxidation was least pronounced in the oxidized NAu-1 system, and slightly more in the KGa-1b system. It is possible that the oxidation reaction in the KGa-1b system is similar to $As^{3+}$ oxidation (Foster et al., 1998a); however, in our study it does not appear that this reaction is affected by the presence of light.

*3.3.5 Sb redox transformation in the low concentration aqueous batch experiments*

The amount of $Sb^{5+}$ in the freshly prepared 300 ppb $Sb^{3+}$ solutions (made from $SbCl_3$ salt) acidified with HCl was under 2 % of the Sb total. However, after the standards were at a bench top for 24 hours, and then stored in the anaerobic glove box for 30 days the extent of oxidation of the 300 ppb solution reached 8 %. The concentration range for the $Sb^{3+}$ standards was 1-300 ppb and the extent of oxidation to $Sb^{5+}$ was dependent on the solution concentration (Figure 3.10). Since all the Sb samples considered in this study were preserved in a way that did not terminate the aqueous oxidation reaction the results discussed here are of qualitative nature only. Samples were prepared, acidified and stored in the same way, and analysed on the same day, therefore the differences between samples in the extent of $Sb^{3+}$ oxidation indicate whether the nature of the substrate present in the system affects this redox reaction.

The amount of antimony recovered in the HCl digested samples was lower than the amount added, and correlates negatively with the overall uptake (Figure 3.11). This effect was most pronounced for the samples equilibrated with the lowest initial $Sb^{3+}$ concentration, meaning that once adsorbed, the extent of antimony re-mobilization is limited under acidic conditions and depends on the surface coverage.

There is a difference in the degree of $Sb^{3+}$ oxidation between the studied substrate suspensions equilibrated under aerobic and anaerobic conditions. The extent of oxidation in the presence of KGa-1b was the lowest and similar under both aerobic and anaerobic conditions: $Sb^{3+}$ was the predominant form of Sb in both liquid and digested samples over the course of the experiment. In the presence of the oxidized NAu-1, the extent of $Sb^{3+}$ oxidation was more dependent on the presence of dissolved $O_2$. Under anaerobic

conditions, the $Sb^{3+}/Sb^{5+}$ ratio in this system was the same as in the KGa-1b system; however, under aerobic conditions the extent of oxidation was more pronounced. The system with reduced NAu-1 showed the highest oxidation in both aerobic and anaerobic conditions (Figure 3.12). Two possible oxidants present in the nontronite systems are dissolved $O_2$ and structural $Fe^{3+}$. The fact that the extent of $Sb^{3+}$ oxidation under anaerobic conditions in the presence of reduced NAu-1 (but not oxidized NAu-1) is larger than in the presence of KGa-1b indicates that structural $Fe^{3+}$ is a likely oxidant, but in order for this reaction to take place some $Fe^{2+}$ should be present in the clay structure. Also, the fact that $Sb^{3+}$ is more oxidized in both reduced and oxidized NAu-1 systems in an aerobic compared to an anaerobic setup indicates that $O_2$ is an oxidant as well, but its reactivity is dependant on the nature of the substrate present in the system. Several samples with $Sb^{3+}$ in KGa-1b suspension were equilibrated at pH 8. The extent of $Sb^{3+}$ oxidation in these samples was higher compared to the samples at pH 5.5 under both aerobic and anaerobic conditions. There was no $Sb^{3+}$ detected in the experiments involving reduced NAu-1 equilibrated with $Sb^{5+}$ solutions, leading to the conclusion that structural $Fe^{2+}$ is not capable of reducing $Sb^{5+}$ on a timescale of 1 month under the conditions of this experiment.

### 3.4 Summary

The experiments described here were designed to study the ability of octahedral $Fe^{3+}/Fe^{2+}$ in clay to affect the redox transformations of arsenic and antimony. Structural $Fe^{2+}$ did not reduce either $As^{5+}$ or $Sb^{5+}$; however, the reduction of some structural $Fe^{3+}$ to $Fe^{2+}$ in nontronite NAu-1 dramatically changed the reactivity of this clay. This partially reduced clay promoted the most extensive oxidation of $As^{3+}$ and $Sb^{3+}$ when compared to other substrates, including the fully oxidized NAu-1 under both aerobic and anaerobic conditions. Based on the $e^-$ balance, both structural $Fe^{3+}$ and dissolved $O_2$ are the most likely oxidants. Based on previous studies of the structural changes in reduced clays, a possible explanantion for the increased As and Sb oxidation in the presence of reduced NAu-1 is the following: Due to the structural re-arrangements from di- to tri-octahedral

geometry and resulting "holes" in unoccupied domains (Manceau et al., 2000; Stucki et al., 2002), there are more sites suitable for $e^-$ transfer. Also, the structural $Fe^{2+}$ may be acting as a catalyst when it is in the $Fe^{2+}$-O-$Fe^{3+}$ pair. The exact mechanism of this reaction cannot be deduced from this study alone.

Aqueous $Fe^{2+}$ was capable of reducing a significant amount of both $As^{5+}$ and $Sb^{5+}$; however, the kinetics of this reaction is slow and is on the order of days. Kaolinite KGa-1b promotes extensive oxidation of arsenic under aerobic conditions in the presence of light (Foster et al., 1998a). This reaction mechanism may be applicable to antimony; however, the extent of this reaction is much less pronounced when compared to arsenic.

In a natural soil environment, structural iron in clays undergoes reduction/reoxidation cycling most likely due to microbial activity (Stucki, 2006); partially reduced clays can be responsible for a variety of environmental reactions, including reactions suggested in this study. Aqueous $Fe^{2+}$ is commonly present in slightly reducing soil, river sediment, and aquifers. The reactions proposed in this study are likely to take place in a clay-rich river sediment, soil, or aquifer environments under typical slightly acidic pH conditions. Since the reduction of $As^{5+}$ by $Fe^{2+}$ has slow kinetics, the re-mobilization of As due to this reduction can take place in aquifers with a relatively slow water flow with a residence time of water on a time scale of one month.

**Acknowledgments**

The authors would like to thank the APS, Argonne National Laboratory, and the Stanford Synchrotron Radiation Lightsource (SSRL) for allocating beam time for this project, and also thank the beam scientists Dr. Matt Newville, Dr. Dale L. Brewe and Dr. Joe Rogers for their assistance with the XAS data acquisition. This graduate research progect was supported by the Inland Northwest Research Alliance (INRA) fellowship, some travel and analytical expenses we funded by the National Science Foundation (NSF) grant CHE-0431425; travel to the analytical facilities was partially covered by a University of Alaska Fairbanks College of Natural Science and Mathematics (UAF CNSM) grant, and an International Association of GeoChemistry (IAGC) student grant. Dr. Ken Severin and Karen Spaleta provided valuable assistance with the LC-ICP-MS work at the UAF Advanced Instrumental Laboratory.

## References

Ahuja, S. (Ed.), 2008. Arsenic contamination of groundwater: mechanism, analysis & remediation. John Wiley & Sons, Inc., 387 pp.

Belzile, N., Chen, Y., Wang, Z., 2001. Oxidation of antimony (III) by amorphous iron and manganese oxyhydroxides. Chemical Geology, 174(4): 379-387.

Bose, P., Sharma, A., 2002. Role of iron in controlling speciation and mobilization of arsenic in subsurface environment. Water Research, 36(19): 4916-4926.

Charlet, L., Bosbach, D., Peretyashko, T., 2002. Natural attenuation of TCE, As, Hg linked to the heterogeneous oxidation of Fe (II): an AFM study. Chemical Geology, 190(1-4): 303-319.

Charlet, L. et al., 2005. Adsorption and heterogeneous reduction of arsenic at the phyllosilicate-water interface. In: O'Day, P., Vlassopoulos, D., Meng, X., Benning, L. (Eds.), Advances in Arsenic Research: Integration of Experimental and Observational Studies and Implications for Mitigation.

Craw, D., Chappell, D., Reay, A., Walls, D., 2000. Mobilisation and attenuation of arsenic around gold mines, east Otago, New Zealand. New Zealand Journal of Geology and Geophysics, 43(3): 373-384.

Dihlström, K., Westgren, A., 2004. Über den Bau des sogenannten Antimontetroxyds und der damit isomorphen Verbindung BiTa2O6F. Zeitschrift für anorganische und allgemeine Chemie, 235(1-2): 153-160.

Filella, M., Belzile, N., Chen, Y., 2002a. Antimony in the environment: a review focused on natural waters I. Occurrence. Earth Science Reviews, 57(1-2): 125-176.

Filella, M., Belzile, N., Chen, Y., 2002b. Antimony in the environment: a review focused on natural waters II. Relevant solution chemistry. Earth Science Reviews, 59(1-4): 265-285.

Foster, A., Brown Jr, G., Parks, G., 1998a. X-ray absorption fine-structure spectroscopy study of photocatalyzed, heterogeneous As (III) oxidation on kaolin and anatase. Environmental Science & Technology, 32: 1444-1452.

Foster, A., Brown Jr, G., Tingle, T., Parks, G., 1998b. Quantitative arsenic speciation in mine tailing using X-ray absorption spectroscopy. American Mineralogist, 83(5-6): 553-568.

Frankenberger, W., 2002. Environmental chemistry of arsenic. CRC.

Gebel, T., 1997. Arsenic and antimony: comparative approach on mechanistic toxicology. Chemico-biological interactions, 107(3): 131-144.

Henke, K., Atwood, D., Blue, L., 2009. Arsenic: Environmental Chemistry, Health Threats and Waste Treatment. Wiley.

Hofstetter, T., Schwarzenbach, R., Haderlein, S., 2003. Reactivity of Fe (II) species associated with clay minerals. Environmental Science & Technology, 37(3): 519.

Keeling, J., Raven, M., Gates, W., 2000. Geology and characterization of two hydrothermal nontronites from weathered metamorphic rocks at the Uley graphite mine, South Australia. Clays and Clay Minerals, 48(5): 537.

Kelly, S., Hesterberg, D., Ravel, B., 2008. Analysis of Soils and Minerals Using X-ray Absorption Spectroscopy. In: Ulery, A., Drees, L. (Eds.), Methods of Soil Analysis: Part 5--Mineralogical Methods.

Kim, M., Nriagu, J., 2000. Oxidation of arsenite in groundwater using ozone and oxygen. Science of the Total Environment, The, 247(1): 71-79.

Leuz, A., Hug, S., Wehrli, B., Johnson, C., 2006. Iron-mediated oxidation of antimony (III) by oxygen and hydrogen peroxide compared to arsenic (III) oxidation. Environmental Science & Technology, 40(8): 2565-2571.

Leuz, A., Johnson, C., 2005. Oxidation of Sb (III) to Sb (V) by O2 and H2O2 in aqueous solutions. Geochimica et cosmochimica acta, 69(5): 1165-1172.

Lin, Z., Puls, R., 2000. Adsorption, desorption and oxidation of arsenic affected by clay minerals and aging process. Environmental geology, 39(7): 753-759.

Lin, Z., Puls, R., 2003. Potential indicators for the assessment of arsenic natural attenuation in the subsurface. Advances in Environmental Research, 7(4): 825-834.

Linstrom, P., Mallard, W., 2005. NIST Chemistry WebBook, NIST Standard Reference Database Number 69. National Institute of Standards and Technology, Gaithersburg MD, 20899.

Manceau, A. et al., 2000. Oxidation-reduction mechanism of iron in dioctahedral smectites: II. Crystal chemistry of reduced Garfield nontronite. American Mineralogist, 85(1): 153.

Manning, B., Goldberg, S., 1997. Adsorption and Stability of Arsenic (III) at the Clay Mineral- Water Interface. Environmental Science & Technology, 31(7): 2005-2011.

Manning, B.A., Fendorf, S., Goldberg, S., 1998. Surface structures and stability of arsenic(III) on geothite: Spectroscopic evidence for inner-sphere complexes. Environmental Science & Technology, 32(16): 2383-2388.

McKay, J., 1992. Clay separation; LSIS Technical memorandum #92-1. University of Western Ohio.

Mitsunobu, S., Takahashi, Y., Sakai, Y., 2008a. Abiotic reduction of antimony (V) by green rust (Fe4 (II) Fe2 (III)(OH) 12SO4· 3H2O). Chemosphere, 70(5): 942-947.

Mitsunobu, S., Takahashi, Y., Sakai, Y., Inumaru, K., 2008b. Interaction of synthetic sulfate green rust with antimony (V). Environmental Science & Technology, 43(2): 318-323.

Mitsunobu, S., Takahashi, Y., Terada, Y., 2010. μ-XANES Evidence for the Reduction of Sb (V) to Sb (III) in Soil from Sb Mine Tailing. Environmental Science & Technology: 79-90.

Moore, P.B., Araki, T., 1976. Bahianite, Al5Sb3O14(O,OH)2, a novel hexagonal close-packed oxide structure. Locality: Serra de Mangabeira, Bahia, Brazil. Neues Jahrbuch fur Mineralogie, Abhandlungen (126): 113-125.

Newville, M., 2001. IFEFFIT: interactive XAFS analysis and FEFF fitting. Journal of Synchrotron Radiation, 8(2): 322-324.

O'Day, P. (Ed.), 2005. Advances in Arsenic Research: Integration of Experimental and Observational Studies and Implications for Mitigation. American Chemical Society, Washington, DC.

Ona-Nguema, G., Morin, G., Juillot, F., Calas, G., Brown Jr, G., 2005. EXAFS analysis of arsenite adsorption onto two-line ferrihydrite, hematite, goethite, and lepidocrocite. Environmental Science & Technology, 39(23): 9147-9155.

Oscarson, D., Huang, P., Liaw, W., 1981. Role of manganese in the oxidation of arsenite by freshwater lake sediments. Clays and Clay Minerals, 29(3): 219-225.

Ravel, B., Newville, M., 2005. ATHENA, ARTEMIS, HEPHAESTUS: data analysis for X-ray absorption spectroscopy using IFEFFIT. Journal of Synchrotron Radiation, 12(4): 537-541.

Ravenscroft, P., Brammer, H., Richards, K., 2009. Arsenic Pollution: A global synthesis. Wiley-Blackwell.

Ryker, S., 2003. Arsenic in Ground Water Used for Drinking Water in the United States. In: Welch, A., Stollenwerk, K. (Eds.), Arsenic in ground water: geochemistry and occurrence. Kluwer Academic Pub.

Scheinost, A. et al., 2006. Quantitative antimony speciation in shooting-range soils by EXAFS spectroscopy. Geochimica et cosmochimica acta, 70(13): 3299-3312.

Smedley, P., Kinniburgh, D., 2002. A review of the source, behaviour and distribution of arsenic in natural waters. Applied Geochemistry, 17(5): 517-568.

Stollenwerk, K., 2003. Geochemical processes controlling transport of arsenic in groundwater: A review of adsorption. Arsenic in ground water: Geochemistry and occurrence: 67-100.

Stucki, J., 2006. Properties and behaviour of iron in clay minerals. Handbook of Clay Science: 423–475.

Stucki, J., Golden, D., Roth, C., 1984a. Effects of reduction and reoxidation of structural iron on the surface charge and dissolution of dioctahedral smectites. Clays and Clay Minerals, 32(5): 350-356.

Stucki, J., Golden, D., Roth, C., 1984b. Preparation and handling of dithionite-reduced smectite suspensions. Clays and Clay Minerals, 32(3): 191-197.

Stucki, J.W., Lee, K., Zhang, L., Larson, R.A., 2002. Effects of iron oxidation state on the surface and structural properties of smectites. Pure and Applied Chemistry, 74(11): 2145-2158.

Trivedi, P., Axe, L., 1999. A comparison of strontium sorption to hydrous aluminum, iron, and manganese oxides. Journal of colloid and interface science, 218(2): 554-563.

Vaughan, D.J., 2006. Arsenic. Elements, 2(2): 71-75.

Violante, A., Pigna, M., 2002. Competitive sorption of arsenate and phosphate on different clay minerals and soils. Soil Science Society of America Journal, 66(6): 1788.

Table 3.1. Experimental conditions for antimony XAS (high concentration) samples. CN – coordination number of Sb based on EXAFS fitting, the error at the 95% confidence level is shown in parenthesis

| Substrate | pH (±0.5) | $Sb^{3+}$ aq mM | $Sb^{5+}$ aq mM | $Fe^{2+}$ aq mM | Rxn time hrs | Atm | UV light | XAS data collection temp, K | CN (2σ) |
|---|---|---|---|---|---|---|---|---|---|
| KGa-1b | 5.5 | - | 0.01 | - | 200 | $N_2$ | - | <16 | 6.1(6) |
| KGa-1b | 5.5 | - | 0.5 | 1 | 200 | $N_2$ | - | <16 | 5.7(4) |
| KGa-1b | 5.5 | - | 2 | 4 | 24 | $N_2$ | - | <180 | 4.4(2) |
| NAu-1 | 5.5 | - | 0.5 | 0.01 | 2 | $N_2$ | - | <16 | 6.2(2) |
| NAu-1 | 5.5 | - | 0.5 | 1 | 200 | $N_2$ | - | <16 | 6.1(4) |
| NAu-1 | 5.5 | - | 2 | 4 | 24 | $N_2$ | - | <180 | 5.8(6) |
| NAu-1-*reduced* | 5.5 | - | 2 | 4 | 24 | $N_2$ | - | <180 | 6.1(4) |
| KGa-1b | 5.5 | 0.04 | - | - | 38 | $O_2$ | + | <16 | 4.1(2) |
| KGa-1b | 5.5 | 0.04 | - | - | 38 | $O_2$ | - | <16 | 4.2(2) |
| NAu-1 | 5.5 | 0.04 | - | - | 38 | $O_2$ | + | <16 | 3.7(2) |
| NAu-1-*reduced* | 5.5 | 0.04 | - | - | 38 | $O_2$ | + | <16 | 6.0(2) |

Table 3.2. Experimental conditions for arsenic XANES samples; the background electrolyte was 0.01 M NaCl, initial pH 5.5 (±0.5); the end-members for linear combination fitting (LCF) were XANES spectra of sodium arsenite and sodium arsenate

| Substrate | $As^{3+}$ aq mM | $As^{5+}$ aq mM | $Fe^{2+}$ aq mM | Rxn time hrs | Atm | UV light | XAS data collection temp, K | LCF $As^{3+}$ (±0.1) | LCF $As^{5+}$ (±0.1) |
|---|---|---|---|---|---|---|---|---|---|
| HAO | - | 5 | - | 40 | $N_2$ | - | <250 | 0.00 | 1.00 |
| HAO | 4.5 | - | - | 40 | $N_2$ | - | <250 | 0.84 | 0.16 |
| NAu-1 | 5 | - | - | 40 | $N_2$ | - | <250 | 0.92 | 0.08 |
| NAu-1 | - | 5 | - | 40 | $N_2$ | - | <250 | 0.00 | 1.00 |
| NAu-1-*reduced* | 5 | - | - | 40 | $N_2$ | - | <250 | 0.75 | 0.25 |
| NAu-1-*reduced* | - | 5 | - | 40 | $N_2$ | - | <250 | 0.00 | 1.00 |
| NAu-1-*reduced* | - | 5 | - | 24 | $N_2$ | + | <170 | 0.00 | 1.00 |
| NAu-1 | - | 5 | - | 24 | $N_2$ | + | <170 | 0.00 | 1.00 |
| KGa-1b | - | 5 | 10 | 24 | $N_2$ | - | <170 | 0.38 | 0.62 |
| KGa-1b | - | 5 | - | 24 | $N_2$ | - | <170 | trace | 1.00 |
| NAu-1 | - | 5 | 10 | 24 | $N_2$ | - | <170 | 0.09 | 0.91 |
| NAu-1 | - | 5 | - | 24 | $N_2$ | - | <170 | 0.00 | 1.00 |
| NAu-1-*reduced* | - | 5 | 10 | 24 | $N_2$ | - | <170 | trace | 0.96 |
| NAu-1-*reduced* | - | 5 | - | 24 | $N_2$ | - | <170 | 0.00 | 1.00 |
| NAu-1 | 0.5 | - | - | 48 | $N_2$ | + | <10 | 0.93 | 0.07 |
| NAu-1-*reduced* | 0.5 | - | - | 48 | $N_2$ | + | <10 | 0.86 | 0.14 |
| HAO | - | 1 | 2 | 48 | $N_2$ | + | <10 | 0.00 | 1.00 |
| KGa-1b | - | 1 | 2 | 2 | $N_2$ | + | <10 | 0.00 | 1.00 |
| KGa-1b | - | 1 | 0.01 | 2 | $N_2$ | + | <10 | 0.00 | 1.00 |
| KGa-1b | - | 1 | 2 | 20 | $N_2$ | + | <10 | 0.00 | 1.00 |
| KGa-1b | - | 1 | 0.01 | 20 | $N_2$ | + | <10 | 0.00 | 1.00 |
| KGa-1b | - | 1 | 2 | 200 | $N_2$ | + | <10 | 0.00 | 1.00 |
| KGa-1b | - | 1 | 0.01 | 200 | $N_2$ | + | <10 | 0.00 | 1.00 |
| NAu-1 | - | 1 | 2 | 2 | $N_2$ | + | <10 | 0.00 | 1.00 |
| NAu-1 | - | 1 | 0.01 | 2 | $N_2$ | + | <10 | 0.00 | 1.00 |
| NAu-1 | - | 1 | 2 | 20 | $N_2$ | + | <10 | 0.00 | 1.00 |
| NAu-1 | - | 1 | 0.01 | 20 | $N_2$ | + | <10 | 0.00 | 1.00 |
| NAu-1 | - | 1 | 2 | 200 | $N_2$ | + | <10 | 0.00 | 1.00 |
| NAu-1 | - | 1 | 0.01 | 200 | $N_2$ | + | <10 | 0.00 | 1.00 |
| HAO | 0.5 | - | - | 36 | $O_2$ | + | <16 | 0.85 | 0.16 |
| HAO | - | 0.5 | - | 36 | $O_2$ | + | <16 | 0.10 | 0.90 |
| NAu-1 | 0.5 | - | - | 36 | $O_2$ | + | <16 | 0.83 | 0.17 |
| NAu-1 | 0.5 | - | - | 36 | $O_2$ | - | <16 | 0.98 | trace |
| NAu-1-*reduced* | 0.5 | - | - | 36 | $O_2$ | + | <16 | trace | 0.98 |
| KGa-1b | 0.5 | - | - | 36 | $O_2$ | + | <16 | 0.51 | 0.49 |

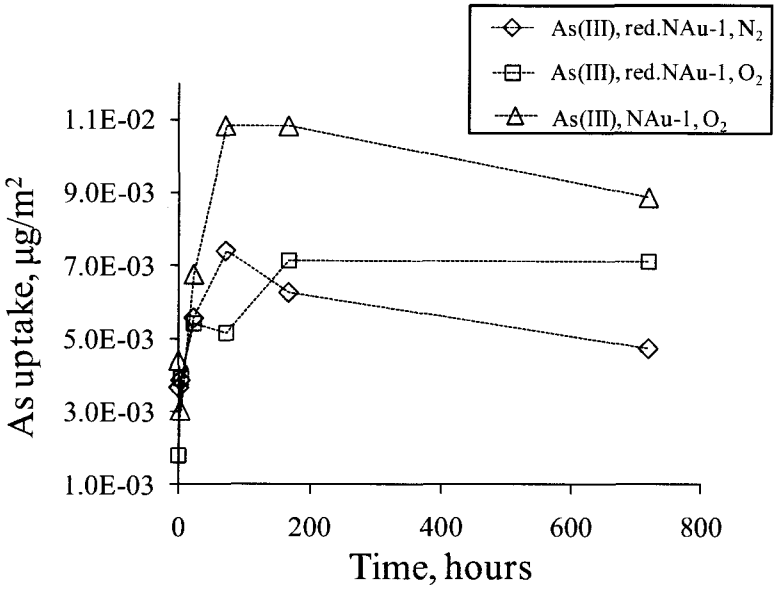


Figure 3.1. Uptake of $As^{3+}$ by oxidized and reduced nontronite in three batch studies (error bars are within the size of the data points)

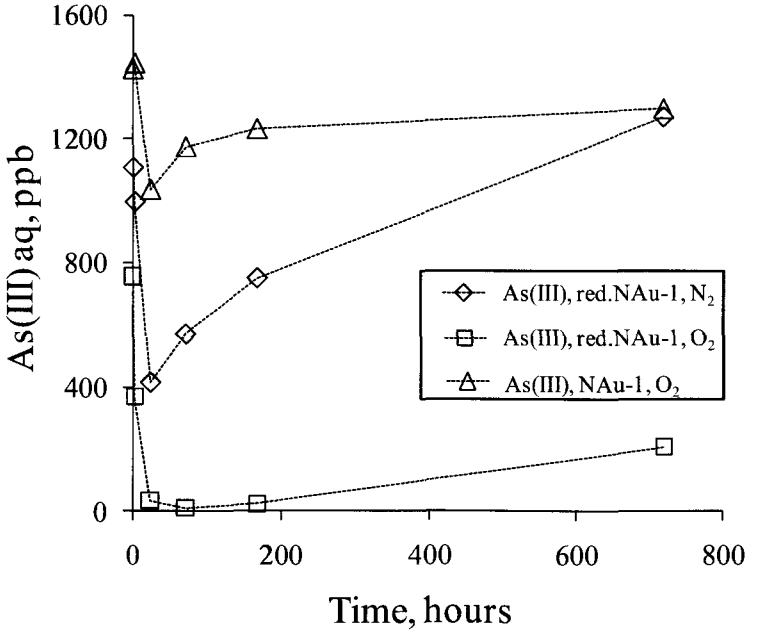


Figure 3.2. The changes of $As^{3+}$ aqueous concentrations in the studied systems (error bars are within the size of the data points)

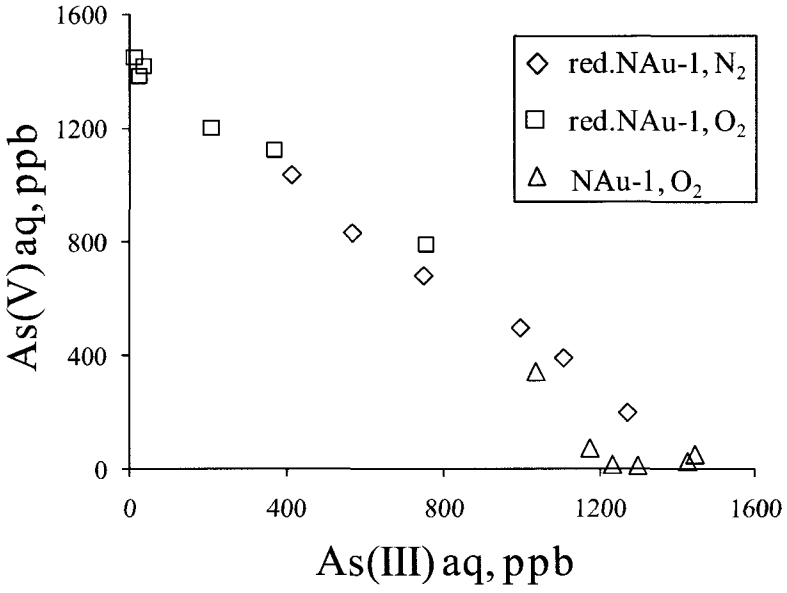


Figure 3.3. Correlation between $As^{3+}$ and $As^{5+}$ aqueous species in three nontronite suspensions

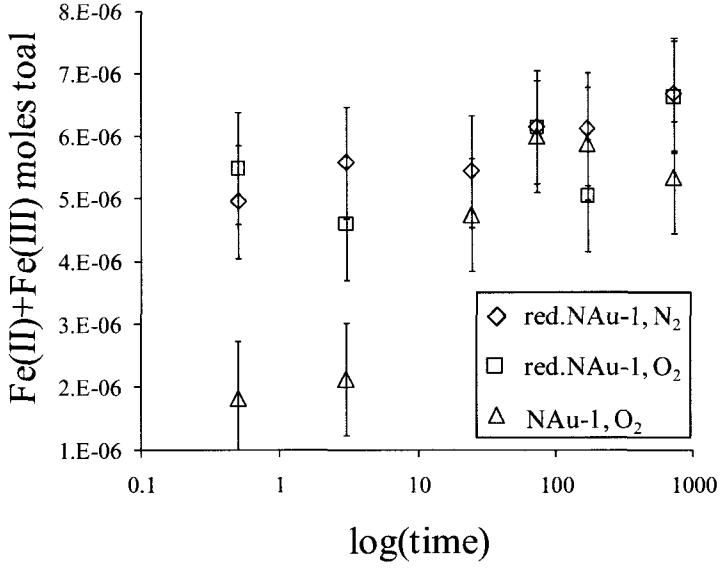


Figure 3.4. The amount of Fe recovered from digested NAu-1 samples, increasing over time, indicating increasing solubility of the substrates

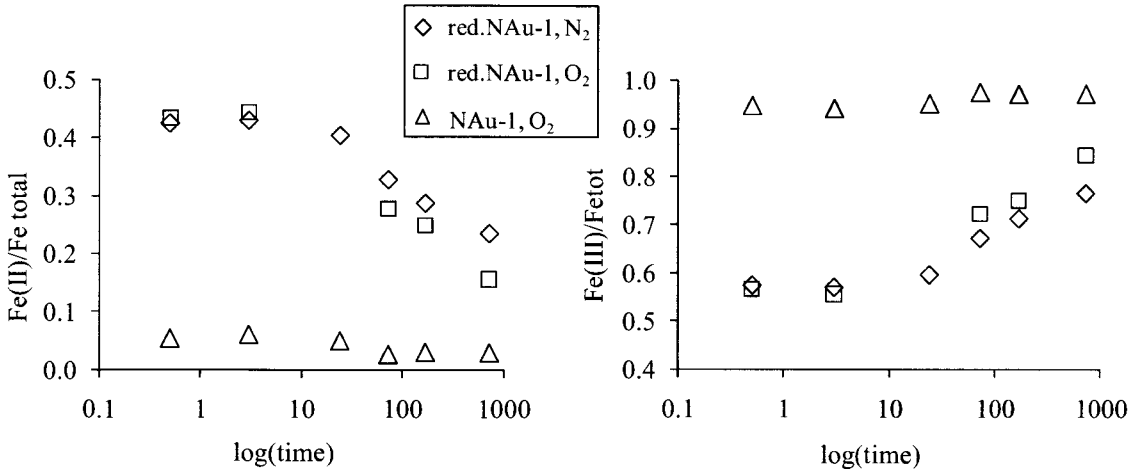


Figure 3.5. Changes in the relative amounts of reduced and oxidized Fe over the course of the experiment

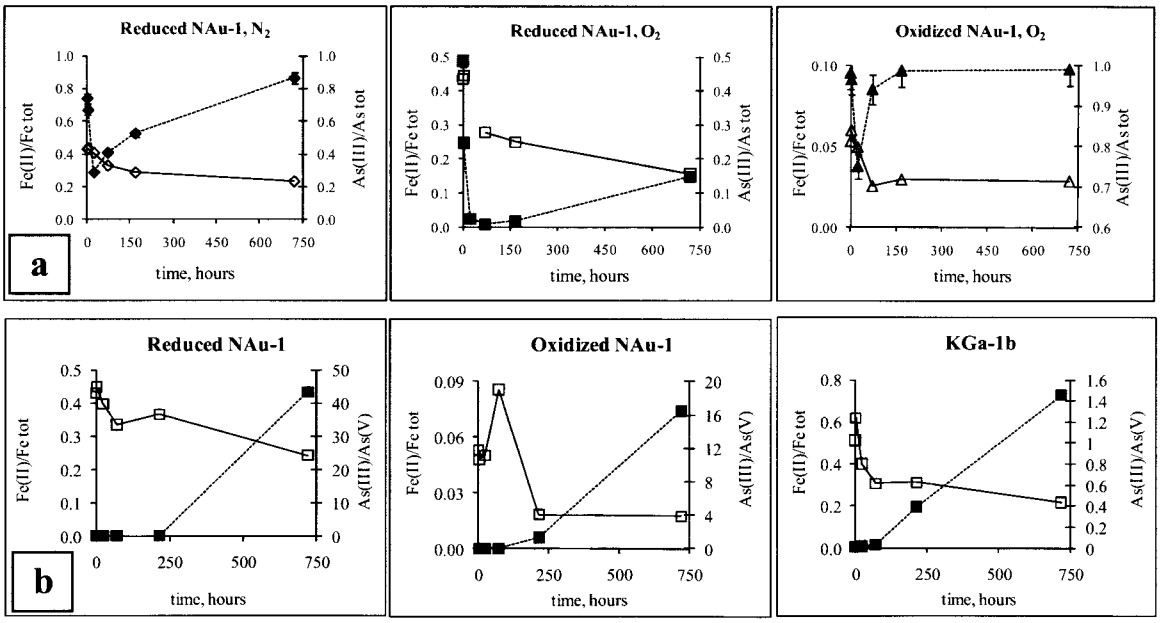


Figure 3.6. The correlation between As reduction and Fe oxidation (a) in clay systems where $As^{3+}$ was added in the beginning of the experiment, (b) in clay systems where $As^{5+}$ and $Fe^{2+}$ were added in the beginning of the experiment. Empty symbols – Fe; Solid symbols – As; error bars if not shown are within the size of the symbols

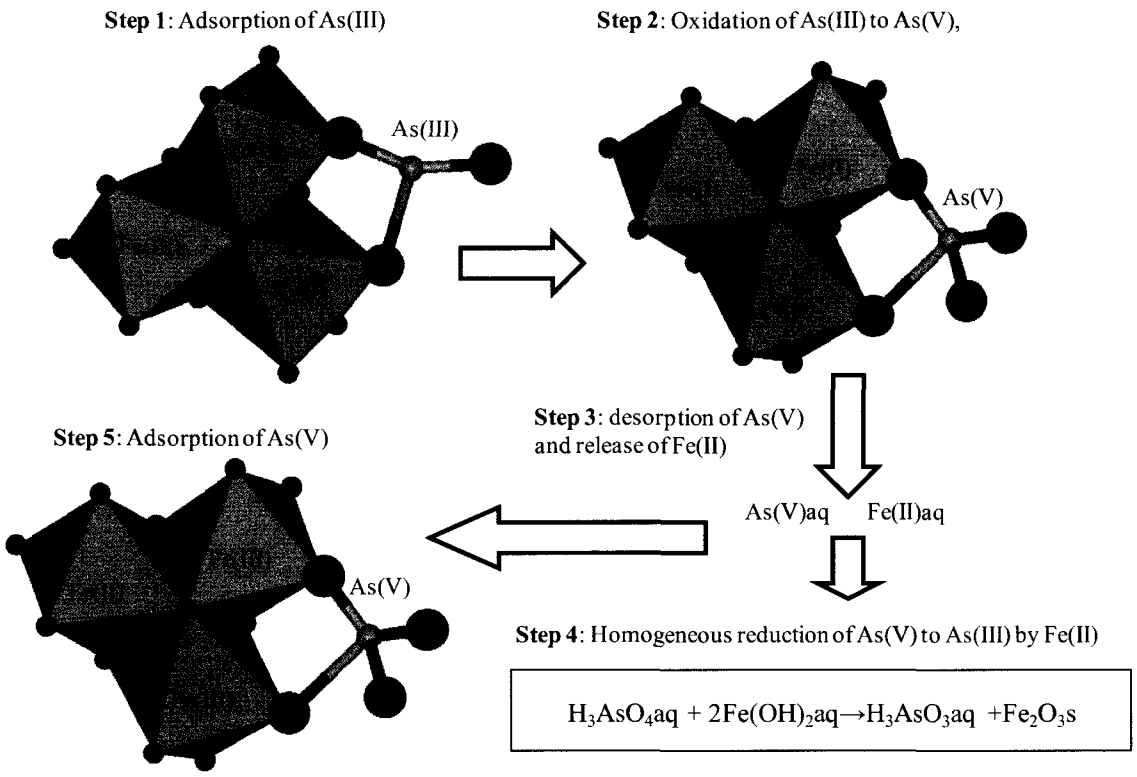


Figure 3.7 Proposed mechanism for the passivation of the nontronite clay surface

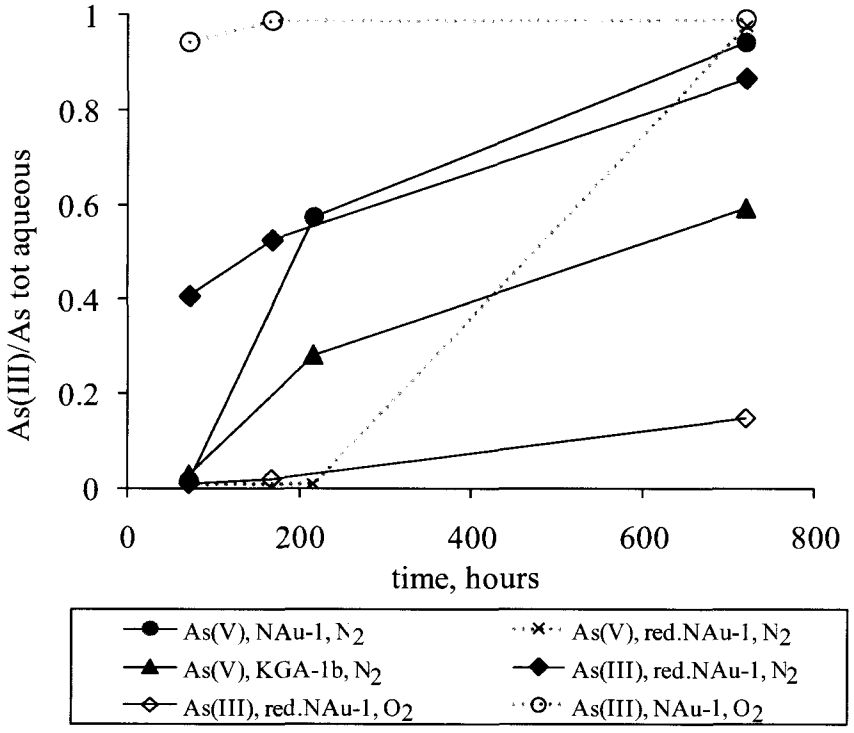


Figure 3.8. Reduction rate of $As^{5+}$ in 6 experiments

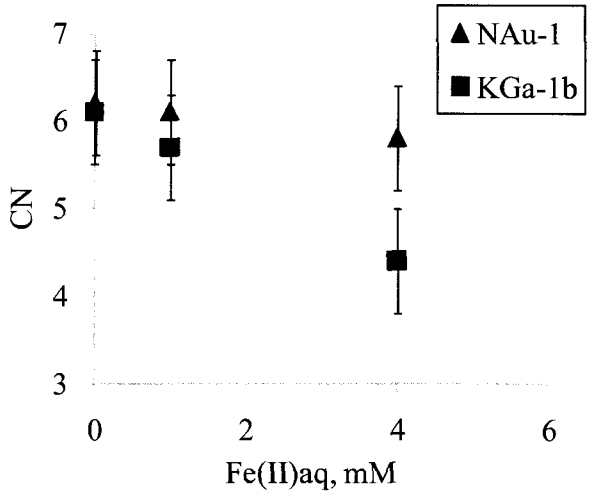


Figure 3.9. Changes in the coordination number (CN) of $Sb^{5+}$ adsorbed by kaolinite (KGa-1b) and oxidized nontronite (NAu-1), with a varying concentration of $Fe^{2+}$ in the system. The error bars in CN are ±0.6 and represent a 95% confidence level

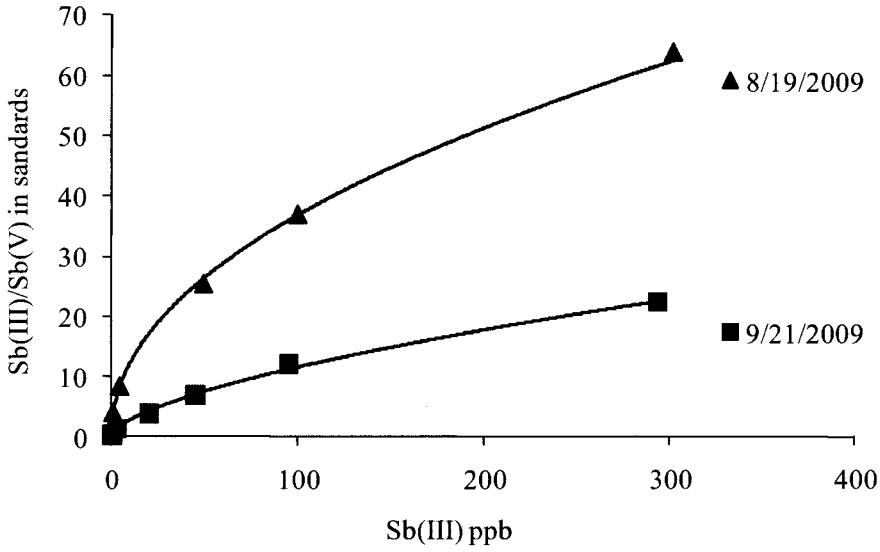


Figure 3.10. The extent of oxidation of $Sb^{3+}$ to $Sb^{5+}$ in standard solutions acidified with ultrapure HCl.

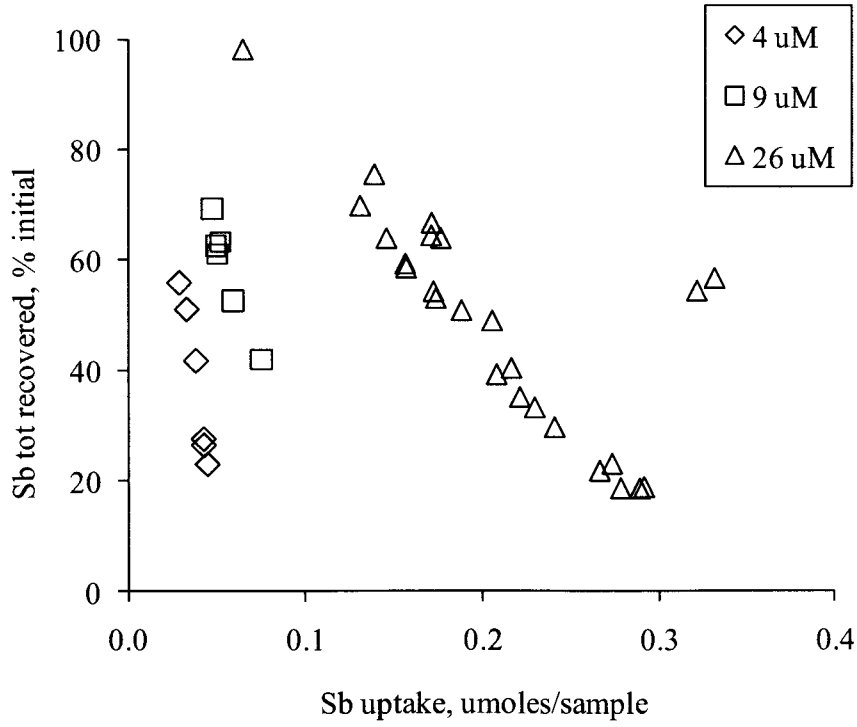


Figure 3.11. The amount of Sb recovered from digested samples was dependant on the uptake and initial concentration of $Sb^{3+}$. Substrates include KGa-1b, HAO, oxidized and reduced NAu-1.

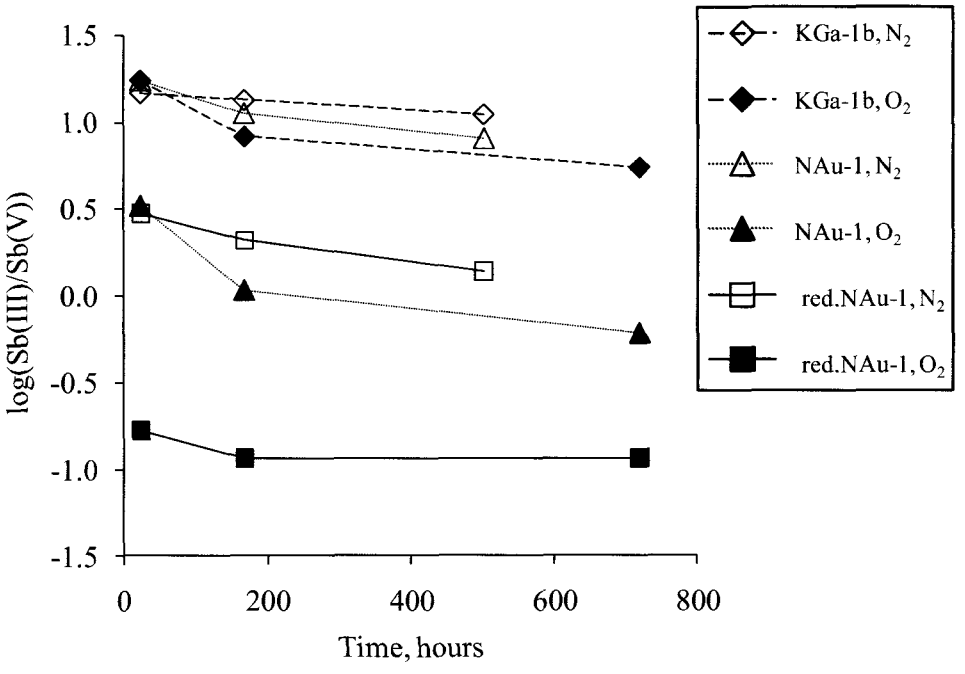


Figure 3.12. Changes in the oxidation state of Sb in the studied systems under aerobic vs. anaerobic conditions with KGa-1b, oxidized and reduced NAu-1 mineral substrates

# Chapter 4: $Sb^{3+}$ and $Sb^{5+}$ Adsorption onto Al-rich Substrates: Hydrous Al Oxide, and Clay Minerals Kaolinite KGa-1b, Oxidized and Reduced Nontronite NAu-1[1]


## Abstract

We studied the immobilization of $Sb^{3+}$ and $Sb^{5+}$ by Al-rich phases - hydrous Al oxide (HAO), the natural clay minerals kaolinite (KGa-1b), and oxidized and reduced nontronite (NAu-1) using batch experiments to determine the uptake capacity and the kinetics of adsorption, and Extended X-ray Absorption Fine Structure (EXAFS) Spectroscopy to identify the mode of adsorption and molecular environment of adsorbed Sb. Both $Sb^{3+}$ and $Sb^{5+}$ are adsorbed via an inner-sphere mode on the surfaces of the studied Al-rich substrates. The observed adsorption geometry is mostly bi-dentate corner-sharing; some mono-dentate complexes formed as well. The kinetics of adsorption is relatively slow (on the order of days), and equilibrium adsorption isotherms are best fit using the Freundlich model. The oxidation state of the clay structural Fe affects the adsorption capacity of nontronite: if the clay is reduced, the adsorption capacity towards $Sb^{3+}$ is slightly decreased, while $Sb^{5+}$ uptake is increased significantly. This may be a result of the presence of dissolved $Fe^{2+}$ in equilibrium with reduced nontronite, or associated with the structural re-arrangements in nontronite caused by reduction. These research findings indicate that Sb can be effectively immobilized by Al-rich phases; the increase in $Sb^{5+}$ uptake in response to reducing structural Fe in clay can be important in natural settings since Fe-rich clays commonly go through oxidation-reduction cycles in response to changing redox conditions.


## 4.1 Introduction

Antimony (Sb) has an average abundance of 0.5-2 μg/g in sedimentary rocks (Filella et al., 2002a), and in natural water and soil the Sb concentration is typically less than 1 μg/L (Filella et al., 2002a) and a few μg/g respectively (Filella et al., 2002a).

[1] Ilgen A.G. and Trainor T.P. 2010. $Sb^{3+}$ and $Sb^{5+}$ adsorption onto Al-rich substrates: hydrous Al oxide, and clay minerals kaolinite KGa-1b, oxidized and reduced nontronite NAu-1. Prepared for submission in the Environmental Science and Technology.

Antimony is a chalcophilic element naturally enriched in geothermal systems (Sabadell and Axtmann, 1975) and sulfide ore deposits (Filella et al., 2002a) and mined in the form of stibnite $Sb_2S_3$ (Ashley et al., 2003; Filella et al., 2002a). The world production of Sb in 2009 was 187,000 tons (Carlin Jr, 2010). It is used in flame retardants (40%), transportation materials (22%), industrial chemicals (14%), ceramics and glass (11%) (Carlin Jr, 2010); other uses include the production of semiconductors and diodes, while lead alloys with Sb are utilized in bullets (Filella et al., 2002a). Elevated concentrations of antimony are found in soils around mining and smelting sites (Wilson et al., 2010), areas affected by sewage and fertilizer use (Filella et al., 2002a), urban areas (Reimann et al., 2010), and shooting range soils (Scheinost et al., 2006). Natural waters impacted by these sources of antimony can have dissolved Sb concentrations up to 100 times above the background level (Filella et al., 2002a). Concern arises from antimony toxicity and its suspected carcinogenic properties for humans (Gebel, 1997); the United States Environmental Protection Agency maximum contaminant level for antimony in drinking water is 6 μg/L (2009).

The major pathways by which Sb can enter natural water and soil are dust deposition from smelting operations (Filella et al., 2002a), weathering of the exposed sulfide ore deposits (Ashley et al., 2003), decomposition of spent Sb-containing bullets at shooting ranges (Johnson et al., 2005) among others. The environmental behavior of Sb is not well understood at the present time (Filella et al., 2002a; Wilson et al., 2010). It appears to be relatively immobile on a large scale: areas of anthropogenic Sb enrichment tend to stay localized (Reimann et al., 2010), and elevated concentrations of Sb are generally found in the upper horizons in the soil profile (Filella et al., 2002a); however, there is experimental evidence that Sb can be mobile, especially in oxic conditions (Johnson et al., 2005; Wilson and Webster-Brown, 2009), and can be transported in soils along the preferential flow paths (Olivé, 2006). Similar to other trace metal(oid) species, Sb partitions to mineral phases and a significant amount of Sb is found in association with solid phases in soil and sediment environments (Filella et al., 2002b). Under typical surface environmental conditions Sb can exist in two oxidation states: +3 and +5, and the

extent to which Sb partitions onto mineral surfaces depends strongly on the oxidation state. The oxidized form $Sb^{5+}$ is more soluble and tends to be more mobile than $Sb^{3+}$ (Johnson et al., 2005).

Previous studies observed that reduced forms of antimony originated from weathering sulfide ore deposits (Casiot et al., 2007), oxidizing smelter residues (Wilson et al., 2004), or spent bullets (Scheinost et al., 2006) readily oxidize to $Sb^{5+}$ and partitions onto metal-oxide phases present in soil or suspended in water. In river sediments, Sb was found to be predominantly associated with Fe and Al phases (Brannon and Patrick, 1985). The mobility of $Sb^{5+}$ in soil can also be limited by the precipitation of Ca antimonate (Johnson et al., 2005).

Laboratory studies on natural sorbents showed that $Sb^{5+}$ was effectively adsorbed by soils rich in amorphous $Fe(OH)_3$ and humic acid (Tighe et al., 2005). Humic acid immobilizes $Sb^{3+}$ more effectively than $Sb^{5+}$ (Pilarski et al., 1995). The extent of $Sb^{3+}$ uptake on 110 natural soil samples showed a great variability and dependence on the presence of competing phosphate ion (Nakamaru et al., 2006). The adsorption of $Sb^{5+}$ in acidic solutions by natural river sand was also found to be dependent on the presence of other ions: EDTA, citrate, sulphite, thiosulphate, iodide, $Zr^{4+}$, tartrate and fluoride inhibited adsorption, while $Al^{3+}$ and $Pb^{2+}$ enhanced it (Hasany and Chaudhary, 1996).

Synthetic sorbents are also able to immobilize both $Sb^{5+}$ and $Sb^{3+}$. Hydrous oxides of Mn, Al and Fe were effective in removing $Sb^{3+}$ and the adsorption affinity followed the sequence $MnOOH>Al(OH)_3>FeOOH$ (Thanabalasingam and Pickering, 1990). Both $Sb^{3+}$ (Kovalenko, 1958) and $Sb^{5+}$ (Rauf et al., 1994) adsorb strongly to $MnO_2$. Antimony(III) can also be removed from solution by synthetic hydroxyapatite (Leyva et al., 2001). Synthetic goethite readily adsorbs $Sb^{3+}$ in a wide pH range, and $Sb^{5+}$ at pH <7 (Leuz et al., 2006). Due to the oxidation of $Sb^{3+}$ by $O_2$ in the goethite suspensions some desorption was also observed (Leuz et al., 2006; Watkins et al., 2006). The maximum adsorption of $Sb^{5+}$ on activated alumina was found to be in the 2.8-4.3 pH range (Xu et al., 2001) and inhibited by organic (ascorbate, EDTA, tartrate and citrate) and inorganic (arsenate, phosphate and sulfate) anions (Xu et al., 2001).

Clays can be a significant fraction of the reactive surface area in soils and river sediments, and potentially serve as a significant sink for dissolved Sb. However, as pointed out in a recent critical review (Wilson et al., 2010) information regarding antimony adsorption to naturally occurring clay minerals is lacking.

Commonly, silicate clay minerals have Fe impurities in the form of co-precipitated Fe-oxides, or structural Fe substituting for Al in the octahedral sheet of clay (Stucki, 2006). The structural Fe can be present in either +2 or +3 oxidation states; cycling between these two states commonly occurs in clay minerals in soils (Stucki, 2006). The interactions between Fe-rich clays and contaminants can be affected by the oxidation state of structural Fe (Hofstetter et al., 2006).

The main goals of this experimental work included (i) characterization of $Sb^{3+}$ and $Sb^{5+}$ adsorption onto naturally occurring Fe-poor and Fe-rich clay minerals on the macro-scale and (ii) determination of geometry of Sb adsorption complexes associated with clay minerals at a molecular level by means of X-ray Absorption Spectroscopy (XAS). We examined the effect of Sb speciation on the extent of adsorption and the effect of the structural Fe oxidation state on the uptake and resulting sorption complexes. This information is important in assessing the role that soil clay minerals may play in immobilizing antimony in the environment.

## 4.2 Experimental Section

### *4.2.1 Clay substrates*

The clay substrates we used were natural kaolinite (KGa-1b) and Fe-rich nontronite (NAu-1) supplied by the Source Clays Repository of the Clay Minerals Society. We also used synthetic hydrous aluminum oxide (HAO) as an Fe-free control substrate for XAS measurements. Milli-Q water with the resistivity of 18.2 MΩ·cm, 0.2 μm filtered and UV-irradiated (< 1 ppb total organic carbon) was used for preparing all solutions (Barnstead NANOpure® DIamond™). HAO was precipitated by titrating 12.82 mM $Al(NO_3)_3 \cdot 9H_2O$ (Baker analyzed, <0.002 % Fe) with 1 M NaOH (Mallinckrodt) until the pH reached 8.9 ±0.2 (Trivedi and Axe, 1999). After the

precipitation, it was centrifuged and washed once with Milli-Q $H_2O$. Nontronite clay was suspended in Milli-Q water and fractionated to < 2 μm particle size by settling (McKay, 1992). Fe-rich NAu-1 clay was reduced following the citrate-bicarbonate-dithionite procedure (Stucki et al., 1984a; Stucki et al., 1984b) to purify it from Fe-oxide impurities. Sodium dithionite $Na_2S_2O_4$ (Fisher Scientific) (53.38 mg per each 100 mg of NAu-1) was added to the nontronite suspended in a de-oxygenated citrate-bicarbonate buffer (8 parts by volume of 0.3 M sodium citrate $Na_3C_6H_5O_7 \cdot 2H_2O$ (EMS) and 1 part of 1 M sodium bicarbonate $NaHCO_3$ (EMD)) in an anaerobic (95 % $N_2$ and 5 % $H_2$ mixture) glove box (PLAS LABS). A palladium catalyst (PLAS LABS) was used to promote reduction of $O_2$ by $H_2$ in the glove box, where $O_2$ and $H_2$ levels were monitored by an $O_2/H_2$ sensor (COY laboratory products) with a detection limit of 1 ppm. The minimum level of $H_2$ was 2 % and $O_2$ remained below detection during the course of experiments. After sodium dithionite was added, the centrifuge tubes were kept in a 70° C water bath for 30 minutes; then the clay was centrifuged (Nalgene, air-tight caps centrifuge tubes). The clays were then re-suspended in de-oxygenated $5x10^{-3}$ M sodium chloride NaCl (JT Baker) solution, followed by centrifugation. To remove $Fe^{2+}$ bound to the surface, the clay was washed twice with 2 M NaCl solution acidified with hydrochloric acid HCl (ULTREX® II) to pH 4; then once with $5x10^{-3}$ M NaCl solution. This procedure has been shown to remove Fe-oxide impurities and to reduce ~20 % of octahedral Fe in Fe-rich Garfield nontronite clay (API No. 33-a) (Stucki et al., 1984b). A portion of nontronite was re-oxidized by purging with $O_2$ for over 40 hours until the clay color changed from dark blue to the original greenish. Both kaolinite and nontronite were washed with a 1 M ammonium acetate-acetic acid buffer at pH 5 (137.1 g of ammonium acetate $C_2H_7NO_2$ (Fisher Chemical) and 60.23 ml of glacial acetic acid $C_2H_4O_2$ (EMD, HPLC grade) diluted to 1 l with Milli-Q water) to remove possible carbonate impurities, then centrifuged and washed once with Milli-Q water. To saturate the ion-exchange sites with $Na^+$ both reduced and oxidized nontronite, as well as kaolinite clay suspensions were washed with 1 M NaCl 3 times, followed by washing 3 times with Milli-Q water. Then the clays were re-suspended in a 0.01 M NaCl solution. All solutions used to treat

the reduced NAu-1 clay were de-oxygenated by purging for 3 hours with $N_2$, and then kept under a vacuum for a minimum of 30 minutes. All the glassware used in all the experiments was acid washed with 2 % ultrapure nitric acid $HNO_3$ (ULTREX® II) and rinsed in Milli-Q water prior to use. The surface area was determined by the Brunauer-Emmett-Teller (BET) $N_2$ adsorption method. The clay samples were freeze dried and out-gassed at 60 °C for 30 hours prior to the surface area measurements.

*4.2.2 Antimony sorption isotherms*

Antimony sorption isotherms were constructed by equilibrating clays (KGa-1b, reduced and oxidized NAu-1) with various initial concentrations of potassium pyroantimonate $KSb(OH)_6$ (EMS) or antimony trichloride $SbCl_3$ (JT Baker) solutions. Due to hygroscopic properties of $SbCl_3$ and overall low solubility of $Sb^{3+}$, the $Sb^{3+}$ stock solution was prepared qualitatively by dissolving approximately 0.02 g of $SbCl_3$ in 1 liter of de-oxygenated Milli-Q water at room temperature; the solution was stirred for several hours. The 5 mM $Sb^{5+}$ stock solution was made by dissolving 0.329 g of $KSb(OH)_6$ in 250 ml of Milli-Q water. The stock solutions were filtered using 0.2 μm Whatman Nylon membrane disposable filters and Sb content was quantified by ICP-MS analysis. The $Sb^{3+}$ solution was stored in an $N_2/H_2$ glove box prior to the experiment. Clay suspensions were added to 15 ml polypropylene centrifuge tubes (BD Falcon) and diluted so that the total volume in each tube was 12.5 ml and final clay suspension density was 3.36 g/l for KGa-1b, 5.44 g/l for reduced and 4.96 g/l for oxidized NAu-1. The experiment included three equilibration times: 24, 168 and 720 hours in the ambient atmosphere ($O_2$ not excluded), the pH was adjusted in the beginning of the experiment to 5.5 (±0.1) or 8 (±0.1) with 0.5 M NaOH or 0.5 M HCl solutions, ionic strength was 0.01 M (NaCl). By the end of the experiment pH drift did not exceed 1 pH unit. A similar experiment was performed in the anaerobic $N_2/H_2$ glove box set up as described above. At the termination of adsorption, each sample was filtered using 0.2 μm Whatman Nylon membrane disposable filter and preserved with 6 M ultrapure $HNO_3$. Samples were stored at 4 °C until analysis.

*4.2.3 Antimony EXAFS experiments*

Extended X-ray Absorption Fine Structure (EXAFS) spectroscopy was used to directly determine the local bonding environment of antimony immobilized at the clay surfaces. Samples were prepared in the laboratory by equilibrating the substrates (KGa-1b, HAO, NAu-1 and reduced NAu-1) with $Sb^{3+}$ or $Sb^{5+}$ solutions. A summary of the experimental conditions for the samples considered in this study is shown in Table 4.1. The initial concentration of $Sb^{3+}$ was slightly oversaturated (saturation index ~ 0.65) with respect to homogeneous $Sb_2O_3$ phase in K-Sb-3, HAO-Sb-3 and N-Sb-3 samples, and undersaturated in RN-Sb-3 sample. The initial concentration of $Sb^{5+}$ in all samples was under the saturation limit (saturation index under -5.4) with respect to homogeneous $Sb_2O_5$ phase.

EXAFS data was collected at sectors 13 (GSECARS), and 20 (PNC/XSD) at the Advanced Photon Source (APS), Argonne National Laboratory on bending magnet lines equipped with Si(111) water-cooled monochromator. Data was also collected at the Stanford Synchrotron Radiation Lightsource (SSRL) on beamline 4-1, with a Si(220) $LN_2$-cooled monochromator. Due to the high energy of Sb K-edge (30,491 eV) an unfocused X-ray beam was used; for harmonic rejection the monochromator was detuned by ~50 %. Energy was calibrated using Sb metal foil. The monochromator step size was 5 eV in the pre-edge, 0.5 eV in the XANES region and 0.05 $Å^{-1}$ in the EXAFS region with a counting time of 2 seconds per point. For low concentration samples, counting times were scaled at higher k (power of 2 or 3 was applied). A liquid He (LHe) cryostat was used to avoid X-ray beam-induced redox reactions and to decrease thermal contribution to the Debye-Waller factors. Sample temperatures were maintained at approximately 5-15 K during the course of measurements. Fluorescent counts were recorded using a Canberra 16 element Ge detector. To account for possible monochromator position shifts, reference spectra were recorded using an ionization chamber and Sb foil placed in line after the sample. The ionization chambers were filled with Ar gas. Each sample was scanned multiple times to improve signal-to-noise ratio. Standards for Sb oxidation states were $Sb_2O_3$ precipitated from $SbCl_3$ (JT Baker) and

$KSb(OH)_6$ (EMS). Standards were scanned in transmission mode. To avoid $Sb^{3+}$ sample oxidation during sample transport to the facility, they were mounted in teflon sample holders in a glove box, then sealed in gas-impermeable bags with an $O_2$ scrubber inside and packed in dry ice; after the bag was opened, the samples were stored in liquid nitrogen prior to data acquisition.

*4.2.4 Analysis*

The total Sb content in the aqueous phase was determined using Inductively Coupled Plasma Mass Spectrometry (ICP-MS Agilent 7500ce) as described elsewhere (Creed et al., 1994). All pH measurements were done using a Thermo ORION meter with combination pH electrode (PerpHectRoss). The EXAFS data processing and fitting was done using the Athena and Artemis interface (Ravel and Newville, 2005) to the IFEFFIT (Newville, 2001) program. The background subtraction (AUTOBK algorithm (Newville et al., 1993)), normalization and conversion into *k*-space was conducted as described elsewhere (Kelly et al., 2008). To isolate individual contributions from neighboring atoms, the Fourier transform (Hanning window, *dk* value of 2) was applied over the *k*-range from 2.5 to 10.9 on average. The upper limit of the k-range was set based on the noise level in the data. The Sb K-edge EXAFS spectra were analyzed by fitting theoretical calculated single scattering (SS) paths. To calculate the theoretical phase and amplitude functions for Sb-O, Sb-Sb, Sb-Al and Sb-Fe SS paths we used the FEFF6 code (Zabinsky et al., 1995) and known structures of bahianite $Al_5Sb_3O_{14}(O,OH)_2$ (Moore and Araki, 1976), brizzite $NaSbO_3$ (Olmi and Sabelli, 1994) and tripuhyite $FeSbO_4$ (Basso et al., 2003). The data fitting was performed for k-weights of 1, 2 and 3 to make sure that the theory and data exhibit same k-dependence. For samples with high noise level the final fitting was done using the k-weight of 1; other samples were fitted using k-weights of 1, 2, and 3 simultaneously.

## 4.3 Results and Discussion

### *4.3.1 Macroscopic characterization of $Sb^{3+}$ and $Sb^{5+}$ adsorption*

The kinetics of $Sb^{3+}$ and $Sb^{5+}$ adsorption on the studied substrates is relatively slow. The uptake increased thought the course of the 720 hour experiment under oxic conditions and was between 35 and 90 % of the maximum after 24 hours depending on the substrate: reduced nontronite on average had the fastest uptake kinetics, followed by oxidized nontronite and kaolinite. Under anoxic setup 60-83 % of $Sb^{3+}$ was adsorbed within 24 hours of reaction; similarly the highest uptake was at the termination of sorption after 502 hours.

Assuming that equilibrium was reached by the termination of the adsorption experiments the uptake data was modeled with equilibrium isotherms (Kulik, 2009; Langmuir, 1916) to determine a best fit model. The linearized form of the Langmuir isotherm

$$\frac{Ceq}{\Gamma} = \frac{Ceq}{\Gamma \max} + \frac{1}{K\Gamma \max} \qquad (1)$$

where C*eq* is the equilibrium aqueous concentration ($\mu M$), $\Gamma$ and $\Gamma$max are uptake and maximum uptake ($\mu moles \times m^{-2}$), and $K_L$ ($L \times \mu mol^{-1}$) is the Langmuir equilibrium constant, and the linearized form of the Freundlich isotherm

$$\log \Gamma = \log Kf + n \log Ceq \qquad (2)$$

where $\Gamma$ is uptake ($\mu moles \times m^{-2}$), C*eq* is the equilibrium aqueous concentration ($\mu M$), *Kf* ($L \times \mu mol^{-1}$) is the Freundlich constant and *n* is a coefficient, were used to analyze the data. The Freundlich isotherm was found to give significantly better fits for all systems (Figure 4.1), except for $Sb^{5+}$ on oxidized nontronite, where the Langmuir model gave a slightly better fit. The resulting fit values are summarized in Table 4.2.

The maximum mono-layer coverage of 6.25 $sites \times nm^{-2}$ was estimated assuming that the diameter of a hydrated Sb species $Sb(OH)_6^-$ is approximately 4 Å. The maximum observed uptake of $Sb^{5+}$ on kaolinite (74.2 $\mu moles \times m^{-2}$) and on reduced nontronite (346.8 $\mu moles \times m^{-2}$) correspond to the surface coverage of 44.7 and 208.9 $sites \times nm^{-2}$ respectively, which significantly exceeds the maximum estimated mono-layer coverage.

The high surface coverage indicates that adsorption is likely coupled with substrate induced precipitation in these systems. In the oxidized nontronite suspension the maximum uptake of $Sb^{5+}$ was $8.3 \mu moles \times m^{-2}$ corresponding to $5.0\ sites \times nm^{-2}$; therefore the mono-layer coverage is not exceeded and Langmuir model appears to provide better representation of the uptake data.

The maximum observed uptake of $Sb^{3+}$ by kaolinite, nontronite, and reduced nontronite was very similar in anoxic and oxic conditions and was 20-23 $\mu moles \times m^{-2}$ on KGa-1b, about 4 $\mu moles \times m^{-2}$ on NAu-1, and 2-3 $\mu moles \times m^{-2}$ on reduced NAu-1. The estimated mono-layer coverage was exceeded only in the kaolinite system. The uptake of $Sb^{3+}$ and $Sb^{5+}$ was on the same order of magnitude for similar equilibrium aqueous concentrations in kaolinite and oxidized nontronite systems; however, the affinity of $Sb^{5+}$ for reduced nontronite was about an order of magnitude larger when compared to $Sb^{3+}$. It appears that the oxidation state of structural Fe has an evident impact on the sorption capacity of nontronite. Reduction of structural Fe caused a significant increase in affinity towards $Sb^{5+}$, and slightly decreased the affinity towards $Sb^{3+}$ compared to the oxidized nontronite. This macroscopic change in uptake can be explained by two possible processes. The first scenario is based on the fact that reduction of nontronite causes structural re-arrangements leading to the formation of tri-octahedral domains within the original di-octahedral structure (Manceau et al., 2000). Assuming that $Sb^{5+}$ is preferentially adsorbed to a site with two Fe octahedra to form a bi-dentate bi-nuclear complex, the tri-octahedral clay layer theoretically should exhibit more sites of this nature compared to a di-octahedral clay (Figure 4.2). Another possible explanation is that dissolved $Fe^{2+}$ present in equilibrium with reduced nontronite may be reducing $Sb^{5+}$ to $Sb^{3+}$ which, depending on the extent of this reaction, can cause precipitation of $Sb_2O_3$ phase. Evidence for reduction of $Sb^{5+}$ associated with $Fe^{3+}$-oxides in natural reducing soils was reported recently (Mitsunobu et al., 2010); we also found evidence for $Sb^{5+}$ reduction by aqueous $Fe^{2+}$ in laboratory settings (manuscript in preparation).

Antimony(V) shows enhanced adsorption at pH 5.5 compared to pH 8 (Figure 4.3) on kaolinite. The effect is less pronounced for $Sb^{3+}$, which correlates with the fact

that the predominant form of dissolved $Sb^{3+}$ is the $H_3SbO_3$ neutral species across this pH range.

*4.3.2 EXAFS characterization of Sb sorption complexes*

*4.3.2.1 $Sb^{3+}$ sorption complexes on HAO, KGA-1b, reduced and oxidized NAu-1*

The $k^3$ weighted and Fourier transformed EXAFS spectra of sorption samples and $Sb_2O_3$ standard and the resulting fits are shown in Figure 4.4. Surface density of $Sb^{3+}$ on all substrates was below the estimated mono-layer coverage (Table 4.1), and due to the low mass loadings have a high level of noise in the EXAFS data. Fitting for $Sb^{3+}$ samples was done using a k-weight of 1 to avoid artifacts caused by noise at higher k-values.

For all studied substrates we find that $Sb^{3+}$ forms inner-sphere sorption complexes. This analysis of the sorption complex binding modes is based on the EXAFS derived best-fit distances and identity of second nearest neighbor features, and comparing these with distances calculated from assumed geometries. In these calculations the Al-O, $Fe^{2+}$-O, and $Fe^{3+}$-O bond length are taken from the reported structure data on kaolinite $Al_2Si_2O_9H_4$ (Bish and Von Dreele, 1989), wustite $Fe_{0.99}O$ (Fjellvag et al., 2002), and nontronite $Na_{0.5}Fe_2(Si_{3.464}Al_{0.536})O_{12}H_2$ (Manceau et al., 1998), as summarized in Table 4.3. Possible inner-sphere sorption complexes and calculated antimony second neighbor inter-atomic distances are shown in Table 4.4. These values represent the approximate ranges without taking into account possible relaxations or non-ideal bond angles; therefore they are used as a guide in the following analysis and not as an exact value.

The coordination number of Sb with respect to 1$^{st}$ shell oxygen neighbor depends on the oxidation state: $Sb^{3+}$ is generally found in a trigonal pyramidal geometry with 3 O nearest-neighbors, while $Sb^{5+}$ forms an octahedron with 6 O neighbors (Scheinost et al., 2006). The $Sb^{3+}$-O bond lengths are typically in the range 1.92-2.04 Å, and $Sb^{5+}$-O is in the range 1.98-2.10 Å (Scheinost et al., 2006). The 1$^{st}$ shell coordination number for all $Sb^{3+}$ samples is close to the theoretical 3, indicating minimal to no oxidation of $Sb^{3+}$ to $Sb^{5+}$ during sample preparation, transport, and EXAFS scanning. The standard $Sb_2O_3$

was precipitated from $SbCl_3$ and, based on fitting EXAFS data, the most appropriate structural model is consistent with structure of valentinite (Whitten et al., 2004). Most notably the three characteristic Sb-Sb distances observed in the EXAFS data (Table 4.5, Figure 4.5) are within error of the reported structure.

In the HAO-Sb-3 sample, the best fit for the 2nd shell was achieved with two Sb-Al distances at 3.44(3) Å and 3.78(4) Å were combined. The 3.44(3) Å distance is likely associated with bi-dentate bi-nuclear, while the 3.78(4) Å - with mono-dentate corner sharing complexes.

In the kaolinite system (K-Sb-3), the best fit for the isolated 2nd shell was Al at 3.37(8) Å distance, indicative of bi-dentate bi-nuclear complex. No evidence for the longer (mono-dentate) distance was found in the kaolinite sample (K-Sb-3); however, due to the low scattering amplitude of Al neighbors and high noise in this sample there is a possibility that the mono-dentate backscattering is masked by noise. The best fit models for Sb immobilized on nontronite (N-Sb-3) and reduced nontronite (RN-Sb-3) surfaces also include Sb-Al distances characteristic of a bi-dentate bi-nuclear complex. In these samples there is also evidence for an additional feature at 3.7 Å (uncorrected for phase shift). This shell can be fitted with either Fe or Al or Sb at 4.20(4) Å, 4.47(9) Å and 3.97(8) Å, respectively. Since the resulting Sb-Al and Sb-Fe distances are longer than what is expected for a mono-dentate complex, and also lead to unexpectedly large phase shifts, we conclude that this feature arises due to mono-dentate Sb-O-Sb linkages. This result implies the formation of poly-nuclear Sb-complexes in association with the studied Fe-rich clay substrate. This can be explained by either existence of aqueous poly-nuclear Sb complexes adsorbing to the nontronite surface or by formation of poly-nuclear complexes on the substrate surface – possibly indicating incipient surface precipitation. The summary of resulting structural parameters and best fit values is presented in Table 4.5.

*4.3.2.2 $Sb^{5+}$ sorption complexes on HAO, KGA-1b, reduced and oxidized NAu-1*

The uptake and calculated surface coverage of $Sb^{5+}$ sorption samples are summarized in Table 4.1. The $Sb^{5+}$ uptake is below the estimated mono-layer coverage in the HAO (HAO-Sb-5) and one of the kaolinite samples (K-Sb-5-low), and exceeds it in one kaolinite (K-Sb-5-high) sample, and the oxidized (N-Sb-5) and reduced (RN-Sb-5) nontronite samples. The $k^3$ weighted and Fourier transformed EXAFS spectra of sorption samples and the $KSb(OH)_6$ standard and the resulting fits are shown in Figure 4.6. Fitting was done using k-weights of 1, 2 and 3 simultaneously to make sure that theory and observation have same k-dependence. The resulting structural parameters and best fit values are presented in Table 4.5.

The EXAFS analysis of the $KSb(OH)_6$ model compound indicates that Sb is coordinated to ~6 O atoms in the 1st shell at a distance of 1.98(1) Å. There is a 2nd shell neighbor(s) at 2.8 Å (uncorrected) distance. The best fit for the 2nd shell is ~ 1 Sb atom at 3.07(2) Å. This distance is consistent with edge sharing geometry of two Sb octahedra, similar to that in the brizzite $NaSbO_3$ (Olmi and Sabelli, 1994) structure, however, slightly shorter than edge-sharing Sb-Sb distance of 3.24 Å in the $Sb_2O_5$ structure (Jansen, 1979).

The sample with $Sb^{5+}$ adsorbed to HAO (HAO-Sb-5) has weakly expressed 2nd shell(s) due to the weak backscattering of Al atoms in addition to the likely disordered and mixed geometries of sorption complexes. A reasonable fit was achieved for a model combining 2 Sb-Al SS paths at 3.8(2) Å and 4.03(6) Å. These two distances are within the range for bi-and mono-dentate corner sharing complexes (Table 4.4).

The 2nd shell for both $Sb^{5+}$ on kaolinite samples (K-Sb-5-low and K-Sb-5-high) includes similar Sb-Al distances (3.74(2) Å and 3.67(2) Å) consistent with a bi-dentate corner sharing complex. The low surface coverage sample (K-Sb-5-low) was only fit with a single Sb-Al shell; the sample has a relatively high noise level and was fitted only using a k-weight of 1. The isolated 2nd shell of the high Sb surface coverage sample (K-Sb-5-high) can be fit with either Sb-Al or Sb-Sb SS paths. The reduced $\chi^2$ value is better when the Sb-Sb SS path is used, however, if the Sb-Al path is added to the model the

further improvement in reduced $\chi^2$ value is again statistically significant over using Sb-Sb path alone. Therefore, it appears there are 2 contributors to the 2nd shell in the high surface coverage kaolinite sample (K-Sb-5-high): Sb at 3.19(1) and Al at 3.67(2) Å. The resulting sorption model includes two types of linkages: a bi-dentate corner-sharing complex with respect to $AlO_6$ octahedral moiety, and edge-sharing complex with respect to an $SbO_6$ moiety. The short Sb-Sb distance of 3.19(1) Å is similar to the Sb-Sb distance of 3.07(2) Å observed in the model $KSb(OH)_6$ sample. These observations indicate some poly-nuclear complex formation in the high coverage sample.

The EXAFS spectra for $Sb^{5+}$ on oxidized (N-Sb-5) and reduced (RN-Sb-5) nontronite look nearly identical. In both cases the Sb-Sb backscattering is observed in the EXAFS data, which is expected based on the high surface coverage (Table 4.1). Precipitation of homogeneous $Sb_2O_5$ phase is not expected since the initial aqueous $Sb^{5+}$ concentration was significantly under the saturation limit for this phase. There are pronounced 2nd shell features at 3.1 and 3.7 Å (uncorrected) distance. The first is best fit with an Sb-Sb SS path with the corresponding distance of 3.2-3.3 Å. The isolated feature at 3.7 Å can be fit with Sb, Al, or Fe at a distance of 4.01, 4.06, and 4.26 Å, respectively. The $\chi^2$ values for fitting this isolated shell in reduced nontronite sample are 35.8 for Fe, 15.1 for Sb and 92.3 for Al. These $\chi^2$ values suggest that, at the 95 % confidence level, the Al fit is significantly worse, while Sb and Fe are similar to each other. An Sb-Fe distance of 4.26 Å however is outside the range expected for inner-sphere binding and therefore, it is more likely that this shell arises due to the presence of Sb-Sb mono-dentate corner-sharing complexes. A similar Sb-Sb distance of approximately 4.0 Å was observed in $Sb_2O_4$ oxide cervantite (Scheinost et al., 2006).

We further examined one of the Fe-rich (34.2 wt.% Fe) nontronite samples (RN-Sb-5) in order to test whether there is detectable contribution from the Sb-Fe backscattering in EXAFS data. Three plausible structural models were considered for $Sb^{5+}$ in the reduced nontronite sample (RN-Sb-5); the resulting fitting and structural parameters are listed in Table 4.5. The first and second models consider only Sb-Sb SS paths which would be consistent with poly-nuclear surface complexes/surface

precipitation and Sb-Sb backscattering dominating the overall EXAFS signal. The first model assumes 2 Sb neighbors at 3.23(6) and 4.01(7) Å respectively, while in the second model the longer distance Sb-Sb path is ignored. The resulting $\chi^2$ values suggest that model 1 is better in explaining observed EXAFS features. In the third structural model we also considered an Sb-Fe SS path. A combination of Sb-Sb at 3.28(1) Å and Sb-Fe at 3.80(8) Å gave a reasonable fit; however, the resulting $\chi^2$ value when compared to the $\chi^2$ value of the model 1 is not statistically different. It is possible that due to the much weaker backscattering ability of Fe and Al compared to Sb, their contributions are masked by Sb signature in these samples. Hence, we suggest that the data are consistent with inner-sphere sorption, but also show significant formation of poly-nuclear complexes due to the high surface loading.

Overall, the Sb-Sb backscattering was observed in $Sb^{3+}$ (N-Sb-3 and RN-Sb-3) and $Sb^{5+}$ (K-Sb-5-high, N-Sb-5, and RN-Sb-5) sorption samples which had Sb surface loading over 1 site·nm$^{-2}$.

*4.3.2.3 The identity of the 2$^{nd}$ shell neighbor*

In the clay samples described above, having chemical constraints was essential in order to determine the identity of the 2$^{nd}$ shell neighbor. In field samples it will generally be the case that there is a mixture of clays and oxides of various compositions, to which Sb may be adsorbed. There is also a possibility of poly-nuclear Sb species formation depending on the aqueous concentration. Therefore it is useful to test whether or not Al and Fe atoms (and possibly Sb) in the 2$^{nd}$ shell can be distinguished in relatively low coverage samples. We tried fitting a HAO-Sb-3 control sample (no Fe present) using a tripuhyite FEFF model that includes Sb-Fe paths; good fits with reasonable Sb-Fe distance can be achieved (Table 4.6). The $\chi^2$ value is close to the value for what we assume is a valid fit (Table 4.5), meaning that the fits with Al vs. Fe in the 2$^{nd}$ shell are statistically similar. We also tested the kaolinite sample K-Sb-5-low by fitting Fe in the second shell using 2 different k-ranges and k-weights of 1, 2, and 3. The Debye-Waller factors $\sigma^2$ were fixed at 0.005. The results are summarized in Table 4.7. When a more

narrow (2.596-9.135) k-range is used, there is no certainty on the identity of the 2nd shell scattering atom. The $\chi^2$ values which are statistically the same (or the best fit) for each k-weight are shown in bold font. For a k-weight of 1, all three models are the same; for a k-weight of 2, Sb-Fe gives the best fit, while for a k-weight of 3 Sb-Fe and Sb-Sb are the same again. When the k-range is expanded (2.596-10.888) the Sb-Al SS path becomes a better fit using k-weights of 1 and 2; however, at a k-weight of 3, Sb-Al and Sb-Fe are not statistically different. This implies that in a natural sample where both Al and Fe-rich phases are present, determining which substrate is responsible for Sb retention can be problematic.

### 4.4 Conclusions, Relevance to a Natural Environment

Our findings indicate that both $Sb^{3+}$ and $Sb^{5+}$ are adsorbed via the formation of inner-sphere complexes on the surfaces of studied Al-rich substrates. The observed adsorption geometry is mostly bi-dentate corner-sharing. In addition, on the surface of hydrous Al oxide both $Sb^{3+}$ and $Sb^{5+}$ form mono-dentate complexes as well. The Al-rich phases are therefore capable of immobilizing Sb in surface environmental conditions. These retention pathways can play an important role in a clay-rich natural environment. Furthermore, the kinetics study shows that adsorption continues over relatively long time scales (on the order of days). The maximum calculated surface coverage was exceeded for several samples; Sb-Sb backscattering feature observed in EXAFS data is interpreted as evidence for the poly-nuclear complex formation.

Based on the fitting of Sb adsorbed to pure HAO, we showed that the nature of the 2nd shell neighbor, namely distinguishing between Fe and Al in the 2nd shell, can not be done based on the EXAFS data alone. This implies that when natural samples are analyzed where both Fe and Al-rich phases are present, the identity of the adsorbing substrate can not be determined without ambiguity. The oxidation state of the clay structural Fe affects the adsorption capacity of nontronite: if clay is reduced, the adsorption capacity towards $Sb^{3+}$ is slightly decreased, while $Sb^{5+}$ uptake is dramatically increased. This is likely a result of the presence of dissolved $Fe^{2+}$ in equilibrium with

reduced nontronite. There is also a possibility that increased uptake is due to increase in the number of available sites for $Sb^{5+}$ adsorption in reduced nontronite compared to oxidized nontronite. This changing $Sb^{5+}$ uptake capacity in response to changing the oxidation state of structural Fe can be an important factor in a natural setting since Fe-rich clays commonly go through oxidation-reduction cycles in response to changing redox conditions.

**Acknowledgments**

We thank the beam scientists Dr. Matt Newville, Dr. Dale L. Brewe and Dr. Joe Rogers for their help with XAS data acquisition. Funding was provided by the National Science Foundation (NSF) grant CHE-0431425.

## References

United States Environmental Protection Agency, 2009. National Primary Drinking Water Regulations, 816-F-09-004.

Ashley, P., Craw, D., Graham, B., Chappell, D., 2003. Environmental mobility of antimony around mesothermal stibnite deposits. New South Wales, Australia and southern New Zealand. Journal of Geochemical Exploration, 77(1): 1–14.

Basso, R., Cabella, R., Lucchetti, G., Marescotti, P., Martinelli, A., 2003. Structural studies on synthetic and natural Fe-Sb-oxides of MO2 type. Neues Jahrbuch für Mineralogie - Monatshefte, 2003(9): 407-420.

Bish, D., Von Dreele, R., 1989. Rietveld refinement of non-hydrogen atomic positions in kaolinite. Clays and Clay Minerals, 37(4): 289-296.

Brannon, J., Patrick, W., 1985. Fixation and mobilization of antimony in sediments. Environmental Pollution Series B, Chemical and Physical, 9(2): 107-126.

Carlin Jr, J., 2010. Antimony, U.S. Geological Survey, Mineral Commodity Summaries. USGS.

Casiot, C., Ujevic, M., Munoz, M., Seidel, J., Elbaz-Poulichet, F., 2007. Antimony and arsenic mobility in a creek draining an antimony mine abandoned 85 years ago (upper Orb basin, France). Applied Geochemistry, 22(4): 788-798.

Creed, J., Brockhoff, C., Martin, T., 1994. EPA method 200.8, Revision 5.4 Determination of trace elements in waters and wastes by inductively coupled plasma - mass spectrometry. US Environmental Protection Agency.

Filella, M., Belzile, N., Chen, Y., 2002a. Antimony in the environment: a review focused on natural waters I. Occurrence. Earth Science Reviews, 57(1-2): 125-176.

Filella, M., Belzile, N., Chen, Y., 2002b. Antimony in the environment: a review focused on natural waters II. Relevant solution chemistry. Earth Science Reviews, 59(1-4): 265-285.

Fjellvag, H., Hauback, B., Vogt, T., Stolen, S., 2002. Monoclinic nearly stoichiometric wustite at low temperatures. American Mineralogist, 87(2-3): 347.

Gebel, T., 1997. Arsenic and antimony: comparative approach on mechanistic toxicology. Chemico-biological interactions, 107(3): 131-144.

Hasany, S., Chaudhary, M., 1996. Sorption potential of Haro river sand for the removal of antimony from acidic aqueous solution. Applied Radiation and Isotopes, 47(4): 467-471.

Hofstetter, T.B., Neumann, A., Schwarzenbach, R.P., 2006. Reduction of Nitroaromatic Compounds by Fe(II) Species Associated with Iron-Rich Smectites. Environmental Science & Technology, 40(1): 235-242.

Jansen, M., 1979. Die Kristallstruktur von Antimon (V)-Oxid. Acta Crystallographica Section B: Structural Crystallography and Crystal Chemistry, 35(3): 539-542.

Johnson, C., Moench, H., Wersin, P., Kugler, P., Wenger, C., 2005. Solubility of antimony and other elements in samples taken from shooting ranges. Journal of environmental quality, 34(1): 248.

Kelly, S., Hesterberg, D., Ravel, B., 2008. Analysis of Soils and Minerals Using X-ray Absorption Spectroscopy. In: Ulery, A., Drees, L. (Eds.), Methods of Soil Analysis: Part 5--Mineralogical Methods.

Kovalenko, P., 1958. Adsorption of trivalent antimony my manganese dioxide. Nauchnye doklady vysshei shkoly. Khimiia i khimicheskaia tekhnologiia: 710-713.

Kulik, D., 2009. Thermodynamic concepts in modeling sorption at the mineral-water interface. Reviews in Mineralogy and Geochemistry, 70(1): 125.

Langmuir, I., 1916. The constitution and fundamental properties of solids and liquids. Part I. Solids. Journal of the American Chemical Society, 38(11): 2221-2295.

Leuz, A., Mönch, H., Johnson, C., 2006. Sorption of Sb (III) and Sb (V) to Goethite: Influence on Sb (III) Oxidation and Mobilization. Environ. Sci. Technol, 40(23): 7277-7282.

Leyva, A., Marrero, J., Smichowski, P., Cicerone, D., 2001. Sorption of antimony onto hydroxyapatite. Environ. Sci. Technol, 35(18): 3669-3675.

Manceau, A., Chateigner, D., Gates, W., 1998. Polarized EXAFS, distance-valence least-squares modeling (DVLS), and quantitative texture analysis approaches to the

structural refinement of Garfield nontronite. Physics and Chemistry of Minerals, 25(5): 347-365.

Manceau, A. et al., 2000. Oxidation-reduction mechanism of iron in dioctahedral smectites: II. Crystal chemistry of reduced Garfield nontronite. American Mineralogist, 85(1): 153.

McKay, J., 1992. Clay separation; LSIS Technical memorandum #92-1. University of Western Ohio.

Mitsunobu, S., Takahashi, Y., Terada, Y., 2010. μ-XANES Evidence for the Reduction of Sb (V) to Sb (III) in Soil from Sb Mine Tailing. Environmental Science & Technology: 79-90.

Moore, P.B., Araki, T., 1976. Bahianite, Al5Sb3O14(O,OH)2, a novel hexagonal close-packed oxide structure. Locality: Serra de Mangabeira, Bahia, Brazil. Neues Jahrbuch fur Mineralogie, Abhandlungen (126): 113-125.

Nakamaru, Y., Tagami, K., Uchida, S., 2006. Antimony mobility in Japanese agricultural soils and the factors affecting antimony sorption behavior. Environmental Pollution, 141(2): 321-326.

Newville, M., 2001. IFEFFIT: interactive XAFS analysis and FEFF fitting. Journal of Synchrotron Radiation, 8(2): 322-324.

Newville, M., Livins, P., Yacoby, Y., Rehr, J., Stern, E., 1993. Near-edge x-ray-absorption fine structure of Pb: A comparison of theory and experiment. Physical Review B, 47(21): 14126-14131.

Olivé, I., 2006. Mobility of Lead and Antimony in Shooting Range Soils, Swiss Federal Institute of Technology Zurich.

Olmi, F., Sabelli, C., 1994. Brizzite, NaSbO3, a new mineral from the Cetine mine (Tuscany, Italy): description and crystal structure. European journal of mineralogy, 6(5): 667-672.

Pilarski, J., Waller, P., Pickering, W., 1995. Sorption of antimony species by humic acid. Water, Air, & Soil Pollution, 84(1): 51-59.

Rauf, M., Ikram, M., Hasany, S., 1994. Adsorption studies of antimony on manganese dioxide using radiometric techniques. Adsorption science & technology, 11(1): 41-50.

Ravel, B., Newville, M., 2005. ATHENA, ARTEMIS, HEPHAESTUS: data analysis for X-ray absorption spectroscopy using IFEFFIT. Journal of Synchrotron Radiation, 12(4): 537-541.

Reimann, C., Matschullat, J., Birke, M., Salminen, R., 2010. Antimony in the environment: lessons from geochemical mapping. Applied Geochemistry, 25: 175-198.

Sabadell, J., Axtmann, R., 1975. Heavy metal contamination from geothermal sources. Environmental Health Perspectives, 12: 1.

Scheinost, A. et al., 2006. Quantitative antimony speciation in shooting-range soils by EXAFS spectroscopy. Geochimica et cosmochimica acta, 70(13): 3299-3312.

Stucki, J., 2006. Properties and behaviour of iron in clay minerals. Handbook of Clay Science: 423–475.

Stucki, J., Golden, D., Roth, C., 1984a. Effects of reduction and reoxidation of structural iron on the surface charge and dissolution of dioctahedral smectites. Clays and Clay Minerals, 32(5): 350-356.

Stucki, J., Golden, D., Roth, C., 1984b. Preparation and handling of dithionite-reduced smectite suspensions. Clays and Clay Minerals, 32(3): 191-197.

Thanabalasingam, P., Pickering, W., 1990. Specific sorption of antimony (III) by the hydrous oxides of Mn, Fe, and Al. Water, Air, & Soil Pollution, 49(1): 175-185.

Tighe, M., Lockwood, P., Wilson, S., 2005. Adsorption of antimony (V) by floodplain soils, amorphous iron (III) hydroxide and humic acid. Journal of Environmental Monitoring, 7(12): 1177-1185.

Trivedi, P., Axe, L., 1999. A comparison of strontium sorption to hydrous aluminum, iron, and manganese oxides. Journal of colloid and interface science, 218(2): 554-563.

Watkins, R. et al., 2006. Investigations into the kinetics and thermodynamics of Sb (III) adsorption on goethite ([alpha]-FeOOH). Journal of colloid and interface science, 303(2): 639-646.

Whitten, A., Dittrich, B., Spackman, M., Turner, P., Brown, T., 2004. Charge density analysis of two polymorphs of antimony (III) oxide. Dalton transactions, 2004(1): 23-29.

Wilson, N., Craw, D., Hunter, K., 2004. Antimony distribution and environmental mobility at an historic antimony smelter site, New Zealand. Environmental Pollution, 129(2): 257-266.

Wilson, N., Webster-Brown, J., 2009. The fate of antimony in a major lowland river system, the Waikato River, New Zealand. Applied Geochemistry.

Wilson, S., Lockwood, P., Ashley, P., Tighe, M., 2010. The chemistry and behaviour of antimony in the soil environment with comparisons to arsenic: A critical review. Environmental Pollution(158): 1169-1181.

Xu, Y., Ohki, A., Maeda, S., 2001. Adsorption and removal of antimony from aqueous solution by an activated alumina. Toxicological & Environmental Chemistry, 80(3): 133-144.

Zabinsky, S., Rehr, J., Ankudinov, A., Albers, R., Eller, M., 1995. Multiple-scattering calculations of x-ray-absorption spectra. Physical Review B, 52(4): 2995-3009.

Table 4.1. Summary of the experimental conditions and resulting uptake for the EXAFS samples; pH was adjusted to 5.5 (±0.5) in the beginning of each experiment and then measured at the end. The pH drift in all cases did not exceed 1 pH unit. The analytical errors in determining initial and final Sb concentrations are ≤10%

| Sample | Substrate[a] | $S_A$ $m^2 \cdot g^{-1}$ | Vol mL | C initial µM | C eq µM | Initial pH | I M | Rxn time hrs | UV light | Atm | Uptake µmoles·$g^{-1}$ | Γ[b] sites·$nm^{-2}$ |
|---|---|---|---|---|---|---|---|---|---|---|---|---|
| ***Antimony(III)*** | | | | | | | | | | | | |
| RN-Sb-3[c] | NAu-1 *reduced* | 69.5 | 35 | ~46 | ~26 | 5.11 | 0.01 | 24 | + | $N_2$ | ~42 | 0.36 |
| N-Sb-3 | NAu-1 | 85.3 | 200 | 116.4 | 1.27 | 5.55 | 0.01 | 24 | - | $N_2$ | 230.2 | 1.63 |
| HAO-Sb-3 | HAO | 196 | 200 | 120.7 | 45.37 | 5.54 | 0.01 | 65.5 | + | $N_2$ | 150.6 | 0.46 |
| K-Sb-3 | KGa-1b | 11.0 | 200 | 120.7 | 109.6 | 5.47 | 0.01 | 38.5 | + | $N_2$ | 22.2 | 1.21 |
| ***Antimony(V)*** | | | | | | | | | | | | |
| K-Sb-5-high | KGa-1b | 11.0 | 35 | 2000 | 363.6 | 4.94 | 0.01 | 24 | + | $O_2$ | 3274 | 179 |
| K-Sb-5-low | KGa-1b | 11.0 | 30 | 10.01 | 2.98 | 5.53 | 0.01 | 200 | + | $N_2$ | 14.1 | 0.77 |
| Sb-5-HAO | HAO | 196 | 200 | 100.1 | 71.61 | 5.46 | 0.01 | 38.5 | + | $O_2$ | 57.0 | 0.17 |
| N-Sb-5 | NAu-1 | 85.3 | 30 | 2000 | 43.02 | 5.45 | 0.01 | 24 | - | $N_2$ | 3914 | 27.6 |
| RN-Sb-5 | NAu-1 *reduced* | 69.5 | 30 | 2000 | 37.55 | 5.48 | 0.01 | 24 | - | $N_2$ | 3925 | 34.0 |

[a] Mass of substrate in each sample 0.50 g
[b] Surface coverage, estimated maximum mono-layer coverage is 6.25 sites·$m^{-2}$
[c] Uptake is calculated based on identical sample

Table 4.2. Summary of Langmuir and Freundlich isotherm fitting parameters

| ***Substrate*** | ***Sorbate*** | $R^2_F$ | $R^2_L$ | $K_F$ $L \cdot \mu mol^{-1}$ | ***n*** | $K_L \times 10^{-2}$ $L \cdot \mu mol^{-1}$ | $\Gamma_{max}$ $\mu moles \cdot m^{-2}$ |
|---|---|---|---|---|---|---|---|
| KGa-1b | $Sb^{3+}$ | 0.999 | 0.947 | 6.23 | 0.499 | 6.16 | 62.50 |
| KGa-1b | $Sb^{5+}$ | 0.985 | 0.946 | 6.02 | 0.434 | 4.01 | 73.53 |
| NAu-1 | $Sb^{3+}$ | 0.946 | 0.024 | 0.51 | 1.026 | 0.38 | 138.89 |
| NAu-1 | $Sb^{5+}$ | 0.986 | 0.994 | 0.23 | 0.809 | 1.84 | 12.21 |
| Reduced NAu-1 | $Sb^{3+}$ | 0.981 | 0.323 | 0.09 | 1.033 | n/a | n/a |
| Reduced NAu-1 | $Sb^{5+}$ | 0.978 | 0.427 | 2.01 | 0.890 | 0.22 | 769.23 |

Table 4.3. Metal-oxygen bond length from the known structures

| ***Bond*** | ***Length*** | ***Reference*** |
|---|---|---|
| $Sb^{3+}$-O | 1.92-2.04 Å | Scheinost et al., 2006 |
| $Sb^{5+}$-O | 1.98-2.10 Å | Scheinost et al., 2006 |
| Al-O | 1.87, 1.93 Å | Bish and Von Dreele, 1989 |
| $Fe^{2+}$-O | 2.154 Å | Fjellvag et al., 2002 |
| $Fe^{3+}$-O | 1.97, 2.03, 2.04 Å | Manceau et al., 1998 |

Table 4.4. Possible sorption geometries and theoretical interatomic distances

| 2nd shell | Antimony (III) | | |
|---|---|---|---|
| | 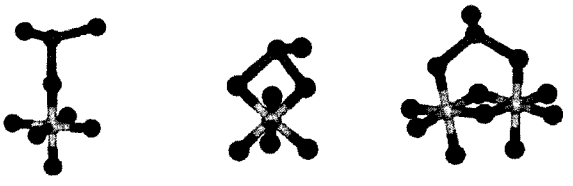 | | |
| Al | 3.79-3.97 Å | 2.68-2.81 Å | 3.54-3.79 Å |
| Fe (II) | 4.07-4.19 Å | 2.89-2.97 Å | 3.76-3.89 Å |
| Fe (III) | 3.89-4.08 Å | 2.75-2.89 Å | 3.57-3.77 Å |
| 2nd shell | Antimony (V) | | |
| | 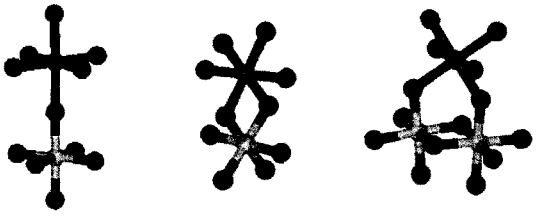 | | |
| Al | 3.85-4.03 Å | 2.78-2.98 Å | 3.58-3.78 Å |
| Fe (II) | 4.13-4.25 Å | 2.98-3.15 Å | 3.76-3.92 Å |
| Fe (III) | 3.95-4.14 Å | 2.83-3.05 Å | 3.65-3.86 Å |

Table 4.5. EXAFS resulting fitting parameters for $Sb^{3+}$ and $Sb^{5+}$ immobilized by Al-rich substrates. K-weight of 1 was used for $Sb^{3+}$ samples, and k-weights of 1,2, and 3 were fitted simultaneously for $Sb^{5+}$ samples

| Sample | FEFF model | R-range (Å) | k-range | Shell | N | R (Å) | σ2 | ΔEo | R-factor | Red χ2 | Indep. Pts | So |
|---|---|---|---|---|---|---|---|---|---|---|---|---|
| ***Antimony(III)*** | | | | | | | | | | | | |
| HAO-Sb-3 | Bahianite | 1.000-3.678 | 2.661-9.573 | Sb-O | 3.2(6) | 1.95(1) | 0.002(2) | 8(2) | 0.018 | 1.86 | 11.5 | 0.98 |
| | | | | Sb-Al | 4(1) | 3.44(3) | 0.002(6) | | | | | |
| | | | | Sb-Al | 4(2) | 3.78(4) | 0.002(6) | | | | | |
| K-Sb-3 | Bahianite | 1.000-3.211 | 2.767-10.148 | Sb-O | 3.7(4) | 1.95(1) | 0.002(2) | 9(1) | 0.013 | 1.36 | 10.1 | 1 |
| | | | | Sb-Al | 2(2) | 3.37(8) | 0.01(1) | | | | | |
| N-Sb-3 | Bahianite | 1.000-4.066 | 2.562-11.060 | Sb-O | 3.7(2) | 1.96(1) | 0.003(1) | 9.1(7) | 0.004 | 2.3 | 16.9 | 1 |
| | | | | Sb-Al | 0.9(5) | 3.39(7) | 0.005(6) | | | | | |
| | | | | Sb-Sb | 2(1) | 3.97(4) | 0.009(4) | | | | | |
| RN-Sb-3 | Bahianite | 1.000-4.071 | 2.562-11.060 | Sb-O | 3.6(2) | 1.96(1) | 0.001(1) | 7.8(8) | 0.010 | 4.18 | 16.3 | 1 |
| | | | | Sb-Al | 1.7(8) | 3.39(4) | 0.003(4) | | | | | |
| | | | | Sb-Sb | 0.9(4) | 3.97(2) | 0.007(2) | | | | | |
| ***Standard*** | | | | | | | | | | | | |
| $Sb_2O_3$ | Bahianite | 1.000-4.379 | 2.453-11.367 | Sb-O | 2.8(3) | 1.98(1) | 0.002(1) | 8(1) | 0.070 | 4332 | 18.8 | 1 |
| | | | | Sb-Sb | 1.1(6) | 3.37(2) | 0.003(2) | | | | | |
| | | | | Sb-Sb | 1(1) | 3.68(5) | 0.005(5) | | | | | |
| | | | | Sb-Sb | 1(1) | 3.95(7) | 0.006(8) | | | | | |
| ***Antimony(V)*** | | | | | | | | | | | | |
| HAO-Sb-5 | Bahianite | 1.000-4.078 | 2.554-11.990 | Sb-O | 6.0(4) | 1.97(1) | 0.002(1) | 9.0(7) | 0.004 | 468 | 18 | 0.93 |
| | | | | Sb-Al | 3(1) | 3.8(1) | 0.009(4) | | | | | |
| | | | | Sb-Al | 6(4) | 4.02(6) | 0.016(7) | | | | | |
| K-Sb-5-low | Bahianite | 1.000-3.609 | 2.596-10.888 | Sb-O | 6.0(4) | 1.95(1) | 0.001(1) | 8(1) | 0.013 | 10.4 | 13.5 | 1 |
| | | | | Sb-Al | 4(1) | 3.74(2) | 0.004(9) | | | | | |
| K-Sb-5-high | Bahianite | 1.000-3.396 | 2.600-10.900 | Sb-O | 6.5(7) | 1.96(1) | 00003(1) | 5.4(7) | 0.004 | 98.6 | 12.4 | 0.87 |
| | | | | Sb-Sb | 0.7(2) | 3.19(1) | 0.003(1) | | | | | |
| | | | | Sb-Al | 1.9(6) | 3.67(2) | 0.005(1) | | | | | |
| N-Sb-5 | Bahianite | 1.000-4.275 | 2.562-10.000 | Sb-O | 3.7(3) | 1.96(1) | 0.002(1) | 8.1(9) | 0.003 | 11.48 | 15.3 | 0.98 |
| | | | | Sb-Sb | 2(2) | 3.25(7) | 0.008(9) | | | | | |
| | | | | Sb-Sb | 0.3(9) | 4.0(2) | 0.002(8) | | | | | |
| RN-Sb-5 model 1 | Bahianite | 1.000-4.109 | 2.542-9.869 | Sb-O | 5.7(5) | 1.97(1) | 0.003(1) | 7(2) | 0.005 | 168.1 | 14 | 0.98 |
| | | | | Sb-Sb | 2(2) | 3.23(6) | 0.006(9) | | | | | |
| | | | | Sb-Sb | 1(1) | 4.01(7) | 0.005(9) | | | | | |
| RN-Sb-5 model 2 | Bahianite Bahianite | 1.000-4.109 | 2.542-9.869 | Sb-O | 5.7(6) | 1.97(1) | 0.003(1) | 7(2) | 0.006 | 222.49 | 14 | 0.98 |
| | | | | Sb-Sb | 0.9(5) | 3.26(4) | 0.005(5) | | | | | |
| RN-Sb-5 model 3 | Bahianite Bahianite Tripuhyite | 1.000-4.109 | 2.542-9.869 | Sb-O | 5.0(5) | 1.97(1) | 0.001(1) | 7(2) | 0.003 | 105.17 | 14 | 0.98 |
| | | | | Sb-Sb | 2(2) | 3.28(1) | 0.01(1) | | | | | |
| | | | | Sb-Fe | 1(1) | 3.80(8) | 0.01(1) | | | | | |
| ***Standard*** | | | | | | | | | | | | |
| $KSb(OH)_6$ | Stibiconite | 1.000-4.116 | 2.481-12.766 | Sb-O | 6.2(6) | 1.98(2) | 0.002(1) | 7(1) | 0.008 | 1171 | 20.2 | 0.87 |
| | | | | Sb-Sb | 1.2(5) | 3.07(2) | 0.003(2) | | | | | |

Table 4.6. $Sb^{3+}$ on HAO (no Fe in the sample): comparison of two structural models with Al vs. Fe in the second shell

| *Sample* | *FEFF model* | *R-range (Å)* | *k-range* | *Shell* | *N* | *R (Å)* | *σ2* | *ΔEo* | *R-factor* | *Red χ2* | *Indep. Pts* | *So* |
|---|---|---|---|---|---|---|---|---|---|---|---|---|
| HAO-Sb-3 | Bahianite | 1.000-3.678 | 2.661-9.573 | Sb-O | 3.2(6) | 1.95(1) | 0.002(2) | 8(2) | 0.018 | 1.86 | 11.5 | 0.98 |
| | | | | Sb-Al | 4(1) | 3.44(3) | 0.002(6) | | | | | |
| | | | | Sb-Al | 4(2) | 3.78(4) | 0.002(6) | | | | | |
| HAO-Sb-3 | Tripuhyite | 1.000-3.635 | 2.661-9.573 | Sb-O | 3.0(2) | 1.95(1) | 0.001(1) | 9(1) | 0.029 | 3.04 | 11.4 | 0.98 |
| | | | | Sb-Fe | 3(2) | 3.60(4) | 0.003(4) | | | | | |

Table 4.7. Comparison of Al, Fe, and Sb in the second shell of the $Sb^{5+}$ on KGa-1b

| | | | | | | *k-weight=1* | | *k-weight=2* | | *k-weight=3* | | | |
|---|---|---|---|---|---|---|---|---|---|---|---|---|---|
| *Sample* | *k-range* | *R-range (Å)* | *2nd shell* | *N* | *R (Å)* | *Red χ²* | *R-factor* | *Red χ²* | *R-factor* | *Red χ²* | *R-factor* | *Ind Pts* | *σ²* |
| K-Sb-5-low | 2.596 - 9.135 | 2.799-3.609 | Al | 4(2)-6(2) | 3.74 | **1.84** | 0.09 | 1.04 | 0.05 | 1.88 | 0.02 | 3 | 0.005 |
| | | | Fe | 2.8(5)-3(1) | 3.48 | **1.58** | 0.08 | **0.36** | 0.02 | **0.29** | 0.002 | 3 | 0.005 |
| | | | Sb | 2(1)-2.7(7) | 3.24 | **2.93** | 0.15 | 0.99 | 0.05 | **0.71** | 0.006 | 3 | 0.005 |
| K-Sb-5-low | 2.596 - 10.888 | 2.799-3.609 | Al | 4(1-3) | 3.74 | **0.94** | 0.07 | **1.13** | 0.11 | **5.07** | 0.20 | 4 | 0.005 |
| | | | Fe | 1-2(2) | 3.48 | 3.36 | 0.25 | 3.20 | 0.33 | **10.24** | 0.40 | 4 | 0.005 |
| | | | Sb | 2.7(7) | 3.24 | 3.58 | 0.27 | 3.79 | 0.39 | 12.97 | 0.51 | 4 | 0.005 |

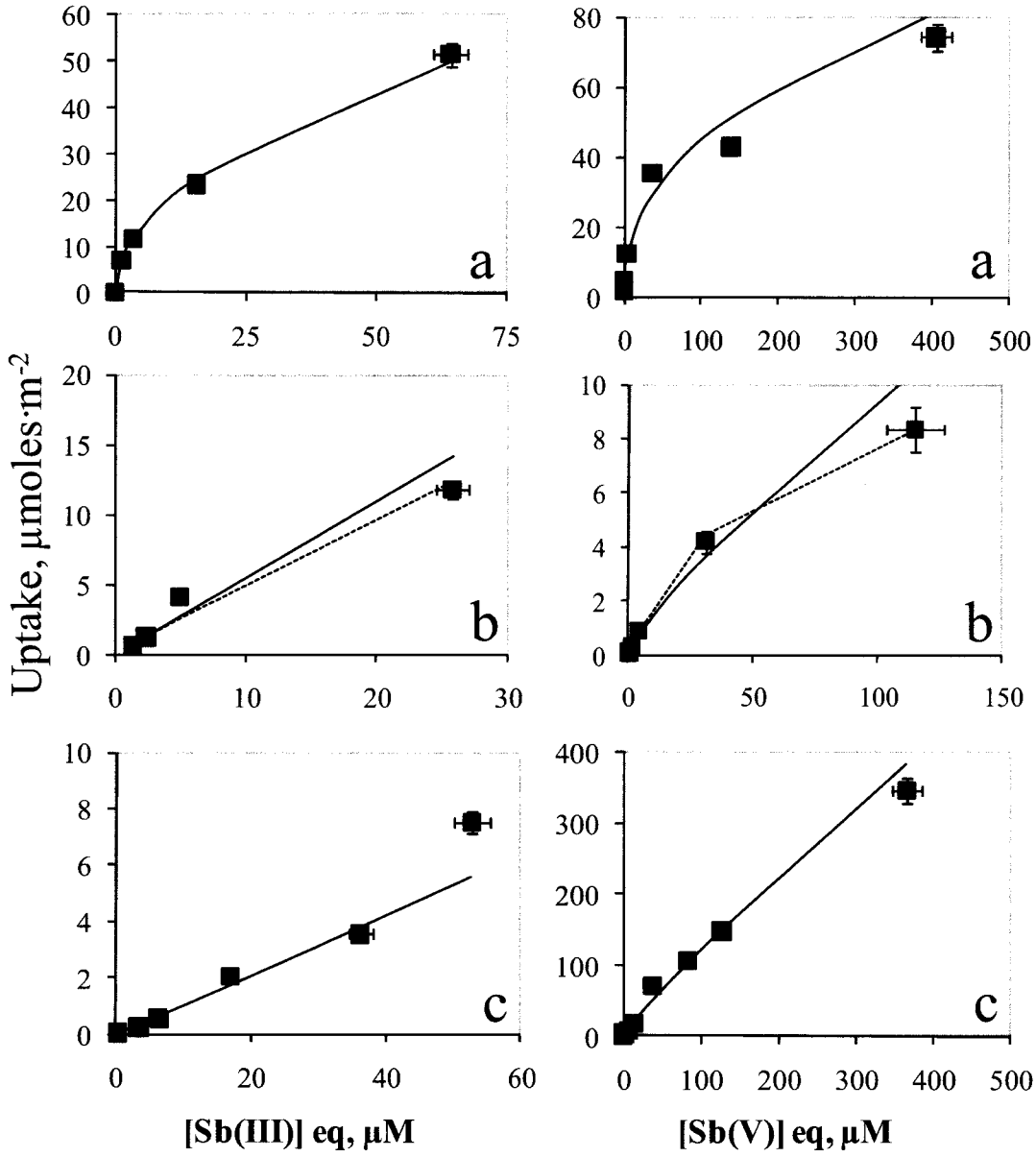


Figure 4.1. Sorption isotherms and fits for $Sb^{3+}$ and $Sb^{5+}$ on clay substrates (a)KGa-1b, (b)NAu-1 oxidized, and (c)NAu-1 reduced. Freundlich model is shown as solid line, Langmuir model – as dashed line

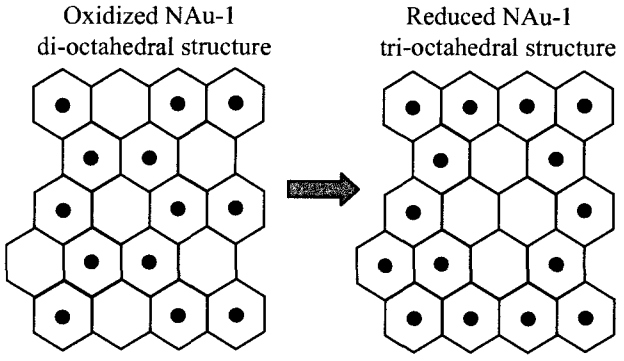


Figure 4.2. Re-arrangement from di-octahedral to tri-octahedral clay sheet structure due to nontronite reduction: more edge sites with two Fe octahedra available for $Sb^{5+}$ adsorption

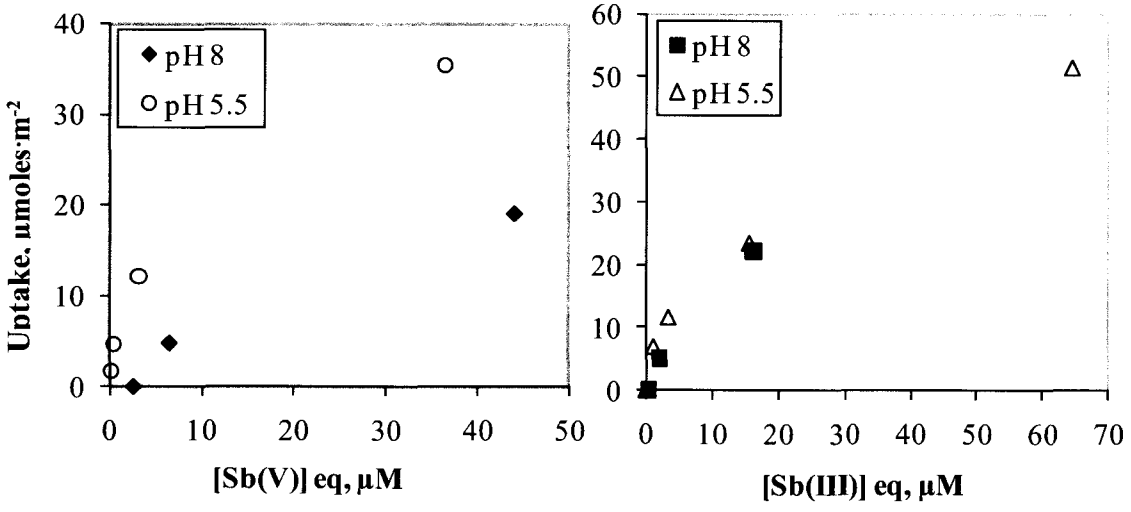


Figure 4.3. $Sb^{5+}$ and $Sb^{3+}$ adsorption on KGa-1b at pH 5.5 compared to pH 8.0; $Sb^{5+}$ is adsorbed better at pH 5.5, while $Sb^{3+}$ adsorption is similar at pH 5.5 and pH 8.0. Error bars for uptake and aqueous concentrations are ≤10%

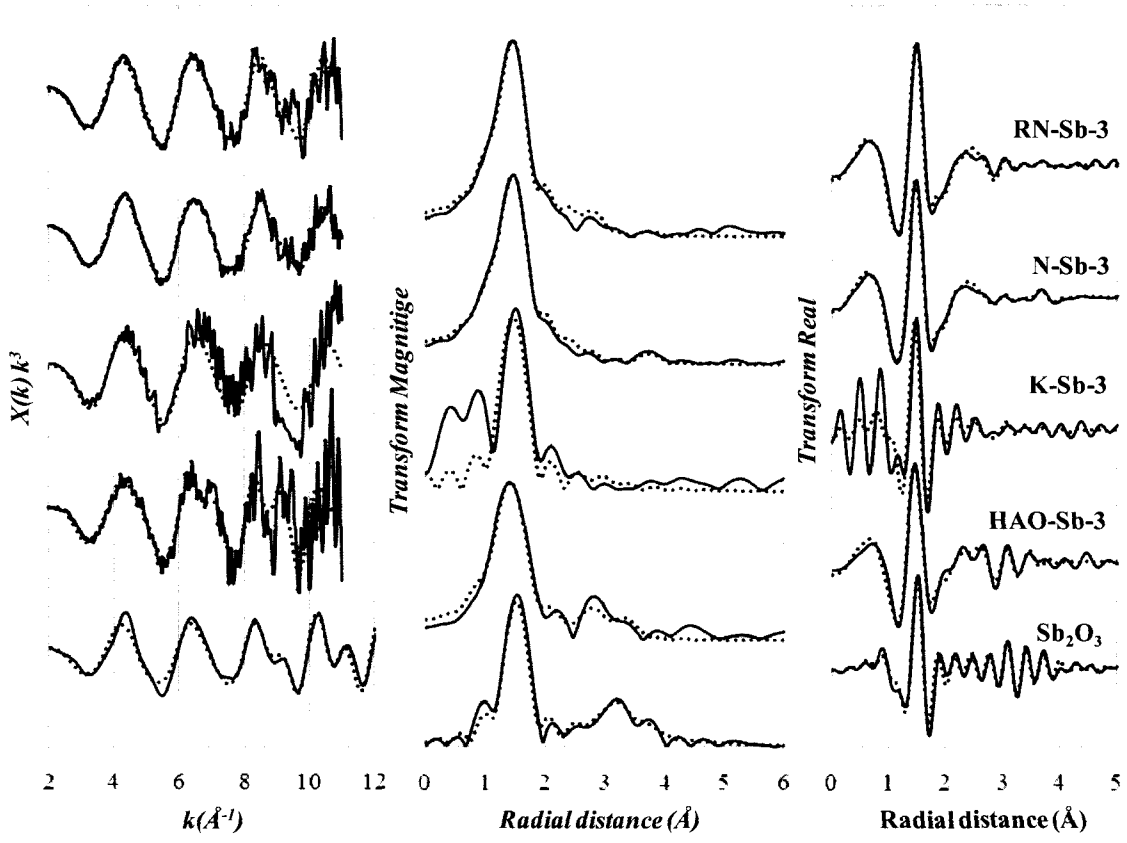


Figure 4.4. EXAFS data (solid lines) and fits (dashed lines) of $Sb^{3+}$ model compound $Sb_2O_3$ and $Sb^{3+}$ adsorbed to HAO, KGa-1b, oxidized and reduced NAu-1

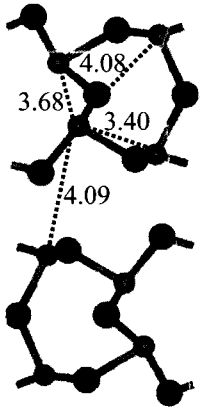


Figure 4.5. Structure of valentinite $Sb_2O_3$ with characteristic Sb-Sb distances

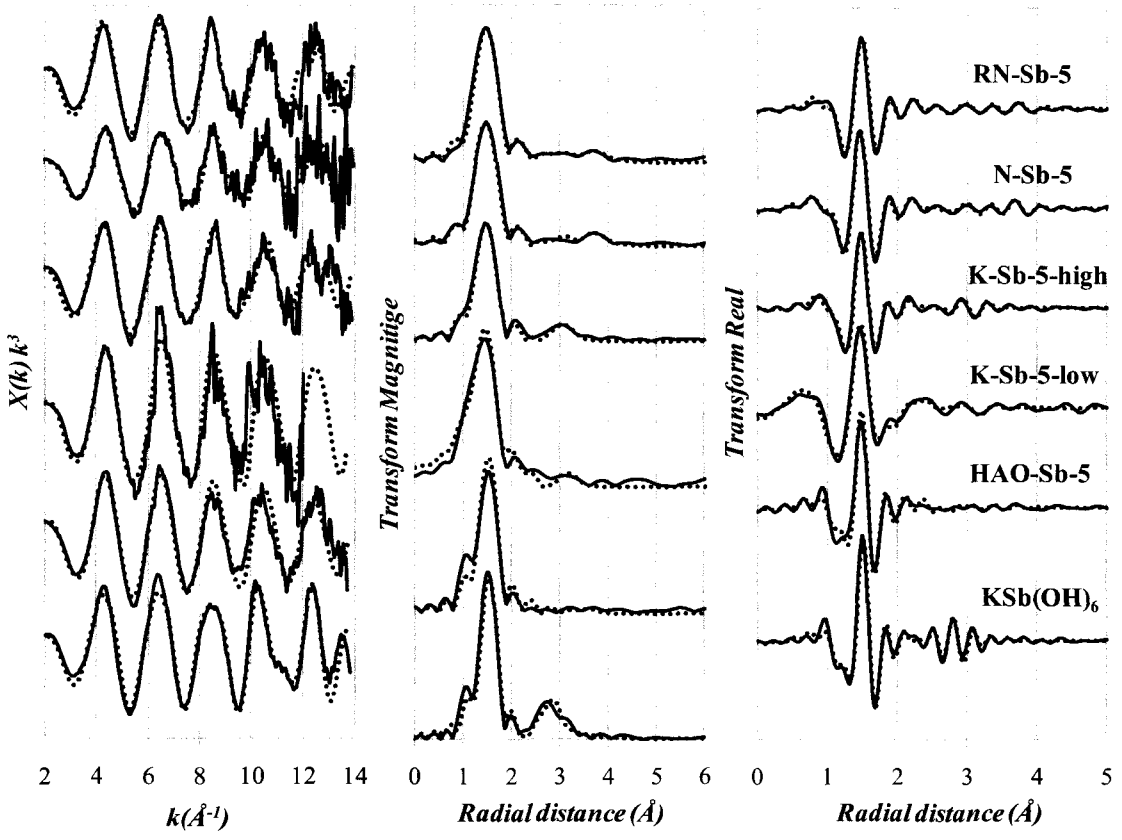


Figure 4.6. EXAFS data (solid lines) and fits (dashed lines) of $Sb^{5+}$ model compound $KSb(OH)_6$ and $Sb^{5+}$ adsorbed to HAO, KGa-1b, oxidized and reduced NAu-1

# Chapter 5: Conclusions and Future Work

This project provides detailed data on the chemical forms and heterogeneous redox reactions of As and Sb at the clay mineral - water interface in natural and laboratory conditions. Partitioning and redox reactions play a key role in the environmental fate and transport of arsenic and antimony. The molecular-level understanding of these reactions is crucial for predicting aqueous concentrations of these contaminants in ground and surface waters.

## 5.1 As and Sb Redox Transformations in Clay-rich Laboratory Systems

One of the most important and unexpected experimental findings presented in this thesis is that the oxidation potential of the structural $Fe^{3+}$ in nontronite clay can be modified by the partial reduction. The fully oxidized nontronite (NAu-1) is not able to significantly oxidize $As^{3+}$ and $Sb^{3+}$; however, if some structural $Fe^{3+}$ is reduced to $Fe^{2+}$ and, as a result a mixture of $Fe^{2+}/Fe^{3+}$ is present, the substrate acts as a strong oxidant. This reaction was confirmed by two independent sets of experiments and by two analytical methods: XAS and LC-ICP-MS. This reaction is not catalyzed by light. The two most likely reasons for the increased oxidation capacity are: 1) Structural re-arrangements in reduced nontronite, namely a partial change from di- to tri-octahedral structure (Manceau et al., 2000; Stucki et al., 2002), provide sites suitable for $e^-$ transfer; 2) Structural $Fe^{2+}$ may act as a catalyst for this oxidation reaction. This reaction has very important implications for As and Sb retention in natural soil environments where partially reduced clays are abundant (Stucki, 2006). The reduced $As^{3+}$ is more mobile than the oxidized $As^{5+}$, while for Sb the opposite is true: the oxidized $Sb^{5+}$ has higher mobility than the reduced $Sb^{3+}$. Therefore, partially reduced Fe-rich clay acting as an oxidant has the ability to decrease the mobility of As and increase the mobility of Sb in soil.

A potentially important direction for future work is to study the exact mechanism of $As^{3+}$ and $Sb^{3+}$ oxidation by the structural $Fe^{3+}$ in partially reduced nontronite, and to

determine the mechanism by which structural $Fe^{2+}$ is able to catalyze this reaction. Previous studies of chemically reduced smectite illustrate that during reduction a maximum possible number of $Fe^{2+}$-O-$Fe^{3+}$ linkages in the octahedral sheet are formed (Stucki, 2006). Perhaps $Fe^{3+}$ in this unit has the ability to oxidize $As^{3+}$ and $Sb^{3+}$, while in the $Fe^{3+}$-O-$Fe^{3+}$ unit $Fe^{3+}$ is much less reactive. In order to determine whether $Fe^{3+}$ in the $Fe^{2+}$-O-$Fe^{3+}$ linkages is preferentially involved in the oxidation reaction, visible absorption spectroscopy can be used (by monitoring the intervalence electron transfer band) during the oxidation reaction. In order to determine the kinetics of the adsorbed As/Sb and structural Fe oxidation state changes, spectroscopic techniques should be used; for example, time-resolved As/Sb and Fe EXAFS measurements should be used to examine the oxidation state changes over the course of the oxidation reaction (time scale of hours). Another important direction is to establish whether structural Fe in clay is stable during these reactions and whether or not it is dissolved and re-precipitated as Fe-oxide; this can be done by means of Mossbauer spectroscopy (Stucki, 2006).

The abiotic reduction of $As^{5+}$ to $As^{3+}$ by aqueous $Fe^{2+}$ was observed in the studied systems, previously reported by other researchers (Bose and Sharma, 2002; Charlet et al., 2005). Also, the observed reduction rate was dependant on the concentration of $Fe^{2+}$ and was similar to the aqueous rate (slow, on the order of days). Therefore studied clays did not exhibit the ability to promote this reduction as described for montmorillonite and phlogopite in the previous studies (Charlet et al., 2002; Charlet et al., 2005). The reaction mechanism proposed for the phlogopite and montmorillonite systems included simultaneous adsorption and redox reaction between $As^{5+}$ and $Fe^{2+}$ at the edge sites, and products of this reaction, namely precipitation of Fe-oxide, were preferentially observed at the edge-like defects on the surface of phlogopite in the previous studies (Charlet et al., 2002; Charlet et al., 2005). The substrates used in the current study should have the same edge adsorption sites and a similar ability to adsorb both $Fe^{2+}$ and $As^{5+}$. Future work is therefore needed to determine the exact controls of this reduction reaction: why is it fast (compared to the homogeneous rate) in the presence

of phlogopite and montmorillonite (Charlet et al., 2002), but not kaolinite and nontronite (this study)?

As described in Chapter 3, $Sb^{5+}$ is reduced by dissolved $Fe^{2+}$ in the presence of kaolinite and notnronite as determined by XAS. The extent of reduction over the 24 hour period is dependant on the nature of the substrate: reduction is more pronounced in the presence of kaolinite (KGa-1b) when compared to nontronite (NAu-1). This substrate effect can be due to the differences in adsorption of the reactants/products (Fe and Sb), or due to different degrees of aqueous $Fe^{2+}$ oxidation by these substrates. If adsorption is the primary control, it is expected that due to the higher surface area of nontronite (NAu-1) compared to kaolinite KGa-1b (85 vs.11 $m^2/g$), nontronite will adsorb more $Fe^{2+}$, and therefore decrease the aqueous concentartion of $Fe^{2+}$ available for reduction. This observation indirectly suggests that this reduction is homogeneous. There is currently no study of the homogeneous reduction of $Sb^{5+}$ by $Fe^{2+}$ and the rates cannot be compared to this study. These two species ($Sb^{5+}$ and $Fe^{2+}$) are likely to co-exist in a natural environment due to close standard redox potentials of the transformations shown in reactions 1-3 (data from (Wilson et al., 2010)).

$$Fe(OH)_3 \text{ (amorphous)} + 3H^+ + e^- \rightarrow Fe^{2+} + 3H_2O \quad E^o = 0.98 \text{ V} \quad (1)$$

$$\alpha\text{-FeOOH (goethite)} + 3H^+ + e^- \rightarrow Fe^{2+} + 2H_2O \quad E^o = 0.77 \text{ V} \quad (2)$$

$$Sb(OH)_6^- + 3H^+ + 2e^- \rightarrow Sb(OH)_3 + 3H_2O \quad E^o = 0.76 \text{ V} \quad (3)$$

Future work should include a study of the kinetics of homogeneous Sb redox reactions likely to take place in natural water; this data is crucial for determining whether mineral substrates have the ability to increase or decrease the rate of redox transformations compared to the rate of the homogeneous reduction.

Further differences between As and Sb reactivity associated with mineral substrates are illustrated in Chapter 3: the Ti-catalyzed oxidation reaction described for As is not pronounced for Sb; the observed extent of Sb oxidation in the presence of kaolinite (KGa-1b) was significantly smaller than the extent of As oxidation under similar conditions. The redox half-reaction for As:

$$H_3AsO_4 + 2H^+ + 2e^- \rightarrow H_3AsO_3 + H_2O \qquad (4)$$

has the standard redox potential of 0.56 V (Wilson et al., 2010), which is lower than the 0.76 V for the similar Sb reduction half-reaction. Even though the redox potentials of adsorbed species can differ significantly from those for the aqueous species, the difference in the tabulated standard potentials indicates that, in general, during arsenic oxidation by dissolved $O_2$, the resulting value of the Gibbs free energy $\Delta G^o$ is more negative than the value for Sb, causing Sb not to be oxidized as readily.

### 5.2 Sb Immobilization by Clays: Soption and Speciation

The experimental work presented in this thesis also illustrates that Al-oxide and clay minerals (kaolinite and nontronite) are capable of immobilizing Sb by chemisorption. The resulting sorption complexes identified by EXAFS have mostly bi-dentate corner-sharing geometry, with some mono-dentate corner-sharing complexes forming on the surfaces of hydrous aluminum oxide. Knowledge about the mechanism and stoichiometry of Sb adsorption on the clay substrates and hydrous aluminum oxide is important in surface complexation modeling for predicting the aqueous concentrations of Sb in equilibrium with Al-rich substrates. On the surfaces of some of the substrates used in this study antimony formed poly-nuclear complexes; this effect was most pronounced in the reduced nontronite system, likely due to the presence of dissolved $Fe^{2+}$ in equilibrium with reduced nontronite. As a result, the macroscopic uptake was the highest in this system. Future work should therefore be focused on the effect of dissolved $Fe^{2+}$ in modifying clay surfaces and the mechanisms of inducing surface precipitation of $Sb^{5+}$; this has important implications for potential Sb mobilization from these substrates.

It is shown in Chapter 4 that determining the nature of adsorbing substrates, more specifically distinguishing between Fe and Al in the 2$^{nd}$ shell of Sb, can be impossible without constraining the chemical composition of the sample; therefore, another important direction for future work would be establishing a more complete database of

model Sb adsorption samples and establishing a reliable procedure for determining the nature of the adsorbing substrate in mixed mineral samples. This is important for assessing Sb transport in a natural environment since the stability of the adsorbed Sb depends on the exact nature of the bonding and identity of the mineral substrate.

### 5.3 As Speciation and Redox Transformations in Clay-rich Natural Setting

In the field study described in Chapter 2, geothermal waste water discharged in surface river water created localized areas of As contamination. The extent of elevated As aqueous concentration is limited by dilution and by adsorption to the river sediment. Reduced $As^{3+}$ is found in the geothermal fluids, and a mixture of $As^{3+}/As^{5+}$ is found in the Falshivaia River water and sediment. Due to mixing with the waste fluid, the Falshivaia River water is at thermodynamic disequilibrium downstream from the power plant as shown by calculating the redox potential based on the major redox couples: $HS^-/SO_4^{2-}$, $Fe^{2+}/Fe^{3+}$, and $NH_4^+/NO_3^-$. Similarly to other reports (Webster-Brown and Lane, 2005), geothermal $As^{3+}$ is oxidized to $As^{5+}$ after $HS^-$ (or $S^{2-}$) is oxidized to $SO_4^{2-}$ in surface water. Based on the field data, it is not possible to determine whether oxidation of $As^{3+}$ to $As^{5+}$ is predominantly a homo- or heterogeneous reaction, since both forms were found in aqueous and adsorbed states. The similar degree of $As^{3+}$ and $As^{5+}$ distribution between water and sediment can be interpreted as similar affinity of these two forms towards the sediment; however, the equilibrium between aqueous and adsorbed forms is unlikely in this setting. Another complication arises due to the operational definition of the "dissolved" form based on the 0.45 μm filtration. It is likely that colloidal Fe- and Al-oxyhydroxides that pass through the filter and later dissolve due to sample preservation techniques, acidification with HCl, cause over-estimation of the aqueous As content. Laboratory studies find that $As^{3+}$ has a lower affinity towards mineral surfaces compared to $As^{5+}$ (Stollenwerk, 2003); therefore, similar $As^{3+}/As^{5+}$ ratios in the sediment and aqueous phase in the field setting indicate that adsorption might inhibit oxidation reactions.

Similarly to the Sb adsorption samples described in Chapter 4, identifying whether Al or Fe atoms are in the As 2$^{nd}$ shell in the field samples (is As adsorbed to an Al- or Fe-rich substrate?) was not straight forward. When the full EXAFS spectrum (1$^{st}$ and 2$^{nd}$ shells) was considered, there was no statistical difference between a fit with Fe vs. a fit with Al 2$^{nd}$ shell as determined using standard procedures (Kelly et al., 2008). When EXAFS data for the isolated 2$^{nd}$ shell was fitted with either As-Al or As-Fe calculated single scattering paths, the resulting fits were statistically different. Based on the field findings, a major area for future explorations is relating field observations to the results of laboratory experiments. More specifically, it is important to determine if As oxidation/reduction reactions in specific natural settings are dominated by homogeneous or heterogeneous pathways, and to continue studying the factors controlling these reactions. Additional important directions of study include the degree of As and Sb association with colloids, the chemical identity of these colloids, and the speciation of As and Sb associated with them.

A mechanistic understanding of the redox transformations and partitioning of As and Sb on the mineral substrates is of foremost importance in modeling and predicting the environmental fate of these toxic elements. Future work has to be focused on the molecular level processes in order to determine the exact stoichiometry and reactive species, which can be represented as simplified structural units, characteristic to a number of mineral substrates. The laboratory results have to be coupled to the field observations in order to establish simplified and accurate models.

## References

Bose, P., Sharma, A., 2002. Role of iron in controlling speciation and mobilization of arsenic in subsurface environment. Water Research, 36(19): 4916-4926.

Charlet, L., Bosbach, D., Peretyashko, T., 2002. Natural attenuation of TCE, As, Hg linked to the heterogeneous oxidation of Fe (II): an AFM study. Chemical Geology, 190(1-4): 303-319.

Charlet, L. et al., 2005. Adsorption and heterogeneous reduction of arsenic at the phyllosilicate-water interface. In: O'Day, P., Vlassopoulos, D., Meng, X., Benning, L. (Eds.), Advances in Arsenic Research: Integration of Experimental and Observational Studies and Implications for Mitigation.

Kelly, S., Hesterberg, D., Ravel, B., 2008. Analysis of Soils and Minerals Using X-ray Absorption Spectroscopy. In: Ulery, A., Drees, L. (Eds.), Methods of Soil Analysis: Part 5--Mineralogical Methods.

Manceau, A. et al., 2000. Oxidation-reduction mechanism of iron in dioctahedral smectites: II. Crystal chemistry of reduced Garfield nontronite. American Mineralogist, 85(1): 153.

Stollenwerk, K., 2003. Geochemical processes controlling transport of arsenic in groundwater: A review of adsorption. Arsenic in ground water: Geochemistry and occurrence: 67-100.

Stucki, J., 2006. Properties and behaviour of iron in clay minerals. Handbook of Clay Science: 423–475.

Stucki, J.W., Lee, K., Zhang, L., Larson, R.A., 2002. Effects of iron oxidation state on the surface and structural properties of smectites. Pure and Applied Chemistry, 74(11): 2145-2158.

Webster-Brown, J.G., Lane, V., 2005. The Environmental Fate of Geothermal Arsenic in a Major River System, New Zealand World Geothermal Congress, Antalya, Turkey.

Wilson, S., Lockwood, P., Ashley, P., Tighe, M., 2010. The chemistry and behaviour of antimony in the soil environment with comparisons to arsenic: A critical review. Environmental Pollution(158): 1169-1181.

# Appendix: Methods

## A.1 Arsenic Analysis in Water with High $Cl^-$ Content by Inductively Coupled Plasma Mass Spectrometry (ICP-MS)

High total dissolved solids concentration can cause several effects on ICP MS measurements, including signal suppression and spectral interferences caused by polyatomic species. For arsenic these species are $ArCl^+$ and CaCl with the mass of 75.

There are several approaches to overcome the interferences. One of them is to use sample pretreatment, which can include using a chromatographic column to remove $Cl^-$, precipitating AgCl, or addition of organic solvent (ethanol, methanol or propanol). Another approach is to modify plasma by addition of diatomic gas to the plasma gas (most commonly 5% $N_2$ to Ar plasma). The mathematical approach based on isotopic occurrences, includes an equation: $As(75)=1\times(^{75}C)-3.127\times(^{77}C)+2.549\times(^{82}C)$. And the most recent approach is to use a collision/reaction cell (CRC), when a reaction cell is being pressurized with $H_2$ or He. The larger polyatomic species are not able to make it through. In the case of using a reaction cell there is no need in applying an interference correction equation.

CRC is most effective if run in robust plasma conditions: sensitivity ~50 million cps/ppm at mid-mass with background < 5 cps, $CeO^+/Ce^+<1$ %, $Ce^{++}/Ce^+<1.5$ %.

Table A.1 Tuning for robust plasma conditions

| Parameter | Optimum | How to adjust |
|---|---|---|
| $CeO^+/Ce^+$ | <1 % in normal mode | Decrease gas flow rate and/or peri-pump<br>Increase sampling depth (8 mm is optimum, however if need to have very robust plasma can be increased to 10 mm) |
| Maximum matrix tolerance | | This is accomplished by decreasing the voltage on **Extract 1**. First find the voltage that gives maximum sensitivity between 1-5 V. Then reduce the voltage by 1-3 V. The resulting voltage should be much closer to zero and only slightly positive or negative.<br>Set **Extract 2** to find maximum sensitivity in the range between -170 and -130 V.<br>Set **Omega Bias** for best sensitivity between -30 and -14V.<br>Set **Omega lens** for best sensitivity between -2 and +3V. Work back and forth to find the best combination.<br>Set the **Cell entrance and exit** at -30 V (Normal mode).<br>Set **QP focus** for best sensitivity between 1 and 5 V. |

Tuning procedure

**I. Normal mode**

Monitor

- $CeO^+/Ce^+$ and $Ce^{++}/Ce^+$
- mass 27 (there is an interference in normal mode at this mass)

a). Adjust **QP bias** to decrease mass 27

For best sensitivity:

b). Adjust **Extract 1** and **Omega lens**, then **Cell entrance, Cell exit, Octopole bias.**

| Cell entrance voltage should be lower than Octopole Bias! |
|---|

c). Adjust **QP focus** for maximum sensitivity at m/z 7 and 59, minimum at m/z 27

| Octopole bias should always be at least 3 V lower than QP bias! |
|---|

**II. Helium mode**

Use normal mode parameters for gas modes, only adjust **Cell exit, QP focus, Oct. bias** and **QP bias.**

Use tuning solution with 1 % HCl.

a). Monitor

- mass 51, 59 and 75 (ClO, Co, ArCl)
- ratio 51/59

Need to achieve 51/59 <1 % (ideally 0.2 %)

b). Set He flow for 4 ml/min

c). Adjust **Octopole bias, Cell exit, QP focus** and **QP bias** to more negative values to compensate for loss of ion kinetic energy in the collision cell.

d). Adjust slowly He flow to achieve 51/59 ratio of less than 1%. It may be necessary to adjust the difference between the **Octopole bias** and **QP bias** to somewhat more than 3 V.

**III. Hydrogen mode**

a). Monitor mass 56, 59 and 80

b). Set $H_2$ flow initially to 4 ml/min

c). Slowly decrease the hydrogen flow until the signal at 80 begins to climb, indicating the presence of ArAr, then increase the flow by 0.1-0.2 ml/min.

Table A.2 Typical values for robust plasma conditions

| **Parameter** | **Normal mode** | **$H_2$** | **He** |
|---|---|---|---|
| Extraction 1 | 0 V | same | same |
| Extraction 2 | -130 V | same | same |
| QP focus | 3 V | -8 V | -10 V |
| Cell exit | -22 V | -45 V | same |
| Octopole bias | -6 V | -18 V | same |
| QP bias | -3 V | -15 V | same |

## A.2 Cation Program for Ion Chromatography

```
Pressure.LowerLimit =                          200 [psi]
          Pressure.UpperLimit =                3000 [psi]
          %A.Equate =                          "%A"
          CR_TC =                              On
          LoadPosition
          Data_Collection_Rate =               5.0 [Hz]
          CellTemperature.Nominal =            30.0 [°C]
          ColumnTemperature.Nominal =          30.0 [°C]
          Suppressor_Type =                    CSRS_4mm
          ; Pump_ECD.H2SO4 =                   0.0
          ; Pump_ECD.MSA =                     20.0
          ; Pump_ECD.Other eluent =            0.0
          ; Pump_ECD.Recommended Current =     66
          Suppressor_Current =                 66 [mA]

-3.500    Pump_ECD_Relay_1.Closed              Duration=138.00
          Concentration =                      20.00 [mM]
          Flow =                               1.00 [ml/min]

 0.000    Concentration =                      10.00 [mM]
          Flow =                               1.00 [ml/min]
          ECD_1.AcqOn
          Pump_InjectValve.InjectPosition      Duration=30.00
          Concentration =                      10.00 [mM]
          Flow =                               1.00 [ml/min]

 2.500    Concentration =                      3.00 [mM]

 25.000   Concentration =                      3.00 [mM]

 26.500   Concentration =                      15.00 [mM]
          Flow =                               1.50 [ml/min]

 50.000   ECD_1.AcqOff
          Concentration =                      15.00 [mM]
          Flow =                               1.50 [ml/min]


          End
```

## A.3 Anion Program for Ion Chromatography

```
CR_TC =     On
            Pressure.UpperLimit =                 3000 [psi]
            %A.Equate =                           "%A"
            Data_Collection_Rate =                5.0 [Hz]
            CellTemperature =                     30.0 [°C]
            ColumnTemperature =                   30.0 [°C]
            Suppressor_Type =                     ASRS_4mm
            ; Pump_ECD.Carbonate =                0.0
            ; Pump_ECD.Bicarbonate =              0.0
            ; Pump_ECD.Hydroxide =                20.0
            ; Pump_ECD.Tetraborate =              0.0
            ; Pump_ECD.Other eluent =             0.0
            ; Pump_ECD.Recommended Current =      50
            Suppressor_Current =                  80 [mA]
            Flow =                                1.00 [ml/min]

-2.500      Pump_ECD_Relay_1.Closed               Duration=0.10
            Pressure.LowerLimit =                 200
            Pressure.UpperLimit =                 3000
            %A.Equate =                           "%A"
            LoadPosition
            Concentration =                       0.50 [mM]
            Curve =                               5

 0.000      Autozero
            Pump_InjectValve.InjectPosition       Duration=200.00
            ECD_1.AcqOn

 2.000      Pump_ECD_Relay_1.Open
            Pump_ECD_Relay_1.State                Open

 3.000      Concentration =                       0.50 [mM]
            Curve =                               5

12.000      Concentration =                       12.00 [mM]
            Curve =                               5

35.000      Concentration =                       50.00 [mM]
            Curve =                               5

36.000      Concentration =                       0.50 [mM]
            Curve =                               5

36.000      ECD_1.AcqOff
            End
```

**A.4. Alkalinity Titration**

Modified from A. D. Eaton, L. S. Clesceri, E. W. Rice, A. E. Greenberg and M. A. H. Franson. Standard Methods for Examination of Water and Wastewater, 21st edition, Amer Public Health Assn, 2005, p. 2-27 – 2-29

Apparatus

1. pH meter with a combination electrode
2. Burette 25 ml
3. Microburette 5 or 10 ml
4. Stirring plate, stir bars
5. Beaker 150-200 ml

Reagents

0.0200 N $H_2SO_4$ – dilute commercially available stock solution

DI $H_2O$

$Na_2CO_3$ 0.05 N - Dry $Na_2CO_3$ at 250 °C for 4 hours, cool in desiccator. Weigh 1.325 g of $Na_2CO_3$ and dilute to 500 ml with DI $H_2O$ and stir. Do not keep for more than 1 week.

Buffer solutions for pH meter calibration.

Procedure

Prepare check standards of $Na_2CO_3$ by diluting stock solution.

| ml stock diluted to 1 l | mg alk/l as $CaCO_3$ |
|---|---|
| 4.0 | 10 |
| 19.98 | 50 |

Calibrate the pH meter

All solutions and samples should be at room temperature

Titrate 100 ml of sample or check standard with 0.0200N $H_2SO_4$ using regular burette and 5 ml microburette (for fine adjustments). The stirring action should be vigorous enough

near the end of titration to break the surface to allow rapid equilibrium of $CO_2$ between the solution and atmosphere. Stop the titration at exact pH of 4.5 and record volume.

Calculation

$$Alk_{total}, mgCaCO_3 / l = ml(titrant) \times 10$$

if the normality of $H_2SO_4$ solution is different than 0.02 N:

$$Alk_{total}, mgCaCO_3 / l = \frac{A \times N \times 50{,}000}{ml(sample)}$$

A – ml standard acid used

N – normality of standard acid

For alkalinities less than 20 mg/l: titrate with 0.0200 N $H_2SO_4$ and stop the titration in the range of pH 4.3 to 4.7, record the volume acid used and exact pH. Carefully add more titrant using microburette to reduce the pH exactly 0.30 pH unit and again record the volume.

Calculation:

$$Alk_{total}, mgCaCO_3 / l = \frac{(2B - C) \times N \times 50{,}000}{ml(sample)}$$

B – ml titrant used to the first recorded pH

C – total ml titrant to reach pH 0.3 unit lower

N – normality of $H_2SO_4$ acid.

**A.5 Method for Clay Separation from Dried Bottom Sediments**

Supporting material: LSIS Technical Memorandum #92-1, Version 3, January 1992, University of Western Ontario, by Jennifer McKay

Equipment and glassware:

~150 ml nalgene bottle

50 ml beaker

500 ml mixing cylinder, marked with tape at 30 cm

Grinding tool

Scale

Vortetex

Peristaltic pump

Sample:

~10 g of sample

Procedure:

1. If the sample is agglomerated, gently disintegrate it using pestle and mortar. DO NOT grind it.
2. Weight the sample and record the weight.
3. Put the sample in 150 ml bottle, add ~50 ml of DI water and stir using vortex for a minute.
4. Pour off the slurry into a 500 ml mixing cylinder.
5. Repeat steps 2 and 3 until water is clear after stirring.
6. The mixing cylinder should be filled to 30 cm height (marked with tape). Add some water if it's not quite full, do not overfill!
7. Tap the cylinder and mix the slurry in it very well, dumping it upside down several times.

8. Let the cylinder sit undisturbed for 23 hours and 16 min (at 20 °C room temperature) so that fraction >2 micron settles down (time is calculated using Stokes Law*). Record the time and calculate when settling should be ended.
9. Dry the sample left over in the nalgene bottle after discarding the slurry (large fraction).
10. Discard the supernatant from the mixing cylinder into a 1,000 ml nalgene bottle, using peristaltic pump.
11. Put the sediments left in the mixing cylinder into 50 ml beaker, dry in an oven (do not exceed 60 ° C), mix it with the rest of the large fraction sample and keep for further analysis.
12. Pour the slurry from the 1,000 ml bottle in the centrifuge tubes.
13. Weight the tubes to equal weight of 50 g +/- 0.1 g.
14. Use centrifuge to separate clay fraction, use setting for 11,000-12,000 rpm for 10-20 min. Water should look clear after the centrifuging, and in case if it does not, rotate for additional 10 min.
15. Discard water from the tubes, leaving 1-2 ml. Put the clays back into water by using vortex (preferred) or glass stirring bar.
16. Collect all the suspended clay in one sample vial (usually they fit into 5 ml vial).
17. XRD slide can be prepared using the suspension.
18. For mass estimate, weigh the left over large fraction sample. The difference in mass between initial sample and large fraction is the mass of clay content.

* Stokes Law: $v = [g(sp\text{-}sl)D^2]+18n$

or $t = (18nh) + [g(sp\text{-}sl)D^2]$

D-particle diameter (2 micron = $2 \times 10^{-4}$ cm)

v – settling velocity (cm/sec) = h x t

h = height or settling depth (30 cm)

t = time in seconds

n = viscosity (poise)

g = gravitational constant (980 $cm/s^2$)

sp = specific gravity of the particle (2.65)

sl = specific gravity of the liquid (sl for water at 20 $^oC$ = 0.99823)

**A.6 Method for Partial Digestion of Bottom Sediment**

Retrieved from: K. Loska and D. Wiechula Comparison of Sample Digestion Procedures for the Determination of Arsenic in Bottom Sediment Using Hydride Generation AAS, Microchim Acta 154, 235-240 (2006).

Detection level: theoretically the same with ICP MS, however needs to be evaluated for every type of sample.

Apparatus

Microwave oven, vessels

Reagents

Ultrapure concentrated $NHO_3$

Utrapure concentrated HCl

Procedure

Weight 150 mg samples of bottom sediment, dried to remove hygroscopic humidity, into Teflon vessels washed with $HNO_3$ and rinsed with distilled water. Use the following combination of concentrated acids (aqua regia): 1.5 ml $HNO_3$ + 4.5 ml HCl

Load the samples in the rotor body and seal.

Place the rotor in the microwave and use the program outlined below.

Program:

| Step | Power | min | Fan |
|---|---|---|---|
| 1 | 250 W | 3 | 1 (continuous cooling/exhaust at low intensity) |
| 2 | 450 W | 2 | 1 |
| 3 | 650 W | 4 | 1 |
| 4 | 950 W | 3 | 1 |

After digestion is complete, cool and dismantle the rotor. Let the acids evaporate by leaving open samples in a fume hood. After the acids are evaporated to dryness, take the

samples out of the rotor body, add 10 $cm^3$ of water and transfer the samples to 50 $cm^3$ volumetric flasks and fill to volume.

In order to evaluate the method, perform digestion of the reference material GXR-1 and GXR -3 (427 and 3970 ppm As respectively).

**A.7 Ion-selective Electrode Method for Sulfide Analysis**

Retrieved from Standard methods for the examination of water and wastewater, 21 ed., 2005; edited by Eaton A.D., Clesceri L.S., Rise E.W. and Greenberg A.E.
Orion Silver/Sulfide electrode Instruction manual

Detection level: 0.032 mg/L ($1x10^{-6}$M) – 100 mg/L

Apparatus

1. Silver/sulfide electrode
2. Double junction reference electrode
3. Electrode polishing strips
4. pH-mater with millivolt scale, capable of 0.1-mV resolution
5. Electrochemical cell: Make suitable cell from a 150 ml beaker and a sheet of rigid plastic (PVC or acrylic) with holes drilled to allow insertion of the electrodes and a tube for flushing the headspace with nitrogen
6. Gas dispersion tube: Use to deaerate water for preparing reagents and standards
7. Magnetic stirrer and stirring bar

Reagents

1. Alkaline antioxidant reagent (AAR)

In a 1 L volumetric flask add:

~600 ml deaerated reagent water

80 g NaOH

35 g ascorbic acid

67 g $Na_2H_2EDTA$

Swirl to dissolve and dilute to 1 L with deaerated reagent water (DRW).

The color of resulting solution should be from colorless to yellow. Store in a tightly capped brown glass bottle. Discard when solution becomes brown.

2. Lead perchlorate, 0.1 M

In 1,000 ml DI water dissolve

46.0 g $Pb(ClO_4)_2 \cdot 3H_2O$

Standardize by titrating with $Na_2H_2EDTA$

$2Pb(ClO_4)_2 \cdot 3H_2O + Na_2H_2EDTA \rightarrow Pb_2EDTA + Na_2H_2(ClO_4)_4 + 6H_2O$

[Note: Put a known amount of moles of $Na_2H_2EDTA$ in a flask; titrate with lead perchlorate solution to the end point; # of moles of $Pb(ClO_4)_2 \cdot 3H_2O$ = 2 x # of moles of $Na_2H_2EDTA$; concentration of lead perchlorate = # of moles/volume of the solution used.]

Make 0.1 M $Na_2H_2EDTA$ solution. Dissolve 37.225 g $Na_2H_2EDTA$ in a 1,000 ml volumetric flask with DI water, heat up a little bit. If have difficulties dissolving add a small amount of NaOH. Filter the solution. This solution needs to be normalized by titration with $CaCO_3$.

Make a standard $CaCO_3$ solution. Use dried $CaCO_3$ (dry in an oven at 250 °C for at least 2 hours, cool in a dessicator). Weight 0.250 g in a beaker, add ~25 ml of DI water, and add dilute HCl drop wise, until dissolved. Add another 2 drops. Transfer to 250 ml volumetric flask.

Make a pH 10 buffer solution. Dissolve 16.9 g ammonium chloride ($NH_4Cl$) in 143 ml conc ammonium hydroxide ($NH_4OH$).

Make the indicators. Dissolve 0.05 g Eriochrome Black T in 10 g triethanolamine. Dissolve 0.05 g xylenol orange in 10 ml DI water.

Pipet 50-ml aliquots of the standard $CaCO_3$ solution into three or four 250-ml Erlenmeyer flasks. Add 7-8 ml of pH 10 buffer to the first sample, 15 ml of DI water, and 3 drops of Eriochrome Black T and titrate immediately with

$Na_2H_2EDTA$ solution until the light red solution turns a light sky blue. Repeat for the replicates.

Titrations must be performed quickly because ammonia will evaporate and thus the pH of the solution will change.

Calculate the molarity of the $Na_2H_2EDTA$ from the volume of $Na_2H_2EDTA$ used in the titration of each aliquot.

$CaCO_3 + Na_2H_2EDTA \rightarrow CaEDTA + Na_2CO_3$

$$C_{Na2H2EDTA} = \frac{V_{CaCO3} \times [CaCO_3]}{V_{EDTA}}$$

The results for the replicates should be very close, if not – repeat titration.

Standardize $Pb(ClO_4)_2$ solution by titrating with known concentration $Na_2H_2EDTA$ solution.

$2Pb(ClO_4)_2 \cdot 3H_2O \times XylOr + Na_2H_2EDTA \rightarrow Pb_2EDTA + Na_2H_2(ClO_4)_4 + 6H_2O + XylOr$

Use spectrophotometer to detect the end point of titration. Prepare 10-15 50 ml beakers. Put 2 ml of ~0.1 M $Pb(ClO_4)_2$ in each, add 1 ml of Xylenol orange, and 30 ml of DI water. Titrate with $Na_2H_2EDTA$ solution until color starts to change from red-purple to yellow, to each subsequent sample add 0.1 ml more $Na_2H_2EDTA$.

When it seems that color of each subsequent sample does not change anymore, add 2 ml extra to the last sample (overtitrate).

Prepare 2 end members - one with 2 ml of Pb solution, 30 ml of $H_2O$ and 1 ml of Xyl.Or., another end member - 2 ml $Na_2H_2EDTA$ solution, 1 ml Xylenol orange and 30 ml $H_2O$. Measure the absorbance spectra using spectrophotometer, record the absorbance at 578 nm.

As soon as absorbance is approximately equal to the blank $Na_2H_2EDTA$, it is the end point.

Calculate the $Pb(ClO_4)_2$ solution concentration:

$$C_{Pb(ClO4)2} = \frac{V_{EDTA} \times [EDTA]}{0.002L}$$

3. Sulfide stock solution, 130 mg/L

Use sodium sulfide nonahydrate ($Na_2S \cdot 9H_2O$) crystals

Use degassed water (Ar or $N_2$)

Preferably remove single crystals of $Na_2S \cdot 9H_2O$ from reagent bottle with nonmetallic tweezers; quickly rinse in degassed reagent water. Blot crystal dry with tissue, than rapidly transfer to a tared, stoppered weighing bottle containing 5 – 10 ml degassed reagent water. Repeat procedure until desired amount of sodium sulfide is in weighing bottle. Avoid excess agitation and mixing of the solution with atmospheric oxygen. Add the rest of the DRW. (3.75 g $Na_2S \cdot 9H_2O$ diluted to a final volume of 500 ml will give a stock solution of which 1 ml = 1.00 mg $S^{2-}$). Standardize the solution using iodometric method or ***titration with 0.1M $Pb(ClO_4)_2$.***

***Iodometric method*** *(for standardizing $S^{2-}$ stock solution)*:

1. Standard iodine solution, 0.0250 N: Dissolve 20 to 25 g KI in a little water and add 3.2 g iodine. After iodine has dissolved, dilute to 1,000 ml and standardize against 0.0250 N $Na_2S_2O_3$, using starch solution as indicator.

2. Standard sodium thiosulfate solution, 0.0250 N:
Dissolve 6.205 g of $Na_2S_2O_3 \cdot 5H_2O$ in distilled water. Add 1.5 ml 6N NaOH or 0.4 g solid NaOH and dilute to 1,000 ml. Standardize with bi-iodate ($KH(IO_3)_2$) solution.

3. Starch solution

Dissolve 2 g laboratory-grade soluble starch and 0.2 g salicylic acid, as a preservative, in 100 ml hot distilled water.

4. Hydrochloric acid, HCl, 6N

Measure from a buret into a 500 ml flask an amount of iodine solution estimated to be in excess over the amount of sulfide present. Add distilled water, if necessary, to bring volume to about 20 ml. Add 2 ml 6 N HCl. Pipet 200 ml sample into flask, discharging sample under solution surface. If iodine color disappears, add more iodine until color remains. Back-titrate with $Na_2S_2O_3$ solution, adding a few drops of starch solution as end point is approached, and continuing until blue color disappears.

Calculation:

One milliliter 0.0250 N iodine solution reacts with 0.4 mg $S^{2-}$:

$$mgS2-/l = \frac{[(A \times B) - (C \times D)] \times 16000}{ml(sample)}$$

A = ml iodine solution

B=normality of iodine solution

C=ml $Na_2S_2O_3$

D=normality of $Na_2S_2O_3$ solution

***0.1M $Pb(ClO_4)_2$ titration*** *(for standardizing the $S^{2-}$ stock solution)*

Pipet 50 ml sulfide stock solution into the electrochemical cell. Insert Ag/S electrode and reference electrode and read initial potential. Titrate with 0.1 M $Pb(ClO_4)_2$. Let electrode potential stabilize and record potential after each addition. Locate equivalence point: 1. as the end point is approached, add smaller and equal increments (0.1 or 0.2 ml) at longer intervals, so that the exact end point can be determined; 2. plot a differential titration curve if the exact end point cannot be determined by inspecting the data. Plot change in instrument reading

for equal increments of $Pb(ClO_4)_2$ against volume of $Pb(ClO_4)_2$ added, using average of burette readings before and after each addition:

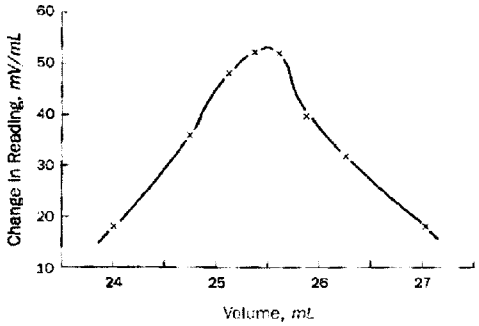


Figure A.1 Change in potential reading during titration with $Pb(ClO_4)_2$

Calculate the function $F_1$ for points before the equivalence point

$$F_1 = (V_0 + V) \times 10^{E/m}$$

$V_o$ = volume of stock solution, ml

V = titrant volume, ml

E = potential, mV

M = slope of calibration curve, mV/log unit.

Plot $F_1$ as a function of titrant volume. Extrapolate to find the intersection with the x-axis; that is, the equivalence point. Calculate sulfide concentration in the stock solution from:

$$C = \frac{V_{eq}[Pb]}{V_0}$$

C = sulfide concentration, mg/l

Veq = equivalence volume

[Pb] = concentration of Pb in titrant, mg/l

Vo = volume of stock solution, ml

Store stock solution in a tightly capped bottle for 1 week or less.

***Store in a fume hood!***

Prepare sulfide standards daily by serial dilution of stock. Add AAR and 1M $Zn(C_2H_3O_2)_2$ solutions to 100 ml volumetric flasks. Add sulfide solutions and dilute to volume with DRW (or DASW). Refer to table A.3 for volumes.

Table A.3 Sulfide standard solutions

| *Dilution* | *Alkaline Atnioxidant Reagent ml* | *Sulfide solution* | *Sulfide solution ml* | *1M Zink Acetate ml* |
|---|---|---|---|---|
| 1:10 | 45 | Stock | 10 | 0.15 |
| 1:100 | 50 | Stock | 1 | 0.15 |
| 1:1 000 | 45 | 1:100 | 10 | 0.14 |
| 1:10 000 | 50 | 1:100 | 1 | 0.15 |

Prepare at least one standard with a concentration less than the lowest sample concentration.

Procedure

Check electrode performance and calibrate daily. Check electrode potential in a sulfide standard every 2 hours. The procedure depends on the sulfide concentration and the time between sample collection and sulfide determination. If the total sulfide concentration is greater than 0.03 mg/L and the time delay is only a few minutes, sulfide can be determined directly. Otherwise, precipitate ZnS, let it settle. Then decant as much supernatant as possible without loss of precipitate. Refill bottle with distilled water, shake to resuspend the precipitate and quickly withdraw a sample. If interfering substances (thiosulfate, sulfite and organic compounds) are present in high concentration, settle, decant, and refill a second time.

a. Check electrode performance: Pipet 50 ml AAR, 50 ml DWR, and 1 ml sulfide stock solution into the measurement cell. Place Ag/S and reference electrodes in the solution and read potential. Add 10 ml stock solution and read potential. The change in potential should be -28±2 mV. If it is not, follow the troubleshooting procedure in the electrode manual.

b. Calibration: Place electrodes in the most dilute standard but use calibration standards that bracket the sulfide concentrations in the samples. Record potential when the rate of change is less than 0.3 mV/min. (This may take up to 30 min for very low sulfide concentrations, i.e., less than 0.03 mg/L.) Rinse electrodes, blot dry with a tissue, and read potential of the next highest standard. For a meter that can be calibrated directly in concentration, follow manufacturer's directions. For other meters, plot potential as a function of the logarithm (base 10) of the sulfide concentration. For potentials in the linear range, calculate the slope and intercept of the linear portion of the calibration plot.

c. Sulfide determination by comparison with calibration curve, with ZnS precipitation: Place filter with ZnS precipitate in a 150 ml beaker containing a stir bar. Wash sample bottle with 50 ml AAR and 20 ml DRW and pour the washings into the beaker. Stir to dissolve precipitate. Remove filter with forcepts while rinsing it into the beaker with a minimum amount of DRW. Quantitatively transfer to a 100 ml volumetric flask and dilute to mark with DRW. Pour into the electrochemical cell and place the electrodes in the solution. Measure potential: record potential when the rate of change is less than 0.3 mV/min. Read sulfide concentration from the calibration curve. Alternatively, for potentials in the linear range, calculate the sulfide concentration from:

$$S_{tot} = 10^{\frac{E-b}{m}}$$

E = electrode potential

B and m are the intercept and slope of the calibration curve. For a meter that can be calibrated directly in concentration, follow the manufacturer's directions.

d. Sulfide determination by standard addition with or without ZnS precipitate: Measure the Ag/S-ISE electrode potential as in c. Add sulfide stock solution and measure potential again. Calculate sulfide concentration as follows:

$$C_o = \frac{fC_s}{(1+f)10^{\frac{Es-Eo}{m}} - 1}$$

Co and Cs = sulfide concentrations in sample and known addition
Eo and Es = potentials measured for sample and known addition
m = slope of calibration curve (approximately 28 mV/log$S^{2-}$)
f = ratio of known addition volume to sample volume

Sulfide determination by titration, with ZnS precipitation: Filter the sample. Place filter with ZnS precipitate in a 150 ml beaker containing a stir bar[1]. Wash sample bottle with 50 ml AAR and 20 ml DRW and pour the washings into the beaker. Stir to dissolve precipitate. Remove filter with forcepts while rinsing it into the beaker with a minimum amount of DRW. Quantitatively transfer to a 100 ml volumetric flask and dilute to mark with DRW. Pour into the electrochemical cell and place the electrodes in the solution. Titrate with lead perchlorate solution. The concentration of the lead perchlorate solution should be ~10-20 times as concentrated as sulfide concentration in the sample. Use standardized 0.1 M lead perchlorate solution to make up the needed concentration. Use the same

[1] This didn't work for me because the sample simply clogged a 0.45 μm filter. In order to get the precipitate, I accurately removed some water from the sample bottle trying not to disturb the precipitate.

procedure as for standardizing the sulfide stock solution. The minimum sulfide concentration for determination by titration is 0.3 mg/L ($10^{-5}$ M).

Table A.4 Reagents for sulfide ion-selective analysis

| **Chemical** | **Amount, concentration** |
|---|---|
| NaOH | 80 g |
| ascorbic acid | 35 g |
| $Na_2H_2EDTA$ | 67 g |
| $Na_2S•9H_2O$ crystals | 3.75 g |
| $Pb(ClO_4)_2•3H_2O$ | 4.60 g |
| $Zn(C_2H_3O_2)_2·2H_2O$ | ~110 g 1 M solution |
| Ar or $N_2$ gas | |
| KI | 20 to 25 g |
| $I_2$ | 3.2 g |
| $Na_2S_2O_3·5H_2O$ | 6.205 g (0.0250 N) |
| Starch, laboratory-grade | 2 g |
| $KH(IO_3)_2$ | |
| Salicylic acid | 0.2 g |
| CaCO3 | ~ 1g |
| NH4Cl | ~20 g |
| NH4OH, conc. | ~ 150 ml |
| Eriochrome Black T | 0.05 g |
| Triethanolamine | 10 g |
| Xylenol orange | 0.05 g |
| HCl | 6 N |